Novel continuous-wave infrared parametric sources and noise analysis of infrared upconversion detectors

Anuja Arun Padhye

Universitat Politécnica de Catalunya

Barcelona, February 2020

Doctorate Program: **Photonics**

Duration: **2016-2020**

Thesis advisor: **Prof. Majid Ebrahim-Zadeh**

Thesis submitted in partial fulfillment of the requirements for the degree of Doctor of Philosophy of the Universitat Politécnica de Catalunya

February 2020

To my family and friends

The best way to predict the future is to invent it.

-Alan Kay

Declaration

I hereby declare that matter embodied in thesis entitled, **"Novel continuous-wave infrared parametric sources and noise analysis of infrared upconversion detectors"** is the result of investigations carried out by me at ICFO- The Institute of Photonic Sciences, Castelldefels, Spain under the supervision of Prof. Majid Ebrahim-Zadeh, and that it has not been submitted elsewhere for the award of any degree or diploma. In keeping with the general practice in reporting scientific observations, due acknowledgment has been made whenever the work described is based on the findings of other investigators.

_____

Anuja Arun Padhye

Certificate

I hereby certify that matter embodied in this thesis entitled, **"Novel continuous-wave infrared parametric sources and noise analysis of infrared upconversion detectors"** has been carried out by Miss. Anuja Arun Padhye at ICFO- The Institute of Photonic Sciences, Castelldefels, Spain, under my supervision, and that it has not been submitted elsewhere for the award of any degree or diploma.

Prof. Majid Ebrahim-Zadeh
(Thesis advisor, ICFO)

Acknowledgements

Life of a PhD student is an emotional roller coaster. I owe so many thanks to all my family members, friends, supervisors, and colleagues for pulling me through these years, and making my ride euphoric. I enjoyed an enriching experience of professional and personal growth in an international environment at ICFO. Firstly I would like to thank my thesis advisor, Prof. Majid Ebrahim-Zadeh for giving me an opportunity to take up the PhD training under his supervision. I am profoundly grateful to him for his invaluable research advice and for patiently supporting me along the way. Thank you Majid for creating constructive atmosphere in the group which allows everyone to succeed in their work.

I am thankful to European Union's Horizon 2020 ITN doctoral programme for generously providing the funding for this research. I would like to thank all professors associated with *Mid-TECH* consortium, for their novel research ideas and guidance. My special thanks goes to Prof. Christian Pedersen for letting me work in his lab and to Dr. Peter Tidemand-Lichtenberg for always being available for discussions during my secondment and even later at ICFO. I am also thankful to committee members of my thesis defense (Prof. Giuseppe Leo, Prof. Luis Roso and Dr. Pablo Loza) for their vital suggestions in shaping up this thesis.

Every PhD student needs an encouraging mentor, I had been lucky to have two; Kavita, who introduced me to many aspects of research in the initial stage and Chaitanya, who advised me during the second half of my PhD. I would like to thank both for sharing their knowledge and experience. Cheers to my other lab mates: thanks

Shahrzad for sharing delightful moments during conferences, thank you Pep for lending a helping hand whenever in need and special thanks for translating the abstract of this thesis to Spanish, thank you Jun and Biplob for sharing a nice time while working in the lab, special thanks to Sukeert and Tess for making our office a happening place, many more thanks to Hanyu and Callum for always being there as best buddies at and outside of work.

I would like to thank the whole team of students (Michael, Pascaline, Rasmus, Laurent, Ashik, Yu-Pei, Saher, Sylvain, Yohei, Ján) involved in *Mid-TECH* project for helping each other throughout our PhD studies and for spending wonderful time post-meetings. Many thanks to Mahmoud and Lichun for the great collaborative work. Especially to Lichun for introducing me to the interesting concept of upconversion noise and for successfully getting our work published. Thanks a lot Dr. Peter-John Rodrigo for guiding us through this project. I am thankful to Ajanta for always encouraging me to work on upconversion detection.

I would like to convey my heartfelt thanks to Anne, Laia, Mery, Ingrid, Manuela and other HR staff for taking care of the administrative part related to my work and stay in Spain. I am indebted to mechanical and electronic workshop teams, IT department, travel and purchasing unit, KTT, ICFO frontdesk and maintenance, ICFO communication and events teams for their prompt everyday assistance through all these years. Special thanks to Ferran for making many books available and checking my resumen. Thank you ICFO Outreach team for giving me an opportunity to volunteer science outreach programs by serving the community.

Thanks to the group of Indian friends at ICFO, Samyobrata, Hitesh, Chetan, Manabendra, Mohit, Aamir, Anamika, Avijit, Swapan, Debraj for organizing events and feeding delicious homemade

food during the festivities. Thank you Chris, Prem, Adara and Manisha for making life in Barcelona fun. Thanks to Vrinda, Zoraze and Siddharth for sharing nice time in Castelldefels. Thank you Shuchi and Niels for the delish sweets and for taking me around Barcelona as a newbie. Cheers to Laurent, Rafael, Alican, Alba, Chariklea, Markos for the memorable and fun outings. Thanks Shreyasi, Pablo and Monserrat for making fond memories in the flat.

Many thanks to Kavitha (a.k.a. KKG), Pamina, Susmita for introducing me to the lunch group and for being close friends from thereon. Thank you Sandra for planning amazing activities around Castelldefels and a memorable trip to Turkey. Thanks Ugaitz, Julio, Iker, Irene and Alvaro for organizing cool parties. A big thanks to Ipsita, Varun, Pandian, Charitra, Sumana, Stephy, Sandhya and Rajashree for making life in Castelldefels even more beautiful. I can't thank Nitin enough for supporting me as a big brother-*cum*-mentor. Thanks a lot Vikas for making me a strong person. Many thanks to Rinu for taking care of me like his younger sister and for creating cherishable moments. Thank you very much Vindhiya for always lending a ear and being my amazing troubleshooter.

Many thanks to my neighbour Mrs. Esther Blanc for treating me like her daughter and for everything else. I would also like to thank several other warm families from our building who always tried to convince me to stay there forever. All these lovely people from Castelldefels including many shop vendor friends have made me feel this town like a home away from home.

Thank you very much to all my school and college teachers, university professors and other international researches with whom I had worked before joining the PhD. Without their constant guidance and encouragement I could not have reached this far. Another important part of my life is the big bunch of friends that I made during

different phases of my studies. I can not thank them enough for sending unconditional love and affection from different continents.

I owe a huge debt of gratitude to my extended family- grandparents, aunts, uncles, cousins and their spouses, nieces and nephews for their immense love, enthusiasm and patience. Thanks a ton for being so supportive.

Words are not enough to thank my boyfriend for always motivating me to bring out the best in me. Thank you very much Kapil for being an eternal sunshine of my life, showering boundless love and laughter. I feel blessed to have his lovely parents and sister by my side who welcomed me into their family with open arms.

I am falling short of words to express my gratitude towards my inspiring parents, Kirti and Arun. Their sage counsel, optimistic approach towards life and unconditional support to my decisions mean a lot to me. *Aai* and *baba* you gave me the wings to fly and explore this world on my own. Thank you very much for the infinite love and care you poured me with.

Abstract

The ability to manipulate frequency of light, through parametric frequency conversion sources based on $\chi^{(2)}$ nonlinear materials, offers an effective route to spectral regions unapproachable by conventional lasers. Most importantly, three-wave mixing processes provide tunable coherent radiation over a broad spectral range. Among the most important tunable devices, narrow linewidth continuous-wave (cw) infrared (IR) optical parametric oscillators (OPOs) are indispensable excitation sources for many applications in molecular spectroscopy and precision metrology. In order to exploit such applications, the development of cw OPOs deploying different wavelength tuning schemes and novel nonlinear materials is highly dezirable, as presented in this thesis.

We demonstrated a rapidly tunable cw OPO based on fan-out grating design periodically-poled $KTiOPO_4$ (PPKTP) crystal at room temperature. This approach allows continuous wavelength tuning by avoiding increased thermal fluctuations at higher operating crystal temperatures. The 532 nm-pumped, output-coupled singly-resonant oscillator (OC-SRO) provides widely tunable near-IR radiation across 741-922 nm and 1258-1884 nm, with total output power of 1.65 W. The use of output coupling for the resonating wave reduces thermal loading and enables 30% enhancement in the OPO extraction efficiency over the pure SRO configuration.

Towards the goal of developing a next-generation cw source $>$4 µm using a newfound quasi-phase-matched semiconductor material, orientation-patterned gallium phosphide (OP-GaP), we demonstrated the first realization of a tunable cw mid-IR source based on

OP-GaP by exploiting single-pass difference-frequency-generation (DFG) between a Tm-fiber laser at 2010 nm and a home-built OPO based on MgO-doped periodically-poled $LiNbO_3$ (MgO:PPLN) crystal. The DFG source generates up to 43 mW of output power, with $>$30 mW across 96% of the tuning range 4608-4694 nm, in high beam quality.

As the tunable mid-IR sources are making great strides, the availability of fast and sensitive mid-IR detectors become equally important. However, the conventional mid-IR detectors demand cryogenic systems for low-noise operation which sets a major drawback as these devices are often bulky and expensive. In this context, the nonlinear frequency upconversion technique has emerged as a promising alternative to the direct detection of mid-IR radiation at room temperature. An upconversion detector (UCD) can be further optimized by identifying and suppressing its noise sources. In order to do so, we experimentally and theoretically investigated noise properties of 1064 nm-pumped single-pass UCD designed for signal detection in telecom and mid-IR range using MgO:PPLN crystals. We studied the dependence of newly discovered SHG (532 nm)-induced spontaneous parametric downconversion (SHG-SPDC) noise intensity on the pump power and crystal temperature, and compared it with the well-known UCD noise source upconverted spontaneous parametric downconversion (USPDC). The measurements deduce that SHG-SPDC must be given a careful consideration since it can act as a dominant noise source under certain operating conditions. However, SHG-SPDC can be avoided by choosing a proper combination of MgO:PPLN grating period, operating temperature, and bandpass filter.

Resumen

La capacidad de manipular la frecuencia de la luz, a través de fuentes de conversión de frecuencia paramétrica basadas en materiales no lineales del tipo $\chi^{(2)}$, ofrece un acceso eficaz a las regiones espectrales inaccesible por los láseres convencionales. Además, los procesos de mezcla de tres ondas proporcionan una radiación coherente sintonizable sobre un rango espectral muy amplio. Entre los dispositivos sintonizables más importantes, los osciladores ópticos paramétricos (OPOs) de onda continua (cw) en el infrarrojo (IR) con ancho de banda estrecho, son fuentes esenciales para muchas aplicaciones en espectroscopia molecular y metrología de precisión. Con el fin de explotar tales aplicaciones, es muy deseable el desarrollo de OPOs de cw mediante diferentes esquemas de sintonización de longitud de onda y nuevos materiales no lineales, como se presentan en esta tesis.

Mostramos aquí un OPO de cw rápidamente sintonizable basado en un cristal *periodically-poled* $KTiOPO_4$ (PPKTP) con diseño de red *fan-out* (en abanico) a temperatura ambiente. Este enfoque permite una sintonización continua de la longitud de onda evitando el aumento de las fluctuaciones térmicas a temperaturas de funcionamiento más altas de los cristales. El OPO resonante con acoplador de salida (OC-SRO) bombeado a longitud de onda de 532 nm, proporciona radiación sintonizable en el infrarrojo cercano (*near-IR*) a través de 741-922 nm y 1258-1884 nm, con una potencia de salida máxima de 1.65 W. El uso del acoplador de salida para la onda resonante reduce la carga térmica y permite una mejora del 30% en la eficiencia de extracción del OPO sobre la configuración SRO pura.

Con el objetivo de desarrollar la nueva generación de fuentes de onda continua con longitud de onda >4 µm utilizando la técnica de *quasi-phase-matching* con materiales semiconductores, presentamos la primera demostración de una fuente de onda continua sintonizable en el infrarrojo medio (*mid-IR*) utilizando el patrón de orientación de fosfuro de galio (OP-GaP) y generación de frecuencia diferencia (DFG) entre un láser de fibra Tm a una longitud de onda de 2010 nm y otro OPO hecho en el laboratorio basado en un cristal MgO-doped *periodically-poled* $LiNbO_3$ (MgO:PPLN). La fuente DFG genera hasta 43 mW de potencia de salida, con >30 mW a través de un 96% del rango de sintonización 4608-4694 nm, con una alta calidad de haz.

A medida que las fuentes de emisión en el *mid-IR* sintonizables mejoren sus prestaciones, la disponibilidad de detectores de *mid-IR* rápidos y sensibles se vuelve igualmente importante. Sin embargo, los detectores de *mid-IR* convencionales requieren sistemas criogénicos para operar con poco ruido, lo que presenta un gran inconveniente ya que estos dispositivos suelen ser voluminosos y caros. En este contexto, la técnica no lineal de conversión ascendente de frecuencia ha surgido como una alternativa prometedora a la detección directa de la radiación de *mid-IR* a temperatura ambiente. Un detector de conversión ascendente (UCD) se puede optimizar aún más identificando y suprimiendo sus fuentes de ruido. Para hacerlo, investigamos teórica y experimentalmente las propiedades de ruido de un UCD de un solo paso bombeado a 1064 nm diseñado para la detección de señales en telecomunicaciones y rango *mid-IR*, utilizando cristales MgO:PPLN. Descubrimos una nueva fuente de ruido llamada ruido espontáneo paramétrico de conversión descendente inducido por generación de segundo harmónico SHG (SHG-SPDC). Estudiamos, también, la dependencia de la intensidad de este ruido (SHG-SPDC) con la potencia de bombeo y la temperatura del cristal.

Finalmente, también comparamos su intensidad con el conocido ruido generado por el detector UCD, llamado ruido de conversión ascendente por conversión paramétrica descendente espontánea (US-PDC). Los resultados obtenidos nos dicen que se debe considerar cuidadosamente el SHG-SPDC, ya que puede actuar como una fuente de ruido dominante en ciertas condiciones de operación. Sin embargo, el SHG-SPDC se puede evitar al elegir una combinación adecuada de MgO:PPLN, el período de red, la temperatura de operación y el filtro de tipo pasa banda.

List of publications

Journal publications

1. K. Devi, **A. Padhye**, Sukeert, and M. Ebrahim-Zadeh, "Widely tunable room-
temperature continuous-wave optical parametric oscillator based on periodically-poled $KTiOPO_4$" Opt. Express 27, 24093-24104 (2019).

2. L. Meng, **A. Padhye**, C. Pedersen, M. Ebrahim-Zadeh, and P. J. Rodrigo, "SHG (532 nm)-induced spontaneous parametric downconversion noise in 1064-nm-pumped IR upconversion detectors," Opt. Lett. 44, 1670-1673 (2019).

3. K. Devi, **A. Padhye**, P. G. Schunemann, and M. Ebrahim-Zadeh, "Multimilliwatt, tunable, continuous-wave, mid-infrared generation across 4.6-4.7 μm based on orientation-patterned gallium phosphide," Opt. Lett. 43, 2284-2287 (2018).

Conference proceedings and presentations

1. K. Devi, **A. Padhye**, Sukeert, and M. Ebrahim-Zadeh, "Widely tunable, green-pumped, visible and near-infrared continuous-wave optical parametric oscillator based on fan-out-grating PPKTP," in 8^{th} EPS-QEOD Europhoton Conference (paper WeM. 2.2), Barcelona, Spain, September 2018.

2. K. Devi, **A. Padhye**, P. G. Schunemann, and M. Ebrahim-Zadeh, "Tunable, multi-milliwatt, continuous-wave difference-frequency-generation across 4.6-4.7 μm based on orientation-patterned GaP," in Conference on lasers and Electro-Optics (CLEO), OSA technical digest (paper JTu2A.67), San Jose, USA, May 2018.

3. K. Devi, **A. Padhye**, P. G. Schunemann, M. Ebrahim-Zadeh, "Continuous-wave, multi-milliwatt, tunable difference-frequency generation across 4608-4694 nm in orientation-patterned GaP," Proc. SPIE 10684, 1068410, SPIE Photonics Europe, Strasbourg, France, April 2018.

4. K. Devi, **A. Padhye**, P. G. Schunemann, and M. Ebrahim-Zadeh, "Tunable, continuous-wave, multi-milliwatt mid-infrared source across 4.6-4.7 μm based on orientation-patterned GaP," in High-Brightness Sources and Light-driven Interactions, OSA Technical Digest (paper MW1C.2), Strasbourg, France, March 2018.

Contents

List of Figures

List of Tables

List of Acronyms

AR	Antireflection
BPF	Bandpass filter
BPM	Birefringent-phase-matching
CPM	Critical phase-matching
cw	Continuous wave
DC	Direct current
DCR	Dark count rate
DFG	Difference-frequency-generation
DRO	Doubly-resonant oscillator
EM-CCD	Electron multiplying charge coupled device
fs	Femtosecond
FSR	Free spectral range
FWHM	Full width at half maximum
GRIIRA	Green-induced infrared absorption
GVM	Group velocity mismatch
HHG	High harmonic generation
HVPE	Hydride vapour phase epitaxy
IC-SRO	Intracavity singly-resonant oscillator
IR	Infrared
MBE	Molecular beam epitaxy
MCT	Mercury cadmium telluride
NCPM	Non-critical phase-matching
NEP	Noise equivalent power
ns	Nanosecond
OC-SRO	Output coupled singly-resonant oscillator
OP	Orientation-patterned

OPA	Optical parametric amplifier
OPG	Optical parametric generator
OPO	Optical parametric oscillator
PBS	Polarizing beam-splitter
PE-SRO	Pump-enhanced singly-resonant oscillator
PP	Periodically-polled
ps	Picosecond
QCL	Quantum cascade laser
QPM	Quasi-phase-matching
RDC	Random duty cycle
SFG	Sum-frequency-generation
SHG	Second-harmonic-generation
SHG-SPDC	Second-harmonic-generation induced spontaneous parametric downconversion
SNR	signal-to-noise ratio
SPDC	Spontaneous parametric downconversion
SRO	Singly-resonant oscillator
SVEA	Slowly varying envelope approximation
THz	Terahertz
TRO	Triply-resonant oscillator
UCD	Upconversion detector
USPDC	Upconverted spontaneous parametric downconversion
UV	Ultraviolet

Chapter 1

Introduction

1.1 Background

Laser is one of the most renowned inventions in the history of natural sciences, which has revolutionized the way we live now. The everyday applications of lasers include barcode scanners, blu-ray disc players, laser printers, and fiber optic internet modems. Lasers are also widely used as surgical and imaging tools in medicine, range finders in military, and propulsion systems in engineering. Since the first realization of ruby laser in 1960 [1], numerous laser systems have been developed based on different states of the matter, which are being used as scientific tools in several fields for demonstration of Bose-Einstein condensate by laser cooling [2], gravitational wave detection [3], and laser-based precision spectroscopy [4], to name a few. Recently, the Nobel Prize in Physics 2018 was awarded for groundbreaking inventions in the field of laser physics [5], suggesting future advancements in high-intensity lasers.

Working principle of laser relies on atomic transitions of its gain medium, in which photons stimulate excited atoms to emit radiation at a specific wavelength corresponding to the energy difference of the transition, and the emitted photons are amplified further by the virtue of a resonator cavity [6]. Such photons have identical physical properties, resulting in unidirectional beam with unique coherence and brightness. Lasers can be operated in different modes such as continuous wave (cw) for narrow-linewidth single-frequency operation, Q-switched for energetic nanosecond (ns) pulses, and mode-locked for ultrashort pulses of picosecond (ps) and femtosecond (fs) duration.

Lasers are commonly designated by the type of gain medium employed. Common types include gas, solid-state, dye, and semiconductor lasers. After the initial demonstrations of laser emission at discrete wavelengths, dye lasers were reported to show true wavelength tunability [7]. Later in 1982, Ti:sapphire laser replaced dye lasers for tunable and ultrafast laser applications [8]. Although such tunable lasers allow continuous tuning over a significant wavelength range, in a single device they can typically cover only a limited portion of the electromagnetic spectrum. Hence, many regions extending from ultraviolet (UV) to mid-infrared (mid-IR) are inaccessible to conventional lasers due to the lack of suitable gain media.

Later in 1994, a type of semiconductor laser called quantum cascade laser (QCL) was conceived [9]. The principle of QCL operation is based on intersubband transitions in a stack of multiple quantum well heterostructures. Because the position of the energy levels in such systems is primarily determined by the thickness of semiconductor layers, it is possible to tune the emission wavelength of QCL over a wide range in the same heterostructure material. Several QCLs with broad wavelength tunability spanning over mid-IR and terahertz (THz) spectral range have been reported so far [10]. However, this technology is not suitable for generating wavelengths below 4 µm. Moreover, at high output powers QCLs suffer from deteriorated beam quality [11].

Nonlinear optical frequency conversion sources provide wide wavelength tunability in most of the major parts of the electromagnetic spectrum down to soft X-ray through high harmonic generation (HHG) [12], without deviating from the properties of an ideal laser source. Nonlinear frequency conversion takes place when the response of the medium is a nonlinear function of the applied electromagnetic field. The earliest observations of nonlinear effects were based on the application of DC or low-frequency electric and magnetic fields to optical media [13]. The discovery of nonlinear optical phenomena induced by the high-intensity driving fields was made possible only after the invention of laser.

In 1961, Peter Franken and colleagues used a pulsed ruby laser to produce nonlinear behaviour in a quartz crystal [14]. They showed that frequency of the output beam after the crystal was twice than that of the incident beam. This first-ever demonstration of *second-harmonic-generation* (SHG) is considered as the beginning of nonlinear optics. A year later, Giordmaine reported intense SHG in KH_2PO_4 (KDP) crystal by matching the phase velocities of the fundamental and the generated second-harmonic radiation [15]. In the same journal issue, the first *sum-frequency-generation* (SFG) source based on triglycine sulfate crystal was published [16]. In the same year, theory for *optical parametric generation* (OPG) and *optical parametric oscillator* (OPO) was proposed [17], followed by a comprehensive quantum-mechanical treatment of the nonlinear optical phenomena [18]. In this work Armstrong and colleagues discussed the need of phase-matching for efficient frequency conversion processes, which laid the theoretical foundations of nonlinear optics. Soon after that, the first *difference-frequency-generation* (DFG) between a ruby laser and a mercury lamp was reported [19].

Subsequently in 1965, optical parametric gain accompanied by DFG was demonstrated using $NH_4H_2PO_4$ (ADP) crystals [20], leading to the observation of OPG. It was then followed by an important achievement, when Giordmaine and Miller reported the first experimental demonstration of an OPO [21]. SHG of 1058 nm nanosecond laser was used as a pump source for the OPO based on $LiNbO_3$ crystal, to generate tunable radiation across 970-1150 nm. A couple of years later, cw OPOs were independently demonstrated by Smith et al. [22] and Byer et al. [23].

The realization of OPO was a far-reaching event, because OPOs are the most efficient and versatile among other nonlinear frequency conversion sources. An OPO consists of a nonlinear gain medium placed inside an optical resonator and pumped by a single laser source. Inside the nonlinear medium, pump photon splits into two photons of longer wavelengths (called *signal* and *idler*) under the condition of energy conservation. A

simple illustration of OPO's tunable operation is shown in Figure 1.1, it depicts that the pump wavelength shown in blue can be converted into signal (green line) and idler (red line) through parametric *downconversion* process under a given phase-matching condition. These output wavelengths can be tuned only within the range (determined by the dispersion properties of the nonlinear medium) of the corresponding rectangles by changing the phase-matching condition. The dashed black line represents degeneracy of the pump wavelength.

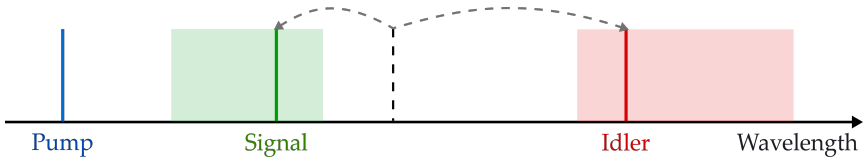

Figure 1.1: Illustration of the working principle of an OPO.

The rapid progress seen so far in the nonlinear optical frequency conversion sources later became torpid, especially the development of practical OPOs was inhibited due to the scarcity of the suitable pump lasers and nonlinear optical materials. Only in the mid-1980s a renaissance began in the pulsed OPO research with the availability of high-power solid-state lasers and the advent of new nonlinear optical materials such as $AgGaS_2$ [24] and β-BaB_2O_4 (β-BBO) [25]. It was then followed by the first demonstration of a synchronously-pumped femtosecond OPO [26].

However, since the early days, development of cw OPOs had been most challenging due to substantially low nonlinear gain available under cw pumping. A watt-level pump laser and an optical crystal with high nonlinearity are the critical requirements for successful operation of a cw OPO. Moreover, for the generation of high-power single-frequency radiation a *singly-resonant oscillator* (SRO) configuration, where a single wave (either signal or idler) resonates inside the OPO cavity, is desirable, despite having high cw threshold power. The first cw SRO was demonstrated in 1993 using birefringent $KTiOPO_4$ (KTP) crystal [27]. Further, to overcome the

high cw SRO threshold, various techniques based on different resonator cavity configurations had been deployed, which include *doubly-resonant oscillator* (DRO) [28], *triply-resonant oscillator* (TRO) [29], *pump-enhanced SRO* (PE-SRO) [30], and *intracavity SRO* (IC-SRO) [31].

By mid 90's, pulsed OPOs were already recognized as an ideal excitation source for gas sensing [32]. However, back then it was not possible to exploit the advantageous properties of single-frequency cw OPOs for high-resolution spectroscopy due to their inefficient performance. A quantum leap in conversion efficiency of cw OPOs was observed after the implementation of *quasi-phase-matching* (QPM) technique obtained by virtue of domain inversion engineering in ferroelectric nonlinear crystals [33]. The first cw OPO based on periodically-poled $LiNbO_3$ (PPLN) was demonstrated in 1996 [34]. Soon after, a cw SRO based on *fan-out* grating PPLN was demonstrated to achieve continuous wavelength tuning at fixed crystal temperature [35]. Around the same period, other periodically-poled crystals such as $KTiOPO_4$ (PPKTP), MgO-doped PPLN (MgO:PPLN), and stoichiometric $LiTaO_3$ (MgO:sPPLT) emerged, which culminated in highly efficient cw infrared OPOs and other nonlinear frequency conversion devices. The most sophisticated cw OPOs to date rely on these ferroelectric materials.

The first commercial single-frequency cw OPO was introduced as early as in 2000 [36]. Later by using the high-power stable fiber laser pump with superior spatial properties, a true cw SRO was made available in the market [37], and ever since the power-scaling of cw OPOs is continuing equipped with the contemporary technology [38].

So far several cw OPO systems have been successfully demonstrated for attaining different performance goals [39]. Frequency selective optical elements, such as intracavity etalon [40] and diffraction grating [41] have been employed to suppress mode hops in cw SROs. In the past our group reported cw SROs based on MgO:sPPLT using Yb-fiber laser under green pumping scheme for near-IR generation [42] and direct pumping for high-power mid-IR generation [43]. We also demonstrated wavelength extension

of MgO:sPPLT cw SROs into the visible [44] and UV [45] using additional frequency doubling and *upconversion* schemes within the OPO cavity. A single-frequency cw SRO with highest total output power of 17.5 W was reported, in which resonating beam was coupled out to reduce the thermal load in MgO:PPLN crystal by reducing the intracavity signal power [46]. By exploiting techniques such as dual-crystal OPO [47] and interferometric output coupling scheme [48], the versatility of fiber-laser-pumped SROs was demonstrated with further improvements in extraction efficiency and wavelength flexibility. The rapid and wide wavelength tuning in the near-IR was demonstrated by exploiting fan-out grating MgO:sPPLT SRO [49]. Recently, wide wavelength tuning was achieved in the mid-IR by using group velocity mismatch (GVM)-optimized tunable pump wavelength for continuous scanning of the non-resonant frequency over several GHz [50]. Towards practical applications of cw SROs, their versatility and sensitivity combined with photoacoustic and cavity ring-down spectroscopy was effectively used in trace-gas sensing [51].

The current focus of the research community is to develop cw OPOs based on highly nonlinear semiconductor crystals like $CdSiP_2$ (CSP), $ZnGeP_2$ (ZGP), and quasi-phase-matched materials such as orientation-patterned gallium arsenide (OP-GaAs), and gallium phosphide (OP-GaP), in order to extend the wavelength tunability of cw OPOs into the deep mid-IR [52]. Demonstration of a single-stage cw OPO based on such semiconductor crystals especially using ZGP and OP-GaAs is challenging because optimum pump laser sources at the desirable wavelength of $\sim$2 µm are rare and most importantly the premium quality semiconductor crystals are still in their developing phase.

During the flourishing era of 1960s for nonlinear optics, several upconversion sources, and most importantly their applications towards imaging were reported [53–55]. However, this area of technology was also hampered by the unavailability of the required nonlinear materials [56]. Only recently, since 2012, upconversion detectors (UCDs) came into effect

[57]. Upconversion detection technique avails the use of simple silicon detectors in order to substitute expensive cryogenically cooled mid-IR detectors, by converting the mid-IR signal to visible/ near-IR using SFG stage. The UCDs offer striking advantages over direct mid-IR detectors namely, high efficiency, low background noise, fast response time, and room-temperature operation. Hence, the development of UCDs for spectroscopy [58] and imaging [59] applications is one of the current hot topics in nonlinear optics. Subsequently, study of noise properties of such UCDs has become equally important [60, 61].

1.2 Overview

Figure 1.2 represents the research outline of this thesis, which consists of two main parts: first, demonstration of cw downconversion sources based on near- and mid-IR OPOs and a mid-IR DFG source; second, introduction to a newly discovered noise source present in short-wavelength-pumped IR upconversion detectors. The commercial, narrow-linewidth, linearly-polarized, cw pump lasers used in this work include a visible diode-pumped solid-state laser at 532 nm and two near-IR fiber lasers at $\sim$1 and $\sim$2 µm. To achieve frequency conversion with maximum efficiency, only quasi-phase-matched nonlinear materials are used. However, the grating period design and poling technique differ from crystal to crystal. The complete experimental characterization of all the devices is performed and reported chapterwise in the thesis. A brief description of the succeeding chapters is given below.

Chapter 2 describes the fundamental concepts of nonlinear optics, primarily associated with three-wave-mixing processes. Starting with an introduction to second-order nonlinear susceptibility, the corresponding coupled-wave equations are derived. Different phase-matching methods are explained and compared in this chapter. Afterwards, important elements of OPO devices are discussed, with focus on resonator design and nonlinear

material considerations for efficient cw OPO operation.

In chapter 3, simple and straightforward wavelength tuning of a cw OPO based on fan-out grating design PPKTP crystal is demonstrated, for the first time, to generate tunable near-IR radiation at a fixed crystal temperature. Firstly, the results of a cw SRO with signal-wave resonating inside the cavity are presented and the experimental data is compared with the different sets of theoretical wavelength tuning curves. Later, the effects of output-coupling of the signal-wave are examined and its effectiveness is proved by discussing the results.

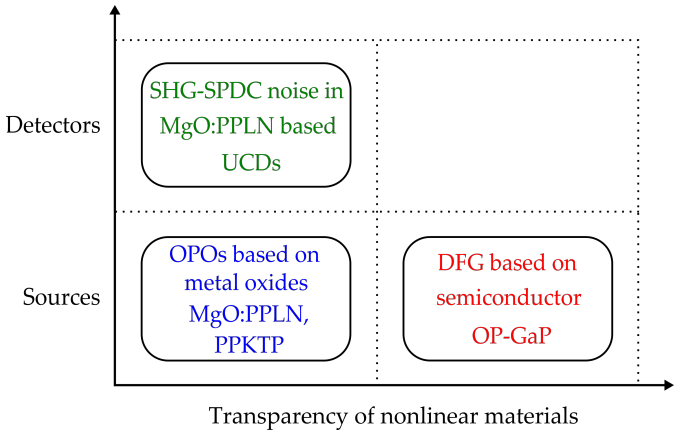

Figure 1.2: Overview of the research work presented in this thesis.

Chapter 4 describes the first demonstration of a DFG source developed for tunable cw mid-IR generation across 4.6-4.7 µm in OP-GaP crystal. The polarization-dependent transmission measurements of the input DFG wavelengths, namely 2.01 µm from Tm-fiber laser and 3.56 µm from MgO:PPLN OPO are presented, followed by the theoretical temperature tuning curves for DFG. Further, experimental results such as DFG power scaling, power stability, tuning spectra and temperature acceptance bandwidth are thoroughly explained.

In chapter 5, state-of-the-art IR upconversion detectors and reports

on noise in such detectors are first reviewed. Then, a novel concept of SHG-SPDC noise is explained and the experimental setup, used for studying noise properties of single-pass short-wavelength-pumped UCDs based on MgO:PPLN crystals, is described. Further, the dependence of SHG-SPDC intensity on the pump power and crystal temperature is experimentally studied and a theoretical model for SHG-SPDC intensity is established. Finally, different noise sources corresponding to telecom and mid-IR UCDs are compared and measures to suppress SHG-SPDC noise are proposed.

Chapter 6 concludes the thesis by highlighting important outcomes of this work and suggests possible improvements to further enhance the device performance. This chapter also provides an insight to the future directions leading to the advancements in the field of cw OPO and upconversion detection technology.

References

[1] T. Maiman, "Stimulated optical radiation in ruby," Nature 187, 493-494 (1960).

[2] S. Stellmer, B. Pasquiou, R. Grimm, and F. Schreck, "Laser cooling to quantum degeneracy," Phys. Rev. Lett. 110, 263003(1-5) (2013).

[3] B. Abbott et al., "Observation of gravitational waves from a binary black hole merger," Phys. Rev. Lett. 116, 061102(1-16) (2016).

[4] N. Picqué and T. Hänsch, "Frequency comb spectroscopy," Nature Photonics 13, 146-157 (2019).

[5] The Nobel Prize in Physics 2018. NobelPrize.org. Nobel Media AB 2019. Mon. 20 May 2019.

[6] W. Silfvast, "Laser Fundamentals," 2nd Ed. Cambridge: Cambridge University Press (2004).

[7] F. Schäfer (ed.), "Dye Lasers," Springer-Verlag Berlin Heidelberg, (1990).

[8] P. Moulton, "Spectroscopic and laser characteristics of Ti:Al_2O_3," J. Opt. Soc. Am. B 3, 125-133 (1986).

[9] J. Faist, F. Capasso, D. Sivco, C. Sirtori, A. Hutchinson, and A. Cho, "Quantum cascade laser," Science 264, 553-556 (1994).

[10] M. Vitiello, G. Scalari, B. Williams, and P. De Natale, "Quantum cascade lasers: 20 years of challenges," Opt. Express 23, 5167-5182 (2015).

[11] S. Ferré, L. Jumpertz, M. Carras, R. Ferreira, and F. Grillot, "Beam shaping in high-power broad-area quantum cascade lasers using optical feedback," Sci. Rep. 7, 44284(1-8) (2017).

[12] A. Johnson, T. Avni, E. Larsen, D. Austin, and J. Marangos, "Attosecond soft X-ray high harmonic generation," Phil. Trans. R. Soc. A 377:20170468 (2019).

[13] J. Kerr, "XL. A new relation between electricity and light: dielectrified media birefringent," Phil. Mag. J. Sci. 4(50), 337-348 (1875).

[14] P. Franken, A. Hill, C. Peters, and G. Weinreich, "Generation of optical harmonics," Phys. Rev. Lett. 7, 118-119 (1961).

[15] J. Giodmaine, "Mixing of light beams in crystals," Phys. Rev. Lett. 8, 19-20 (1962).

[16] M. Bass, P. Franken, A. Hill, C. Peters, and G. Weinreich, "Optical mixing," Phys. Rev. Lett. 8, 18 (1962).

[17] N. Kroll, "Parametric amplification in spatially extended media and application to the design of tunable oscillators at optical frequencies," Phys. Rev., 127, 1207-1211 (1962).

[18] J. Armstrong, N. Bloembergen, J. Ducuing, and P. Pershan, "Interaction between light waves in a nonlinear dielectric," Phys. Rev. 127, 1918-1939 (1962).

[19] A. Smith and N. Braslau, "Observation of an optical difference frequency," J. Appl. Phys. 34, 2105-2106 (1963).

[20] C. Wang and G. Racette, "Measurement of parametric gain accompanying optical difference frequency generation," Appl. Phys. Lett. 6, 169-171 (1965).

[21] J. Giordmaine and R. Miller, "Tunable coherent parametric oscillation in $LiNbO_3$ at optical frequencies," Phys. Rev. Lett. 14, 973-976 (1965).

[22] R. Smith, J. Geusic, H. Levinstein, J. Rubin, S. Singh, and L. Van Uitert, "Continuous optical parametric oscillation in $Ba_2NaNb_5O_{15}$," Appl. Phys. Lett. 12, 308-310 (1968).

[23] R. Byer, M. Oshman, J. Young, and S. Harris, "Visible cw parametric oscillator," Appl. Phys. Lett. 13, 109-111 (1968).

[24] Y. Fan, R. Eckardt, R. Byer, R. Route, and R. Feigelson, "$AgGaS_2$ infrared parametric oscillator," Appl. Phys. Lett. 45, 313-315 (1984).

[25] L. Cheng, W. Bosenberg, and C. Tang, "Broadly tunable optical parametric oscillation in β-BaB_2O_4," Appl. Phys. Lett. 53, 175-177 (1988).

[26] D. Edelstein, E. Wachman, and C. Tang, "Broadly tunable high repetition rate femtosecond optical parametric oscillator," Appl. Phys. Lett. 54, 1728-1730 (1989).

[27] S. Yang, R. Eckardt, and R. Byer, "Continuous-wave singly resonant optical parametric oscillator pumped by a single-frequency resonantly doubled Nd:YAG laser," Opt. Lett. 18, 971-973 (1993).

[28] F. Colville, M. Padgett, and M. Dunn "Continuous-wave, dual-cavity, doubly resonant, optical parametric oscillator," Appl. Phys. Lett. 64, 1490 (1994).

[29] M. Scheidt, B. Beier, R. Knappe, K. Boller, and R. Wallenstein, "Diode laser pumped continuous-wave KTP optical parametric oscillator," J. Opt. Soc. Am. B 12, 2087-2094 (1995).

[30] M. Scheidt, B. Beier, K. Boller, and R. Wallenstein, "Frequency-stable operation of a diode-pumped continuous-wave $RbTiOAsO_4$ optical parametric oscillator," Opt. Lett. 22, 1287-1289 (1997).

[31] F. Colville, M. Dunn, and M. Ebrahim-Zadeh, "Continuous-wave, singly resonant intracavity parametric oscillator," Opt. Lett. 22, 75-79 (1997).

[32] J. Scherer, D. Voelkel, D. Rakestraw, J. Paul, C. Collier, R. Saykally, and A. O'Keefe, "Infrared cavity ringdown laser absorption spectroscopy (IR-CRLAS)," Chem. Phys. Lett. 245, 273-280 (1995).

[33] M. Fejer, G. Magel, D. Jundt, and R. Byer, "Quasi-phasematched second harmonic generation: Tuning and tolerances," IEEE J. Quantum Elect. 28, 2631-2654 (1992).

[34] W. Bosenberg, A. Drobshoff, J. Alexander, L. Myers and R. Byer, "93%-pump depletion, 3.5-W continuous-wave, singly resonant optical parametric oscillator," Opt. Lett. 21, 1336-1338 (1996).

[35] P. Powers, T. Kulp, and S. Bisson, "Continuous tuning of a continuous-wave periodically poled lithium niobate optical parametric oscillator by use of a fan-out grating design," Opt. Lett. 23, 159-161 (1998).

[36] https://www.laserfocusworld.com/lasers-sources/article/16563724/tunable-sources-highpower-cw-opos-span-the-spectrum

[37] A. Henderson and R. Stafford, "Low threshold, singly-resonant CW OPO pumped by an all-fiber pump source," Opt. Express 14, 767-772 (2006).

[38] http://www.radiantis.com/cw-opo-based-laser-system/121-titan.html

[39] I. Breunig, D. Haertle, and K. Buse, "Continuous-wave optical parametric oscillators: recent developments and prospects," Appl. Phys. B 105, 99-111 (2011).

[40] M. Van Herpen, S. Li, S. Bisson, S. te Lintel Hekkert and F. Harren, "Tuning and stability of a continuous-wave mid-infrared high-power single resonant optical parametric oscillator," Appl. Phys. B 75, 329-333 (2002).

[41] M. Vainio, M. Siltanen, J. Peltola, and L. Halonen, "Continuous-wave optical parametric oscillator tuned by a diffraction grating," Opt. Express 17, 7702-7707 (2009).

[42] G. Samanta, S. Kumar, R. Das, and M. Ebrahim-Zadeh, "Continuous-wave optical parametric oscillator pumped by a fiber laser green source at 532 nm," Opt. Lett. 34, 2255-2257 (2009).

[43] S. Kumar and M. Ebrahim-Zadeh, "High-power, continuous-wave, mid-infrared optical parametric oscillator based on MgO:sPPLT," Opt. Lett. 36, 2578-2580 (2011).

[44] G. Samanta and M. Ebrahim-Zadeh, "Continuous-wave, single-frequency, solid-state blue source for the 425-489 nm spectral range," Opt. Lett. 33, 1228-1230 (2008).

[45] K. Devi, S. Kumar, and M. Ebrahim-Zadeh, "Tunable, continuous-wave, ultraviolet source based on intracavity sum-frequency-generation in an optical parametric oscillator using BiB_3O_6," Opt. Express 21, 24829-24836(2013).

[46] S. Kumar, R. Das, G. K. Samanta and M. Ebrahim-Zadeh, "Optimally-output-coupled, 17.5 W, fiber-laser-pumped continuous-wave optical parametric oscillator," Appl. Phys. B 102, 31-35 (2011).

[47] G. Samanta and M. Ebrahim-Zadeh, "Dual-wavelength, two-crystal, continuous-wave optical parametric oscillator," Opt. Lett. 36, 3033-3035 (2011).

[48] K. Devi, S. Kumar, A. Esteban-Martin, and M. Ebrahim-Zadeh, "Antiresonant ring output-coupled continuous-wave optical parametric oscillator," Opt. Express 20, 19313-19321 (2012).

[49] K. Devi and M. Ebrahim-Zadeh, "Room-temperature, rapidly tunable, green-pumped continuous-wave optical parametric oscillator," Opt. Lett. 42, 2635-2638 (2017).

[50] V. Ulvila and M. Vainio, "Diode-laser-pumped continuous-wave optical parametric oscillator with a large mid-infrared tuning range,"Opt. Comm. 439, 99-102 (2019).

[51] D. Arslanov, M. Spunei, J. Mandon, S. Cristescu, S. Persijn, and F. Harren, "Continuous-wave optical parametric oscillator based infrared spectroscopy for sensitive molecular gas sensing," Laser Photonics Rev. 7, 188-206 (2013).

[52] P. Schunemann, K. Zawilski, L. Pomeranz, D. Creeden, and P. Budni, "Advances in nonlinear optical crystals for mid-infrared coherent sources," J. Opt. Soc. Am. B 33, D36-D43 (2016).

[53] J. Midwinter, "Image conversion from 1.6 μm to the visible in lithium niobate," Appl. Phys. Lett. 12, 68-70 (1968).

[54] J. Warner, "Spatial resolution measurements in up-conversion from 10.6 μm to the visible," Appl. Phys. Lett. 13, 360-362 (1968).

[55] R. Boyd and C. Townes, "An infrared upconverter for astronomical imaging," Appl. Phys. Lett. 31, 440-442 (1977).

[56] R. Andrews, "IR image parametric up-conversion," IEEE J. Quantum Electron. QE6, 68-80 (1970).

[57] J. Dam, P. Tidemand-Lichtenberg, and C. Pedersen, "Room-temperature mid-infrared single-photon spectral imaging," Nat. Photonics 6, 788-793 (2012).

[58] P. Tidemand-Lichtenberg, J. Dam, H. Andersen, L. Høgstedt, and C. Pedersen, "Mid-infrared upconversion spectroscopy," J. Opt. Soc. Am. B 33, D28-D35 (2016).

[59] S. Junaid, S. Kumar, M. Mathez, M. Hermes, N. Stone, N. Shepherd, M. Ebrahim-Zadeh, P. Tidemand-Lichtenberg, and C. Pedersen, "Video-rate, mid-infrared hyperspectral upconversion imaging," Optica 6, 702-708 (2019).

[60] L. Meng, L. Høgstedt, P. Tidemand-Lichtenberg, C. Pedersen, and P. Rodrigo, "Enhancing the detectivity of an upconversion single-photon detector by spatial filtering of upconverted parametric fluorescence," Opt. Express 26, 24712-24722 (2018).

[61] A. Barh, P. Tidemand-Lichtenberg, and C. Pedersen, "Thermal noise in mid-infrared broadband upconversion detectors," Opt. Express 26, 3249-3259 (2018).

Chapter 2

Basics of nonlinear optics

2.1 Introduction to optical nonlinearity

The properties of light and its interaction with matter is studied in nonlinear optics. As a consequence of incident light, electrons in a transparent dielectric medium are displaced with respect to their nuclei due to the applied electric field, and dipole moment per unit volume is induced. Oscillations of the induced dipoles result into the emission of electromagnetic waves. Optical response of a material scales linearly when amplitude of the incident radiation is small, given by instantaneous polarization

$$\boldsymbol{P} = \epsilon_0 \boldsymbol{\chi}^{(1)} \boldsymbol{E} \tag{2.1}$$

where $\boldsymbol{E}$ is the incident electric field, ϵ_0 is the electric permittivity of free space, and $\boldsymbol{\chi}^{(1)}$ is the linear electric susceptibility which determines refractive index, absorption and birefringence properties of the material. In this case, the waves emitted from the dipoles have same frequency as that of the applied field. The phenomena such as refraction, diffraction and dispersion are usually observed under low-intensity light-matter interactions. However, material properties change rapidly if the incident field strengths are of the order of intra-atomic electric field. Under this condition, the dipoles oscillate not only at the input frequency but also above and below it, which leads to the effects such as harmonic generation, frequency-mixing and self-focusing. The nonlinear optical response of the material can be described by expressing the total induced polarization as a power series in the applied electric field [1]

$$\boldsymbol{P} = \epsilon_0 (\boldsymbol{\chi}^{(1)} \boldsymbol{E} + \boldsymbol{\chi}^{(2)} \boldsymbol{E}^2 + \boldsymbol{\chi}^{(3)} \boldsymbol{E}^3 + ...) \tag{2.2}$$

where $\boldsymbol{\chi}^{(2)}$ and $\boldsymbol{\chi}^{(3)}$ represent the second and third-order nonlinear electric susceptibilities. Higher-order terms in equation 2.2 are responsible for the generation of new oscillation frequencies. In general, the electric susceptibility of an anisotropic medium is defined as a tensor $\boldsymbol{\chi}^{(n)}$ of rank n+1 involving n+1 interacting waves. Work presented in this thesis is based on the second-order nonlinearity, realized through different frequency-mixing processes in $\chi^{(2)}$ materials, hence basics of the same are discussed in this chapter.

2.2 Second-order nonlinear optical processes

Deducing from the previous section, second-order nonlinear optical processes involve three waves. If an applied electric field consists of two distinct frequency components ω_1 and ω_2, which is represented by

$$\boldsymbol{E} = \boldsymbol{E}_1 \mathrm{e}^{-\mathrm{i}\omega_1 t} + \boldsymbol{E}_2 \mathrm{e}^{-\mathrm{i}\omega_2 t} + c.c. \tag{2.3}$$

then the induced second-order nonlinear polarization is given by

$$\begin{aligned}
\boldsymbol{P}^{(2)} &= \epsilon_0 \boldsymbol{\chi}^{(2)} \boldsymbol{E}.\boldsymbol{E} && (2.4)\\
&= \epsilon_0 \boldsymbol{\chi}^{(2)} \boldsymbol{E}_1.\boldsymbol{E}_1 \mathrm{e}^{-2\mathrm{i}\omega_1 t} + \epsilon_0 \boldsymbol{\chi}^{(2)} \boldsymbol{E}_2.\boldsymbol{E}_2 \mathrm{e}^{-2\mathrm{i}\omega_2 t} && (2.5)\\
&+ 2\epsilon_0 \boldsymbol{\chi}^{(2)} \boldsymbol{E}_1.\boldsymbol{E}_2 \mathrm{e}^{-\mathrm{i}(\omega_1+\omega_2)t} && (2.6)\\
&+ 2\epsilon_0 \boldsymbol{\chi}^{(2)} \boldsymbol{E}_1.\boldsymbol{E}_2^* \mathrm{e}^{-\mathrm{i}(\omega_1-\omega_2)t} && (2.7)\\
&+ 2\epsilon_0 \boldsymbol{\chi}^{(2)} (\boldsymbol{E}_1.\boldsymbol{E}_1^* + \boldsymbol{E}_2.\boldsymbol{E}_2^*) + c.c. && (2.8)
\end{aligned}$$

Equation 2.5 represents a process called second-harmonic-generation (SHG) as exponents of its terms are proportional to twice the input frequencies. While the exponents in equation 2.6 and 2.7 are proportional to the sum and difference of the input frequencies, representing the phenomena of sum-frequency-generation (SFG) and difference-frequency-generation (DFG), respectively. Equation 2.8 is related to optical rectification and complex conjugates (*c.c.*) do not lead to any extra processes.

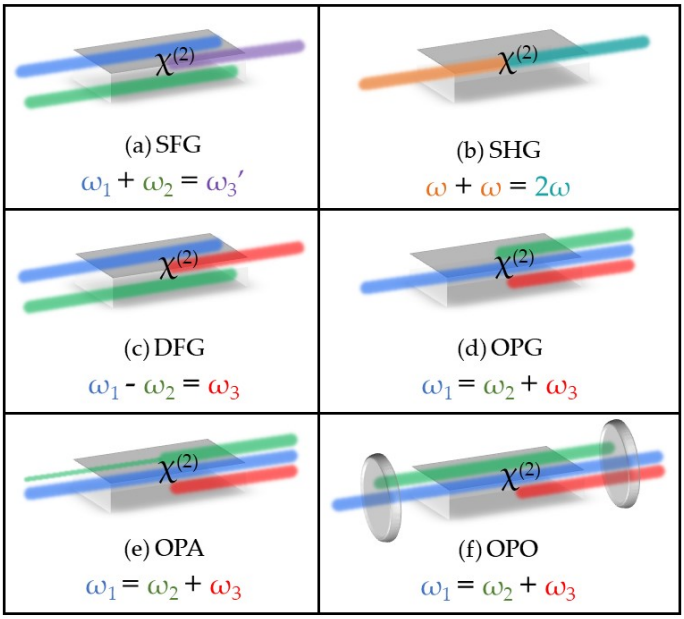

Figure 2.1: Schematic of second-order optical nonlinear processes.

Figure 2.1 illustrates different types of frequency conversion processes taking place in $\chi^{(2)}$ nonlinear materials, where $\omega_1 > \omega_2 > \omega_3$. In all the processes, energy of the interacting photons is conserved. In SFG (Figure 2.1 (a)), two photons at frequencies ω_1 and ω_2 are combined to generate a higher-energy photon at frequency, $\omega_{3'} = \omega_1 + \omega_2$. Hence, it is called upconversion process. SHG is the degenerate case of SFG, where two photons of frequency ω combine to produce a single photon at 2ω, as shown in Figure 2.1 (b). While DFG (Figure 2.1 (c)) involves two input photons at ω_1 and ω_2 and generates a lower-energy photon at frequency $\omega_3 = \omega_1 - \omega_2$. Therefore, it is called downconversion process. A special case of DFG is known as optical rectification, where two input photons of same frequency combine to generate static electric field within the nonlinear medium. Another type of the downconversion process is called spontaneous parametric downcon-

version (SPDC) or optical parametric generation (OPG), in which a pump photon at ω_1 spontaneously splits into two new photons of lower-frequency ω_2 and ω_3, where $\omega_1 = \omega_2 + \omega_3$, as seen in Figure 2.1 (d). By convention, of the two generated photons, the one with higher frequency is called the signal, and the one with lower frequency the idler. The downconverted photons in OPG are generated out of the interaction between a strong pump field and quantum vacuum fluctuations [2]. Hence, the output of the OPG process is relatively weak. In order to achieve macroscopic amplification, an *optical parametric amplification* (OPA) stage is usually employed in which signal is used as a weak seed as shown in Figure 2.1 (e).

If the nonlinear material is contained within a Fabry-Perot resonator to provide optical feedback to OPG, the resulting device is called an optical parametric oscillator (OPO) as sketched in Figure 2.1 (f). An optical cavity is used to enhance the efficiency of the OPG by resonating at least one of the generated waves. The OPO significantly improves the conversion efficiency of a parametric process, even at low pump intensity operation in continuous-wave (cw) regime. It is considered as the most efficient device of producing tunable frequency output from a single input beam [3]. The fundamentals of cw OPOs will be discussed thoroughly in the last section of this chapter. The work presented in this thesis is based on developing cw sources such as OPOs, DFG, and SFG.

2.3 Second-order nonlinear susceptibility

Nonlinear interactions typically take place in crystalline media whose optical susceptibility tensor is dictated by spatial symmetry of the crystal structure [4]. Second-order nonlinearity can be observed only if the crystal potential is asymmetric in some direction i.e. the crystal must not have an inversion symmetry (*a non-centrosymmetric* crystal). The quadratic susceptibility tensor has 27 frequency-dependent coefficients and are denoted by $\chi^{(2)}_{ijk}$, where indices *i, j, k* refer to Cartesian coordinates *x, y ,z* representing the polarization directions. They are often expressed in terms of d-coefficients defined as,

$$d_{ijk} = \frac{1}{2}\chi^{(2)}_{ijk} \tag{2.9}$$

The intrinsic permutation symmetry allows the indices of $\chi^{(2)}_{ijk}$ to be permuted as long as the frequencies of the interacting waves are permuted simultaneously [5]. Further, using following symmetry properties $\boldsymbol{d}$-tensor can be conveniently expressed in the form of 3X6 matrix with coefficients d_{il}. As a rule of thumb, the nonlinear crystal used for frequency mixing should be transparent over the entire range of involved optical frequencies, hence all components of the $\boldsymbol{\chi}^{(2)}$ tensor are real. Additionally, the condition of full permutation symmetry can be applied to a lossless medium, according to which all frequency arguments of the nonlinear susceptibility can be freely swapped as long as the corresponding Cartesian indices are swapped simultaneously [6]. Subsequently, Kleinman's symmetry condition is applicable when all the corresponding frequencies are much lower than the lowest resonance frequency of the medium [7]. In this case the nonlinear susceptibility is essentially independent of the frequency term. Full permutation symmetry also applies. Therefore, it is possible to permute the indices without permuting the interacting frequency terms.

After evoking different symmetry relations the $\boldsymbol{d}$-tensor reduces down to 10 independent coefficients. Using equation 2.4, the second order

nonlinear polarization at output frequency ω_3 can be expressed as

$$\begin{pmatrix} P_x^{(2)}(\omega_3) \\ P_y^{(2)}(\omega_3) \\ P_z^{(2)}(\omega_3) \end{pmatrix} = 2\epsilon_0 K \begin{pmatrix} d_{11} & d_{12} & d_{13} & d_{14} & d_{15} & d_{16} \\ d_{21} & d_{22} & d_{23} & d_{24} & d_{25} & d_{26} \\ d_{31} & d_{32} & d_{33} & d_{34} & d_{35} & d_{36} \end{pmatrix} \begin{pmatrix} E_x(\omega_1)E_x(\omega_2) \\ E_y(\omega_1)E_y(\omega_2) \\ E_z(\omega_1)E_z(\omega_2) \\ E_y(\omega_1)E_z(\omega_2) + E_z(\omega_1)E_y(\omega_2) \\ E_x(\omega_1)E_z(\omega_2) + E_z(\omega_1)E_x(\omega_2) \\ E_x(\omega_1)E_y(\omega_2) + E_y(\omega_1)E_x(\omega_2) \end{pmatrix} \tag{2.10}$$

where K is the degeneracy factor, whose value depends on the conversion processes.

For a given nonlinear material with certain crystal lattice symmetry, the number of independent elements of the ***d***-tensor can be further reduced. For example, the negative uniaxial birefringent crystal lithium niobate ($LiNbO_3$) belongs to the point group 3m and its d_{il} matrix has only 3 independent elements [8], given by

$$d_{il} = \begin{pmatrix} 0 & 0 & 0 & 0 & d_{31} & -d_{22} \\ -d_{22} & d_{22} & 0 & d_{31} & 0 & 0 \\ d_{31} & d_{31} & d_{33} & 0 & 0 & 0 \end{pmatrix} \tag{2.11}$$

In practice, the second-order nonlinear susceptibility is denoted in terms of a scalar quantity. In general, d_{eff} (*effective nonlinear coefficient*) is a sum of terms obtained through the contraction treatment. For a given frequency-mixing process, d_{eff} is calculated based on the polarization and propagation direction of the interacting optical waves, and the geometry of the nonlinear crystal.

2.4 Coupled-wave equations in second-order nonlinear processes

The second-order optical nonlinear effects are governed by Maxwell's equations in the non-centrosymmetric crystals. The solution of Maxwell's equations describes the energy transfer between involved electromagnetic waves and their propagation in a $\chi^{(2)}$ nonlinear medium [6]. While the direction of the energy flow in a three-wave mixing process depends on the relative phase and intensity of the input fields. The nonlinear material is assumed to be transparent for all interacting waves. It is also considered to be non-magnetic ($\boldsymbol{M} = 0$) and non-conducting, which contains neither free charges ($\rho = 0$) nor free currents ($\boldsymbol{J} = 0$). Under the mentioned criteria, the Maxwell's macroscopic equations are,

$$\begin{aligned} \boldsymbol{\nabla} \cdot \boldsymbol{D} &= 0 \\ \boldsymbol{\nabla} \cdot \boldsymbol{B} &= 0 \\ \boldsymbol{\nabla} \times \boldsymbol{E} &= -\frac{\partial \boldsymbol{B}}{\partial t} \\ \boldsymbol{\nabla} \times \boldsymbol{H} &= \frac{\partial \boldsymbol{D}}{\partial t} \end{aligned} \tag{2.12}$$

where the electric flux density $\boldsymbol{D}$ is expressed in terms of the induced polarization as, $\boldsymbol{D} = \epsilon_0 \boldsymbol{E} + \boldsymbol{P}$. The magnetic flux density $\boldsymbol{B}$ can be written in terms of the magnetic field $\boldsymbol{H}$, as $\boldsymbol{B} = \mu_0 \boldsymbol{H}$, where μ_0 is the magnetic permeability of the free space, and the speed of light $c = \sqrt{\epsilon_0 \mu_0}$. By using these equations together with the vector identity operations, the following wave equation can be derived which shows the evolution of the electric fields as they propagate through the nonlinear dielectric medium.

$$\boldsymbol{\nabla}^2 \boldsymbol{E} = \frac{n^2}{c^2} \frac{\partial^2 \boldsymbol{E}}{\partial t^2} + \mu_0 \frac{\partial^2 \boldsymbol{P}}{\partial t^2} \tag{2.13}$$

The total electric field in a lossless nonlinear medium is assumed to consists of three travelling plane waves along an arbitrary chosen direction z, with

frequencies ω_j; j=1,2,3 and $\omega_3 > \omega_2 > \omega_1$

$$\boldsymbol{E}_j(z,t) = E_j(z,\omega_j)\mathrm{e}^{\mathrm{i}(k_j z - \omega_j t)} + c.c. \tag{2.14}$$

and the nonlinear source term is given by

$$\boldsymbol{P}_j(z,t) = P_j(z,\omega_j)\mathrm{e}^{\mathrm{i}(k_j z - \omega_j t)} + c.c. \tag{2.15}$$

where wavenumber k_j is expressed in terms of frequency dependent refractive index n_j

$$k_j = \frac{n_j(\omega_j)\omega_j}{c} \tag{2.16}$$

After substituting equations 2.14 and 2.15 into equation 2.13, *slowly varying envelope approximation* (SVEA) is applied [9], which states that the second-order derivatives can be ignored as the amplitude of electric field varies slowly in space over a distance comparable to the optical wavelength

$$\left|\frac{\mathrm{d}^2 E_j}{\mathrm{d}dz^2}\right| << \left|k_j \frac{\mathrm{d}E_j}{\mathrm{d}z}\right| \tag{2.17}$$

This treatment produces three *coupled-amplitude equations* for each interacting wave,

$$\frac{\mathrm{d}E_1}{\mathrm{d}z} = \frac{2\mathrm{i}\omega_1^2 d_{\mathrm{eff}}}{k_1 c^2} E_3 {E_2}^* \mathrm{e}^{\mathrm{i}\Delta k z} \tag{2.18}$$

$$\frac{\mathrm{d}E_2}{\mathrm{d}z} = \frac{2\mathrm{i}\omega_2^2 d_{\mathrm{eff}}}{k_2 c^2} E_3 {E_1}^* \mathrm{e}^{\mathrm{i}\Delta k z} \tag{2.19}$$

$$\frac{\mathrm{d}E_3}{\mathrm{d}z} = \frac{2\mathrm{i}\omega_3^2 d_{\mathrm{eff}}}{k_3 c^2} E_1 E_2 \mathrm{e}^{-\mathrm{i}\Delta k z} \tag{2.20}$$

where, phase-mismatch $\Delta k = k_3 - k_2 - k_1$ represents the degree of phase velocity mismatch between the three waves.

For a downconversion process with constant input fields E_3 and E_2, output field amplitude at the exit plane of a nonlinear crystal of length L can be calculated by integrating equation 2.18 from z = 0 to L. Then the output beam intensity is given by,

$$I_1 = 2n_1\epsilon_0 c|E_1|^2 \tag{2.21}$$

$$= \frac{8d_{\text{eff}}^2\omega_1 I_2 I_3}{n_1 n_2 n_3 \epsilon_0 c^2}\,\text{sinc}^2\left(\frac{\Delta kL}{2}\right) \tag{2.22}$$

It implies that the intensity of the downconverted wave is maximum at Δk = 0, which is known as perfect phase-matching condition. Whereas if $\Delta k \neq 0$ i.e. for increasing phase-mismatch, output intensity decreases with oscillatory behaviour. The period of oscillations is defined as *coherence length* and is given by

$$L_{\text{c}} = \frac{\pi}{\Delta k} \tag{2.23}$$

It is a measure of the maximum interaction length over which the energy flows from the driving polarization to the generated radiation by maintaining the phase-relation between interacting waves inside the nonlinear crystal.

2.5 Parametric gain and amplification

In the three-wave mixing processes, the pump field is usually much stronger than the generated fields. Hence, it is assumed that the input pump field E_3 does not undergo strong depletion and its variation throughout the crystal can be neglected i.e. left hand side of equation 2.20 is zero. Therefore, the coupled-wave equations are reduced to two, with E_3 being independent of z in both equations 2.18 and 2.19. Under the phase-matching condition, parametric noise is amplified during its propagation through the nonlinear crystal. For a non-zero input signal $E_2 \neq 0$, the single-pass parametric gain

in the crystal of length L is given by [10]

$$G_2(L) = \frac{I_2(L)}{I_2(0)} - 1 \tag{2.24}$$

$$= \Gamma^2 L^2 \frac{\sinh^2\left(\sqrt{\Gamma^2 L^2 - \left(\frac{\Delta k L}{2}\right)^2}\right)}{\Gamma^2 L^2 - \left(\frac{\Delta k L}{2}\right)^2} \tag{2.25}$$

where Γ is the gain factor defined as

$$\Gamma^2 = \frac{8\pi^2 d_{\text{eff}}^2}{n_1 n_2 n_3 \epsilon_0 c \lambda_1 \lambda_2} I_3(0) \tag{2.26}$$

where λ_j is wavelength and $\lambda_1 > \lambda_2 > \lambda_3$.

For the perfect phase-matching condition, the single-pass gain increases exponentially with $2\Gamma L$ in the high-gain limit ($\Gamma L >> 1$). The high-gain limit is valid for parametric generation using high-intensity, pulsed, and amplified laser pump sources.

2.6 Phase-matching condition

As seen in section 2.4, the phase-matching condition has to be fulfilled to achieve optimal energy conversion. Ideally, the coherence length should be longer than the length of a crystal. However, the three optical fields at different frequencies fail to maintain the phase velocity synchronization inside the nonlinear crystal due to material dispersion. Hence, phase-matching techniques are actively employed to make $\Delta k = 0$. Phase-matching refers to fixing the relative phase velocity mismatch between the interacting waves, as the waves propagate through the crystal. In the OPO system, phase-mismatch is determined by

$$\Delta k = \frac{n_{\text{p}}(\lambda_{\text{p}}, T)}{\lambda_{\text{p}}} - \frac{n_{\text{s}}(\lambda_{\text{s}}, T)}{\lambda_{\text{s}}} - \frac{n_{\text{i}}(\lambda_{\text{i}}, T)}{\lambda_{\text{i}}} \tag{2.27}$$

where the wavelength and crystal temperature dependent linear refractive indices are determined using Sellmeier equations for a given nonlinear crystal. Traditionally, phase-matching is controlled by exploiting natural birefringence of the optically anisotropic crystals to compensate for dispersion, this method is referred to as *birefringent phase-matching* (BPM). Another technique, known as quasi-phase-matching (QPM) relies on periodic reversal of the electric dipole domains in ferroelectric materials and epitaxy growth techniques for controlled lattice inversion in semiconductor materials. In both methods, wavelength tuning in the parametric device is achieved by varying the temperature of the crystal.

Birefringent phase-matching

As the refractive index of the crystal depends on the light polarization and its propagation direction relative to the crystal lattice, the perfect phase-matching can be obtained by choosing these parameters properly. If the crystal has a single optic axis in z-direction, then $n_x = n_y \neq n_z$, i.e. refractive index of a beam polarized in xy-plane is independent of the propagation direction and it is termed as *ordinary ray* (o-ray). The orthogonal counterpart of o-ray is called *extraordinary ray* (e-ray) which depends on the polarization. Thus, in the *uniaxial crystals*, the refractive index distribution is a sphere of radius n_o for o-ray and a spheroid of semi-axes n_o and n_e for e-ray, which is given by the index ellipsoid equation

$$\frac{1}{{n_\mathrm{e}}^2(\theta)} = \frac{\sin^2(\theta)}{{n_\mathrm{e}}^2} + \frac{\cos^2(\theta)}{{n_\mathrm{o}}^2} \tag{2.28}$$

where θ is the angle between the e-ray polarization and the optic axis. By selecting the polarization directions of interacting beams for e-ray, the angle θ can be varied until equation 2.28 is balanced and the wavelength tuning is realized through angle tuning.

Figure 2.2 represents two types BPM for SHG process in a negative

uniaxial birefringent crystal (n_e<n_o). Figure 2.2 (a) refers to *critical phase-matching* (CPM) ($0 < \theta < 90^o$), where Poynting vector ($\boldsymbol{s}$) propagating in the anisotropic crystal diverges from the wave vector ($\boldsymbol{k}$) leading to spatial walk-off angle (ρ). The spatial walk-off can become large enough that beam overlap is lost over the full length of the crystal, reducing the effective interaction length. However, as seen from Figure 2.2 (b), spatial walk-off can be completely removed under *non-critical phase-matching* (NCPM), as $\boldsymbol{s}$ is always parallel to $\boldsymbol{k}$ for $\theta = 90^o$.

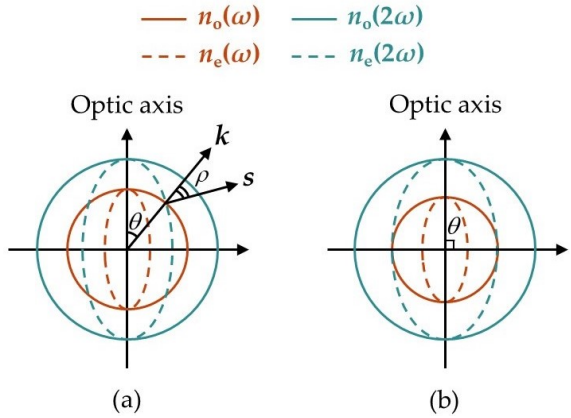

Figure 2.2: (a) Critical and (b) non-critical phase-matching in a negative birefringent crystal.

Quasi-phase-matching

The BPM technique is not applicable when the material does not possess sufficient birefringence to compensate for the refractive index difference due to the dispersion. Moreover, BPM suffers from following limitations, the polarization directions that are suitable for phase-matching do not usually produce the highest possible nonlinearity, NCPM is often impossible as wavelength tuning relies only on temperature tuning and hence CPM is used, however it leads to spatial separation of the beams due to the

Poynting vector walk-off limiting the interaction length and conversion efficiency. Instead of trying to match the phase velocity of the pump and generated beams throughout the entire bulk crystal, an alternative technique of quasi-phase-matching is deployed under such circumstances. QPM can be achieved by periodically changing the sign of the nonlinear susceptibility tensor at each coherence length of the crystal. Thus, the phase of induced polarization shifts by 180^{o} after each L_c, forcing the interacting waves to be in phase along the propagation direction [11]. The additional phase is known as grating period Λ, and it corresponds to twice the coherence length of the crystal ($\Lambda = 2L_c$). Depending on the frequency-mixing process, the nonlinear crystal can be structured for grating periods having a wide range of lengths from a few micrometers to hundreds of micrometers, with different grating designs as shown in Figure 2.3.

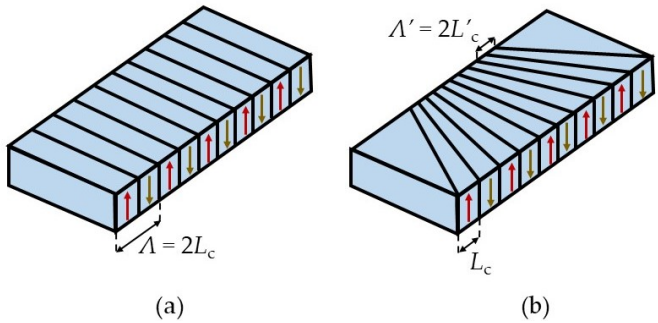

Figure 2.3: (a) Uniform and (b) fan-out grating design in a quasi-phase-matched nonlinear crystal.

Following equation 2.27, the phase-matching condition for QPM is modified to include the grating period wavevector as,

$$\Delta k = \frac{n_p(\lambda_p, T)}{\lambda_p} - \frac{n_s(\lambda_s, T)}{\lambda_s} - \frac{n_i(\lambda_i, T)}{\lambda_i} - \frac{2\pi m}{\Lambda} \tag{2.29}$$

where coefficient m is referred to as QPM order. The effective nonlinear

coefficient for the quasi-phase-matched interaction is given by

$$d_m = \frac{2}{m\pi} d_{eff} \tag{2.30}$$

which implies that higher order QPM is associated with lower effective nonlinearity. Wavelength tuning in quasi-phase-matched devices is essentially achieved via grating period tuning. The engineering flexibility in fan-out grating design allows rapid wavelength tuning as grating periods continuously vary from Λ' to Λ, along the width of the crystal, as shown in Figure 2.3 (b).

QPM permits the use of the same polarization direction for all interacting waves, accessing the highest diagonal d_{il} coefficient. Collinear propagation assures maximum overlap between the waves, resulting in longer effective interaction length throughout the crystal. Furthermore, QPM can also be applicable to nonlinear crystals that are not birefringent but have a very high nonlinear coefficients. Depending on the type of the nonlinear material, the QPM gratings can be fabricated using following two methods.

(a) Periodic poling

Periodic poling is a technique used to realize popular QPM engineered ferroelectric oxide crystals such as PPLN ($LiNbO_3$), PPLT ($LiTaO_3$) and PPKTP ($KTiOPO_4$). The poling procedure for $LiNbO_3$ is described in [12] and the main production steps are illustrated in Figure 2.4. First the grating period is determined and its pattern is transferred to the crystal by photolithography. After removing the photoresist an intense electric field is applied to the crystal using patterned electrodes designed for the given grating period. When the applied voltage exceeds the coercive field, permanent domain reversal occurs and a periodic structure of alternating polarity is formed.

The nature of domain reversal process limits the aperture size of the periodically poled crystal. If the domain structures is too thin or the

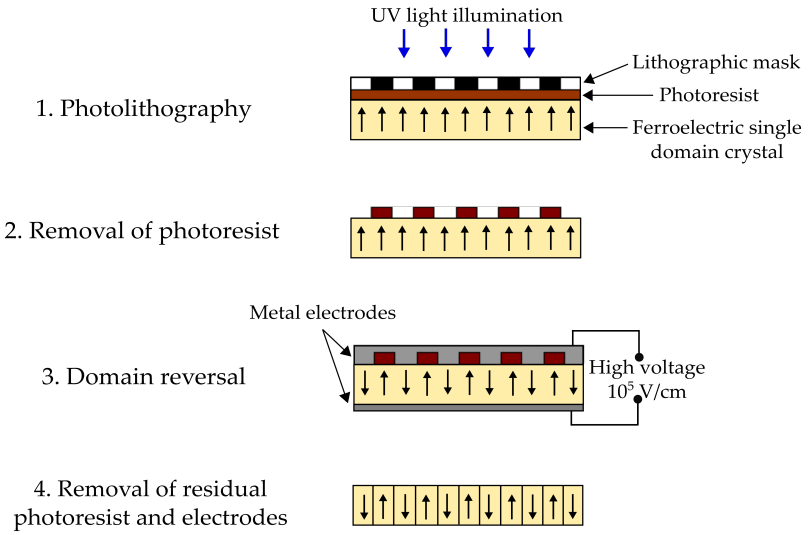

Figure 2.4: Process of periodic inversion of the sign of the nonlinear coefficient.

voltage is too high the current will spark through the crystal across several grating periods, whereas if the crystal is too thick the voltage may not be high enough for a complete domain reversal. In the course of poling process, both photolithography and domain inversion can cause stochastic errors in the grating position. As a consequence of such errors, unintended parametric processes are observed in the quasi-phase-matched crystals under intense pumping.

(b) Orientation patterning

The method called orientation patterning is used for growing periodic quasi-phase-matching domain structure on the non-ferroelectric semiconductor crystals such as GaAs and GaP. The growth technique for OP-GaP is described in [13] and is depicted in Figure 2.5. First a thin layer of silicon is

grown on GaP wafer. Then on a thin layered GaP (-) of inverted orientation with respect to the substrate GaP (+) is grown using on polar-on-nonpolar molecular beam epitaxy (MBE). Then GaP (-) layer is lithographically patterned using the photoresist of desired grating period length. Later, it is chemically etched back to the original bulk GaP (+) substrate. In the last step, grating structure is vertically extended over several hundred microns using hydride vapour phase epitaxy (HVPE) process. Here, silicon is used as a lattice-matched non-polar layer. A high quality all-epitaxial grown material with substantial thickness can be obtained, as long as precise vertical domain propagation is maintained over the required thickness of the crystal. Impurities in the bulk semiconductor substrate or that are originated during the fabrication of the quasi-phase-matched layer, can lead to linear absorption losses in the orientation-patterned crystals.

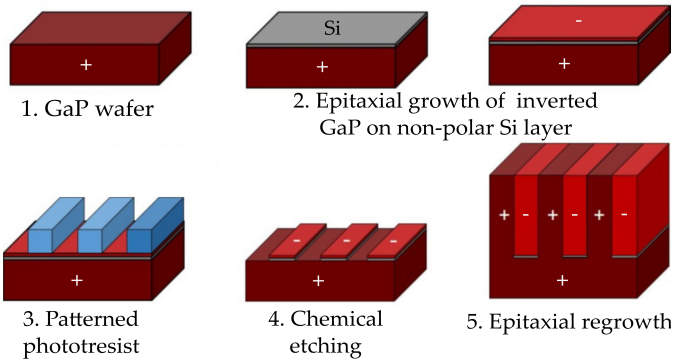

Figure 2.5: Process of orientation patterning during the growth of OP-GaP crystal.

In order to compare BPM and QPM, normalized intensity of the generated wave as a function of propagation distance over the crystal length for non-phase-matched ($\Delta k \neq 0$), perfectly phase-matched ($\Delta k = 0$), and quasi-phase-matched conditions is shown in Figure 2.6. Unlike BPM, QPM is not a perfect phase-matching method. For a given d_{eff} value, output intensity grows rapidly under BPM condition, however high intensity sustains

only for a part of the crystal length. Whereas, for the same d_{eff} value, QPM gradually builds up intensity to deliver the maximum intensity at the exit plane of the crystal. Hence, QPM is considered to be more efficient.

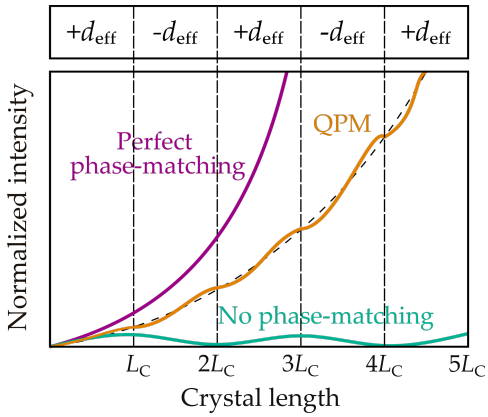

Figure 2.6: Illustration of perfectly birefringent phase-matching, quasi-phase-matching, and no-phase-matching conditions.

2.7 Continuous-wave optical parametric oscillators

As illustrated in Figure 2.1 (f), an OPO is a device based on a nonlinear crystal enclosed in an optical resonator. The crystal is pumped by an intense input pump field and at least one of the generated waves is resonated in the OPO cavity to provide macroscopic amplification of the downconverted fields. The parametric processes are effectively instantaneous, where no energy is stored inside the nonlinear crystal. The OPOs can be operated at all time-scales from cw to ultrafast, where temporal qualities of the pump laser are transferred to the output beams. The characteristics of cw OPOs are discussed in the following subsections.

Under perfect phase-matching, equation 2.25 for single-pass signal gain reduces to

$$G_s(L) = \sinh^2(\Gamma L) \tag{2.31}$$

For low gain ($\Gamma L \lesssim 1$), it approximates to

$$G_s(L) \cong \Gamma^2 L^2 \tag{2.32}$$

which implies that the single-pass signal gain has a quadratic dependence on ΓL in the low-gain limit. Experimentally, the low-gain limit corresponds to parametric generation when using cw pump sources.

2.7.1 Oscillator configurations

For a given pump power and a nonlinear crystal, efficient operation of an OPO requires substantial gain at the parametric waves to overcome losses in the cavity. The losses mainly originate from the limitations on purity of the cavity mirror coatings. Additionally, linear absorption in the crystal and scattering losses also contribute. Hence, in order to maintain the necessary parametric gain, at least one of the generated waves are resonated inside the optical cavity while extracting the waves of interest. Four major oscillator configurations are used, depending on the number of resonating waves.

In a singly-resonant oscillator (SRO), either signal or idler is resonated while the other one is completely extracted from the cavity together with the transmitted pump. Resonating signal is the most widely used OPO configuration as shown in the Figure 2.1 (f), because of the availability of high-quality mirror coatings for shorter wavelengths as compared to the longer idler wavelengths. The doubly-resonant oscillator (DRO) resonates both signal and idler while the undepleted pump is extracted. In a triply-resonant oscillator (TRO), all three waves are resonated. To enhance the efficiency by increasing the pump intensity, another configuration known as pump-enhanced SRO (PE-SRO) is used, where one of the generated waves is resonated together with the pump inside the OPO cavity.

The pump threshold can be significantly reduced by designing DRO and TRO cavities, which is desirable particularly for cw operation. However, continuous wavelength tuning of such OPOs is complicated compared to SROs. On the other hand, in spite of the high operation threshold, SROs provide single-frequency output with stable performance.

2.7.2 Steady-state SRO threshold

Similar to a conventional laser oscillator, an OPO is also characterised by a threshold condition. It is defined by the pumping intensity at which the growth of the parametric waves in one round-trip of the optical cavity balances the total loss in that round-trip. The pump power oscillation threshold is an important parameter for cw OPOs under low-gain pumping. The steady-state SRO threshold can be calculated considering plane-wave and undepleted pump approximations, and by assuming phase-matched interaction under single-pass of the pump. If the signal is resonating in the cavity, then the pump intensity required to reach the oscillation threshold is expressed as

$$I_{\text{th}} = \frac{\alpha_s c \epsilon_0 n_p n_s n_i \lambda_s \lambda_i}{8\pi^2 L^2 d_{\text{eff}}^2} \tag{2.33}$$

where α_s is the fractional round-trip power loss signal wave in the SRO configuration.

2.7.3 Cavity design

The successful operation of an OPO requires an optimum cavity design, in which mode of the resonant beam is matched to the pump mode at the centre of the nonlinear crystal. The typical cavity configurations used in OPOs are shown in Figure 2.7 . The linear cavity, V-cavity and X-cavity are standing wave cavities, while the ring cavity is a travelling wave cavity. The ring cavity provides essentially the same OPO performance as the

four-mirror linear design. However, OPO operation threshold of the ring resonator is lesser than the four-mirror standing-wave resonator [14].

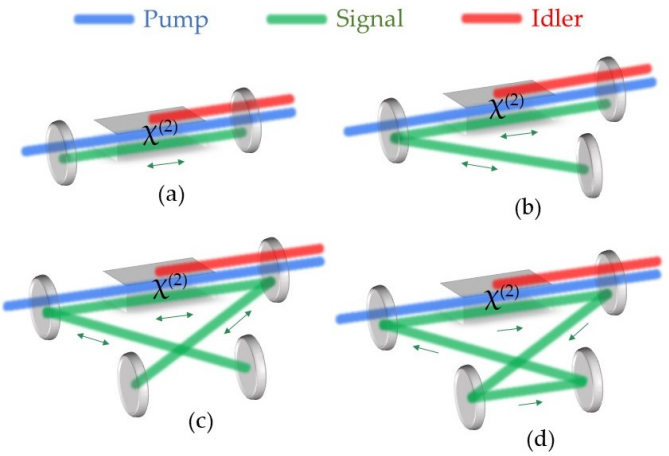

Figure 2.7: OPO resonator cavity designs: (a) linear cavity, (b) V-cavity, (c) X-cavity, (d) ring cavity.

The linear cavity is commonly used in nanosecond OPOs, whereas V-cavity and X-cavity are typically used in ultrafast OPOs. In order to achieve a stable single-frequency operation, a unidirectional ring cavity is preferred in a cw SRO configuration. In context to cw OPOs, the ring cavity design offers advantages such as, losses due to the material absorption and crystal coatings are reduced because the resonating wave travels only single-pass every round-trip, the possibility of introducing etalon for frequency selection or suitable nonlinear crystals for intracavity frequency conversion at the second beam waist of the cavity. Additionally, optical isolator is not required as ring cavity eliminates back-reflections into the pump laser.

To design the above mentioned cavities, ABCD matrix is used for calculating the effect of optical elements on the interacting waves. Using the Gaussian beam transformation matrices, the signal waist can be calculated at any position in the cavity.

2.7.4 Nonlinear material and phase-matching bandwidths

When selecting a nonlinear crystal material for an OPO, several important parameters have to be taken into account. This includes a broad transparency range, high optical damage threshold, good thermal conductivity, phase-matching possibility in the wavelength range of interest, mechanical hardness, chemical stability, high nonlinear *figure-of-merit*, availability in high quality and large size. Physical parameters of a nonlinear material are represented in terms of figure-of-merit as,

$$FOM = \frac{d_{\text{eff}}}{\sqrt{n_{\text{p}} n_{\text{s}} n_{\text{i}}}} \tag{2.34}$$

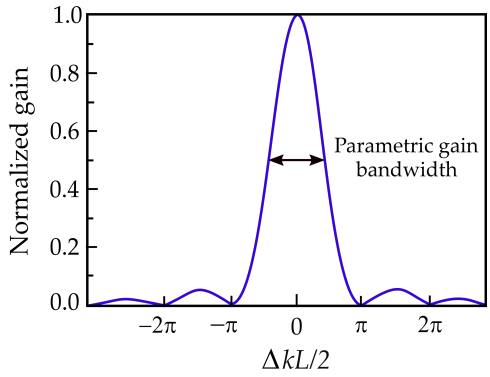

Figure 2.8: The dependence of parametric gain on the phase-mismatch parameter.

Another crucial parameter associated with the nonlinear material is its parametric gain bandwidth, as it indicates the maximum tolerance to possible finite deviations in the pump linewidth, angular divergence of the pump beam and phase-matching temperature. The spectral ($\Delta\lambda_{\text{p}}$), angular ($\Delta\theta$) and temperature (ΔT) acceptance bandwidths for a given experimental parameters can be calculated using the Taylor-series expansion of Δk for the pump wavelength, angular spread of the pump beam, and phase-matching temperature of the crystal, respectively [15]. For attainment of the maximum parametric gain and minimum OPO threshold, the use of nonlinear material

with large $\Delta\lambda_p$, $\Delta\theta$ and ΔT is advisable. As shown in Figure 2.8, sinc^2 function describes the gain profile of the material, and its *full width at half maximum* (FWHM) bandwidth is defined as $|\Delta kL| \cong 2\pi$. The acceptance bandwidths are inversely proportional to the crystal length. This implies that shorter crystal lengths can tolerate large deviations.

References

[1] N. Bloembergen, "Nonlinear optics and spectroscopy," Rev. Mod. Phys. 54, 685-695 (1982).

[2] D. Kleinman, "Theory of optical parametric noise," Phys. Rev., 174, 1027-1041 (1968).

[3] M. Ebrahim-Zadeh and M. Dunn, "Optical parametric oscillators," in *OSA Handbook of Optics*, Vol. 4, (McGraw-Hill New York, 2000). Chap. 22, pp. 1-72.

[4] P. Franken and J. Ward, "Optical harmonics and nonlinear phenomena," Rev. Mod. Phys. 35, 23-29 (1963).

[5] R. Sutherland, "Handbook of nonlinear optics," second edition, Marcel Dekker, Inc., USA (1996).

[6] R. Boyd, "Nonlinear optics," Academic press, San Diego (2007).

[7] D. Kleinman, "Nonlinear dielectric polarization in optical media," Phy. Rev. 126, 1977-1979 (1962).

[8] P. Powers and J. Haus, "Fundamentals of nonlinear optics," CRC Press, USA (2011).

[9] Y. Shen, "The principles of nonlinear optics," John Wiley, New York (1984).

[10] S. Harris, "Tunable optical parametric oscillators," Proc. of IEEE 57, 2096-2113 (1969).

[11] J. Armstrong, N. Bloemberger, J. Ducuing and P. Pershan, "Interactions between light waves in a nonlinear dielectric," Phys. Rev. 127, 1918-1939 (1962).

[12] I. Barry, G. Ross, P. Smith, R. Eason, and G. Cook, "Microstructuring of lithium niobate using differential etch-rate between inverted and non-inverted ferroelectric domains," Mat. Lett. 37, 246-254 (1998).

[13] P. Schunemann, K. Zawilski, L. Pomeranz, D. Creeden, and P. Budni, "Advances in nonlinear optical crystals for mid-infrared coherent sources," J. Opt. Soc. Am. B 33, D36-D43 (2016).

[14] M. Vainio, J. Peltola, S. Persijn, F. Harren, and L. Halonen, "Singly resonant cw OPO with simple wavelength tuning," Opt. Express 16, 11141-11146 (2008).

[15] N. Barnes and V. Corcoran, "Parametric generation processes: spectral bandwidth and acceptance angles," App. Opt. 15, 696-699 (1976).

Chapter 3

Continuous-wave OPO based on fan-out-grating PPKTP

3.1 Background and motivation

Since the first report of a continuous-wave (cw) optical parametric oscillator (OPO) in 1968 [1], with its operation in near-infrared (near-IR) spectral range, the field of cw OPOs has been vastly expanding in different aspects [2]. The availability of stable solid-state visible pump lasers, and the advent of new nonlinear materials, most importantly the advances in quasi-phase-matching (QPM) engineering technology, together with innovative OPO design concepts, have led to high-power, widely tunable mid-IR sources [3]. The cw OPOs, offering broad wavelength tunability in the near and mid-IR region with single-frequency output and good beam quality, are well established in the commercial market as promising robust devices [4]. These sources are of key significance in several applications including frequency metrology, high-resolution spectroscopy, optical microscopy, and near-IR imaging [5–8].

The cw OPOs pumped by green radiation (532 nm) are attractive because of their ability to generate output from the visible to near-IR in a single device. However, given the small parametric gain available under low pump intensities in the cw regime, to exploit the highest nonlinear coefficient of the nonlinear optical crystal, practical cw OPOs are exclusively based on quasi-phase-matched nonlinear materials with long interaction lengths [9]. Moreover, the available nonlinear crystals for green pumping are limited due to absorption of the visible light and the resultant thermal

lensing. The quasi-phase-matched materials that have been explored in the past for high-power cw OPOs include periodically-poled $LiNbO_3$ (PPLN), $LiTaO_3$ (PPLT) and $KTiOPO_4$ (PPKTP), MgO-doped PPLN (MgO:PPLN), and stoichiometric PPLT (MgO:sPPLT) [3].

The green-induced infrared absorption (GRIIRA) and photorefractive damage caused by the visible pump and signal radiation below ∼1 µm precludes the use of PPLN as gain medium for green-pumped OPOs. The development of viable singly-resonant oscillators (SROs) based on PPLN is challenging as GRIIRA leads to significant thermal lensing [10]. Moreover, undoped PPLN crystal needs to be operated at high temperatures >100 °C, especially when pumped by intense visible light, in order to minimize the photorefractive effect. An alternative nonlinear crystal PPLT was used in a pump-enhanced SRO configuration with a frequency-doubled Nd:YAG laser at 532 nm [11]. The thermal effects were observed in such OPO as well and the output powers were limited due to the pump absorption in PPLT. Further, it was demonstrated that GRIIRA and photorefractive susceptibility to the visible light can be eliminated, or at least significantly reduced, when using MgO:PPLN and MgO:sPPLT crystals [12]. This enabled the generation of multi-watt idler powers with wide wavelength tunability, using a green-pumped cw SRO based on MgO:sPPLT [13]. Similarly, a 532 nm-pumped cw SRO based on MgO:PPLN was reported together with its application in Doppler-free saturation spectroscopy of the cesium D_2 line using the output signal at 852.347 nm [14].

Another quasi-phase-matched material that has been explored for the green pumping scheme is PPKTP, which has higher photorefractive damage threshold and negligible GRIIRA compared to both PPLN and PPLT. Therefore, it does not require high temperature operation as in the case of PPLN and PPLT crystals. Various cw OPOs based on PPKTP have been reported in the past. Table 3.1 summarises the performance characteristics of the tunable cw OPOs demonstrated to date using PPKTP as gain medium. The first report of such OPO was based on a doubly-resonant oscillator (DRO)

configuration, pumped at 532 nm by frequency-doubled Nd:YAG laser [15]. A year later, another PPKTP-based cw DRO was demonstrated along with its spectroscopic application by recording the absorption spectrum of methane near 1649 nm [16]. Around the same time, a PPKTP-based cw SRO under intracavity pumping scheme was reported along with additional Ti:sapphire pump wavelength tuning at room temperature [17]. By configuring the same pump laser and SRO in ring-cavity geometries and using an etalon, similar results were reported with single-frequency signal output of linewidth <15 MHz [18]. Later, a cw OPO in a pump-enhanced SRO configuration, with signal as a resonant wave, was demonstrated [19]. In 2002, a cw SRO with broad near-IR wavelength tuning was reported using a pair of multiple-grating PPKTP crystals, where the idler was further frequency-doubled to generate visible radiation from the same system [20]. Much later, in 2011, a DRO was demonstrated with maximum output-coupled signal power of 156 mW at 805 nm [21].

Although the above mentioned sources have exhibited good efficiency and wide tunability, the wavelength tuning in the practical SRO cavity geometry has been achieved by variation of the PPKTP crystal temperature. However, changing the crystal temperature is a slow process, as the crystal needs to reach thermal stability at each defined temperature. Therefore, the wavelength tuning under this approach is not rapid. Moreover, damage in PPKTP has been observed at high temperatures when pumped at high green powers [20], thus limiting the attainable spectral tuning range at high powers when using the crystals with discrete and uniform grating periods. On the other hand, wavelength tuning with the continuous variation of QPM grating period, which can be achieved with fan-out grating crystal design at fixed low temperatures, is a relatively fast process, and can provide widely tunable near-IR output wavelengths [22].

Pump (nm)	Configuration	Signal (nm)	Idler (nm)	Signal power (mW)	Idler power (mW)	QPM grating period (μm)	Crystal temperature (°C)	Ref.
532	DRO	1037-1093		6.5 (signal + idler)		9	32-38	[15]
532	DRO	763.44-769.14	1639.17-1665.67	-	10 (1650 nm)	9.55	20-55	[16]
800	Intracavity SRO	1140-1270	2230-2730	-	455 (2470 nm)	28.5	20 (pump tuning)	[17]
		1180-1260	2290-2570	-	115 (2350 nm)		35-100	
532	Pump-enhanced SRO	865-1032	1100-1384	28 (946.4 nm)	72 (1215 nm)	9	37.5-225	[19]
532	SRO	656-1035	1096-2830	60	800	8.96-12.194	RT-150	[20]
526.5	OC-DRO	791.29-807.53	1512.87-1573.37	156 (805 nm)	89 (1522 nm)	9.68	10-90	[21]

Table 3.1: Continuous-wave tunable OPOs based on PPKTP.

The advancement in quasi-phase-matched crystal fabrication techniques has now made fan-out grating design in PPKTP crystal possible. Given the advantages of such grating pattern, particularly in providing rapid and continuous wavelength tuning, it is desirable to exploit the fan-out grating design in PPKTP to study its potential as a nonlinear material for stable frequency-conversion devices. As such, it would be important to develop cw OPO sources based on this material, providing wide and rapidly tunable output wavelengths, while circumventing the need for temperature tuning. Here we report, for the first time to the best of our knowledge, a green-pumped cw OPO based on a fan-out grating design in PPKTP, enabling rapid and continuous wavelength tuning with lateral translation of the nonlinear crystal, operating at the room temperature. At first, we completely characterized the system in a bow-tie SRO geometry with all highly reflective cavity mirrors for the signal, and further we investigated the performance of the OPO by optimally output coupling the intracavity signal. This is also the first report of output coupling the signal from a PPKTP-based cw SRO, in order to effectively reduce thermal loading in the crystal and enhance output efficiencies with watt-level idler power.

3.2 Experimental setup

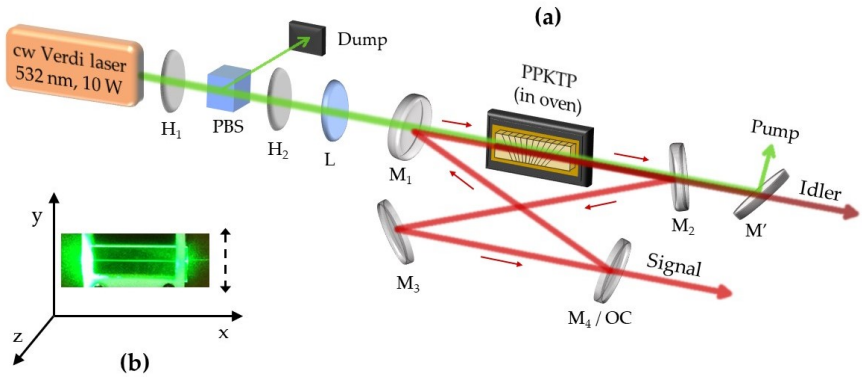

Figure 3.1: (a) Schematic of the experimental setup. H_{1-2}, half-wave plates; PBS, polarizing beam splitter; L, lens; M_{1-4} and M', mirrors; OC, output coupler. (b) Laboratory picture of the crystal.

A schematic of the experimental setup and a laboratory photo of the crystal is shown in Figure 3.1. A commercial cw frequency-doubled Nd:YVO_4 solid-state laser is used as a pump source for the OPO, which delivers up to 10 W of output power at 532 nm in a single-frequency, linearly polarized beam with M^2<1.1. The laser is operated at maximum power in order to maintain stable characteristics, and the input pump power for OPO is adjusted using a combination of half-wave plate, H_1, and polarizing beam-splitter (PBS) cube. A second half-wave plate, H_2, is placed to control the pump polarization for phase-matching in the crystal. The pump beam is focused at the centre of the crystal to the beam waist radius of w_{0p}~49 µm. The PPKTP crystal used has dimensions of 30x11x1 mm^3, in a fan-out grating design with periods varying over Λ=9.00-10.85 µm across its lateral dimension. The crystal is housed in an oven with a stability of ±0.1 ^oC, adjustable from room temperature to 200 ^oC, and mounted on a linear translation stage (resolution of 10 µm) to enable smooth grating tuning across its width in ±y direction with fine and continuous translation of the

crystal. The end faces of the crystal are antireflection (AR)-coated at 532 nm (R<0.5%), 720-990 nm (R<0.5%), and 1130-2040 nm (R<5%). The OPO is configured in a compact ring cavity comprising two concave mirrors, $M_{1,2}$ (r=-100 mm), and two plane mirrors, $M_{3,4}$. Cavity mirrors, M_{1-4}, are highly reflecting (R>99.8%) for the signal (620-1030 nm) and highly transmitting (T>97%) for the idler (1078-3550 nm) and pump, ensuring singly-resonant oscillation of the signal with single-pass pumping. In the latter part of the experiment, the highly reflective mirror, M_4, is replaced by a plane output coupler, OC. It has an output coupling of ∼1% across 635-1100 nm. A dichroic mirror, $M^{'}$, is used to separate the output idler from the transmitted pump.

3.3 Results

3.3.1 Crystal characterization

Given the first demonstration of PPKTP in the fan-out grating design, and in particular a system pumped at the high green powers, it was important to characterize the crystal before implementing the OPO. Hence, transmission of the crystal was measured as a function of pump intensity at various temperatures, under phase-matched polarization and orthogonal non-phase-matched polarization, while keeping the crystal at a fixed position. The results are shown in Figure 3.2.

Transmission of ∼89.6%, ∼89.6% and ∼87% under phase-matched polarization, and ∼93.2%, ∼93.2% and ∼91.7% under orthogonal non-phase-matched polarization was observed at room temperature (T∼25 ^{o}C), moderate temperature (T∼50 ^{o}C), and high temperature (T∼170 ^{o}C), respectively. As evident from Figure 3.2 (a), the variation in crystal transmission with pump intensity at all temperatures remains negligible. No drop in transmission was observed at high intensities, thus indicating an absence of two-photon absorption. However, at high temperature, a small drop in

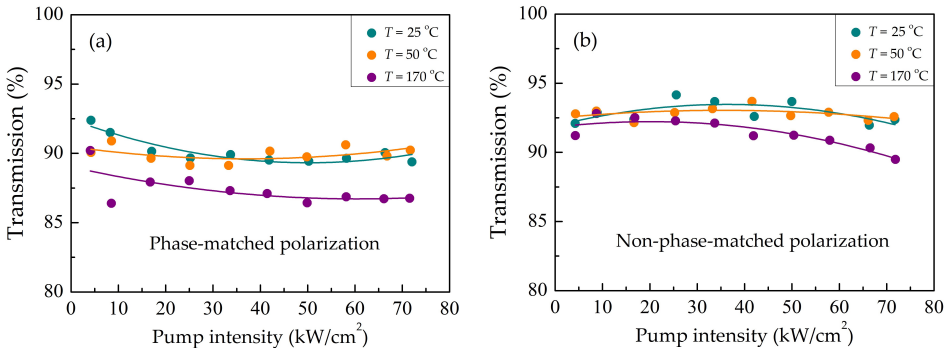

Figure 3.2: Transmission of PPKTP sample as a function of pump intensity at different crystal temperatures under (a) phase-matched, and (b) orthogonal non-phase-matched polarization.

transmission by ∼2.5% was observed at all pump intensities as compared to low temperatures. The behaviour of the crystal under orthogonal non-phase-matched polarization across the pump intensity was similar, as seen in Figure 3.2 (b). However, the transmission at all temperatures was measured to be ∼4% higher as compared to that of the phase-matched polarization. The lower transmission under phase-matched polarization (z-axis for periodically-poled sample) as compared to orthogonal non-phase-matched polarization has been reported earlier in KTP [23].

3.3.2 SRO configuration

The OPO was initially characterized by extracting the single-pass idler from the cavity along with the residual resonating signal radiation leaking through the mirror, M_4. The results obtained under such configuration are discussed in this section. The wavelength tuning in the present device could be achieved through lateral translation of the PPKTP crystal to vary the grating period, or by variation of the temperature of the crystal, while keeping either of the parameters fixed. Initially, the position of the crystal was varied while keeping the crystal at low temperature of 22.4 ^{o}C, and

the signal wavelengths were recorded using a spectrometer (Ocean Optics HR4000) at optimum pump powers generating maximum output powers. Figure 3.3 shows the generated signal and idler wavelengths as a function of variation of the crystal position at 22.4 °C. The rapid and continuously tunable output was obtained across 863-742 nm in signal, with the corresponding idler wavelengths over 1386-1879 nm. As seen from Figure 3.3, at 22.4 °C, 1.45 mm is the minimum and 8.08 mm is the maximum crystal position used for tuning. The complete width of the crystal could not be used, since the pump beam distortion was observed towards the edges of the crystal, which ceased the OPO operation.

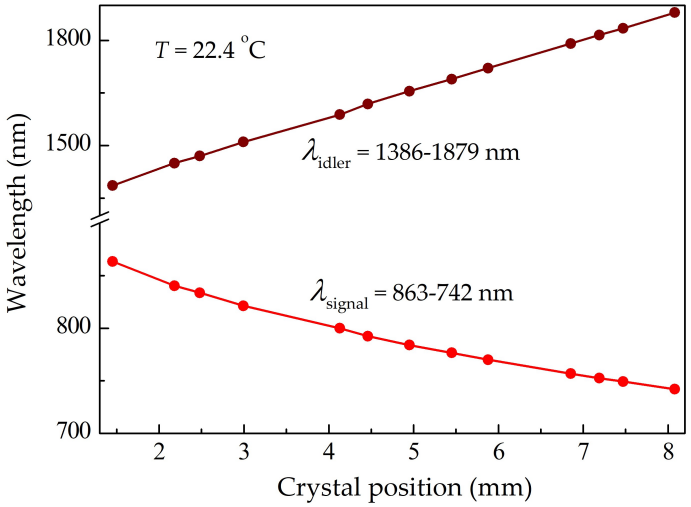

Figure 3.3: Wavelength tuning with lateral translation of PPKTP crystal at temperature T=22.4 °C.

Later, the wavelength tuning was performed by varying the temperature of the crystal when the crystal was kept fixed at position 1.45 mm. The results are shown in Figure 3.4, where the signal tuning across 863-825 nm and idler tuning across 1385-1498 nm was recorded with the corresponding crystal temperature variation across 23.4-165 °C.

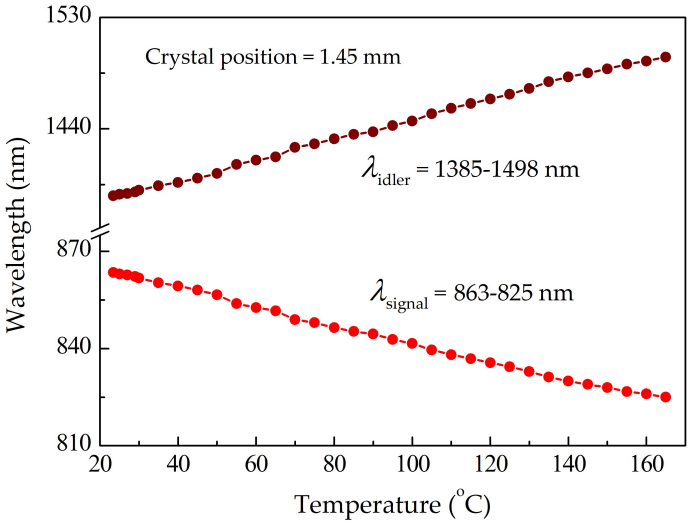

Figure 3.4: Wavelength tuning as a function of crystal temperature, at crystal position 1.45 mm.

Given the fan-out grating design of the PPKTP sample, calculation of the grating periods relied on the experimental wavelength tuning data and the available Sellmeier equations for PPKTP. The properties of PPKTP crystal including thermo-optic dispersion relations and the Sellmeier equations have been extensively studied in many earlier reports [24–28]. In order to determine the grating period at the corresponding crystal position, the grating period variation across the width of the crystal was theoretically calculated, using the relevant Sellmeier equations, as shown in Figure 3.5 (a). At the generated spectral range with the crystal under room temperature operation, the simulations were performed using three Sellmeier equations [24, 26, 27]. As evident, the theoretically calculated grating period at a fixed crystal position varies with different Sellmeier equations. Thus, signal tuning across 863-742 nm, as shown in Figure 3.3, was achieved for calculated grating period variation across Λ=9.13-10.37 µm, Λ=9.10-10.46 µm, and Λ=9.17-10.55 µm, as plotted in Figure 3.5 (a), obtained from [24], [26],

and [27], respectively.

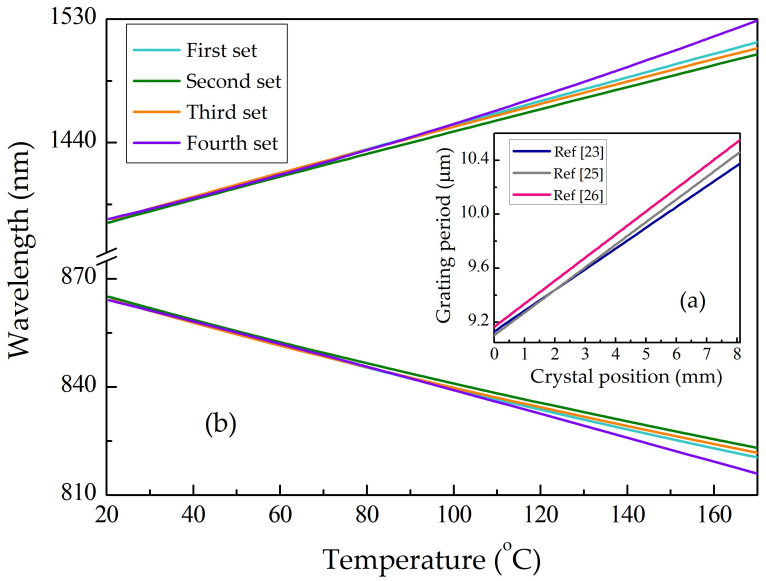

Figure 3.5: Inset: (a) Calculated grating period corresponding to the crystal position, (b) Theoretical temperature tuning curves obtained from the calculated grating periods.

At the fixed crystal position of 1.45 mm, the temperature tuning curves were also simulated using four different sets of Sellmeier equations and temperature derivatives of refractive indices, as shown in Figure 3.5 (b). The first and second set include the refractive index temperature derivatives from [25], and Sellmeier equations from [24] and [26], respectively, while the third set includes the refractive index temperature derivatives and Sellmeier equations from [27], and fourth set includes the refractive index temperature derivatives from [28] and Sellmeier equations from [26]. Further, the theoretical curves from Figure 3.5 (b) were compared with the experimental temperature tuning data from Figure 3.4. It was observed that, the third set of theoretical curves is in good agreement with the recorded experimental results. Therefore, the Sellmeier equations from [27] were

used hereafter, to calculate the grating periods at the given crystal position using data from Figure 3.5 (a).

Temperature tuning was recorded also at the longest accessible crystal position of 8.08 mm (Λ=10.55 µm), as seen in Figure 3.6. The shortest signal wavelength of 738 nm, with the corresponding longest idler 1910 nm, was generated at this position. However, as evident from Figures 3.4 and 3.6, in this case, variation in wavelength with temperature is relatively small. At longer grating periods, essentially further away from the degeneracy, temperature tuning range of output wavelengths decreases, as the maximum limit of crystal temperature for optimal OPO operation decreases due to the dispersion properties of PPKTP, similar to MgO:sPPLT [22].

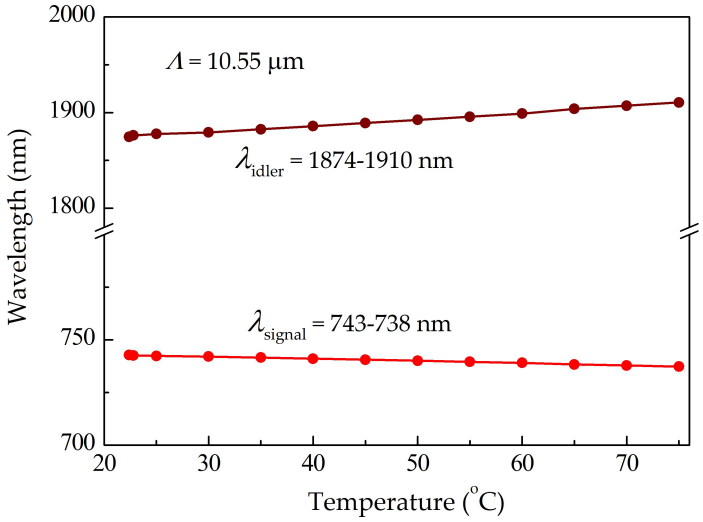

Figure 3.6: Variation in wavelength across temperature tuning at Λ=10.55 µm.

Further, the output wavelengths were extended to another extreme by translating the crystal and keeping its temperature fixed at 50 °C. As seen from Figure 3.7, the longest signal and the corresponding shortest idler wavelengths were recorded to be 908 nm and 1284 nm, respectively. Thanks to the thermo-optic dispersion properties of PPKTP, even shorter

grating period of Λ=9.19 µm was accessible at higher temperature, as seen in this case. As evident from the results, fan-out grating tuning at a fixed crystal temperature has been found to be an efficient and robust approach to achieve wide wavelength tunability.

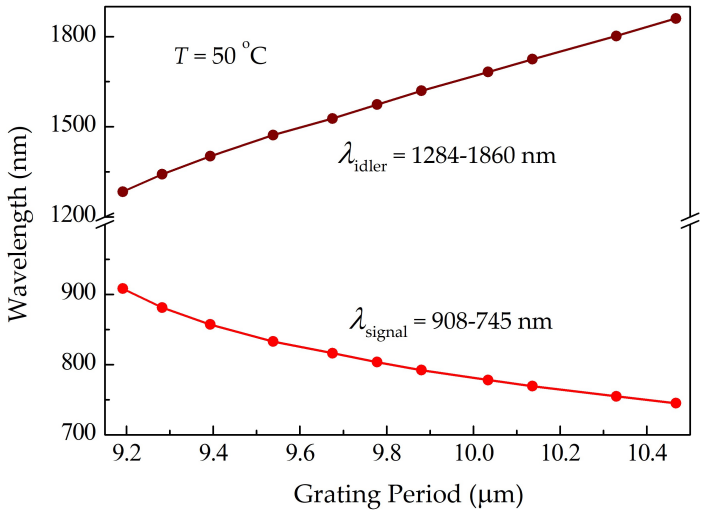

Figure 3.7: Variation in wavelength with grating period tuning at crystal temperature T=50 °C.

The generated idler powers across the respective wavelength tuning bandwidths were recorded together with both sets of grating tuning data. Figure 3.8 shows the output power measured across the idler tuning range (1386-1879 nm) at the crystal temperature of 22.4 °C, obtained from the continuous grating tuning. As seen, the maximum idler power of 210 mW was recorded at 1588 nm, with >80 mW over 62% of the measured idler wavelength tuning range. This set of measurements was performed at 5.2 W of pump power, corresponding to an idler extraction efficiency of 4% at 1588 nm. At the higher crystal temperature of 50 °C, an idler power >200 mW was measured over 48% of the wavelength tuning range, with the maximum idler power of 365 mW at 1284 nm, as shown in Figure 3.9.

The drop in output power at the longer idler wavelengths, as seen in the Figures 3.8 and 3.9, is attributed to the reduction in parametric gain away from the degeneracy at longer grating periods.

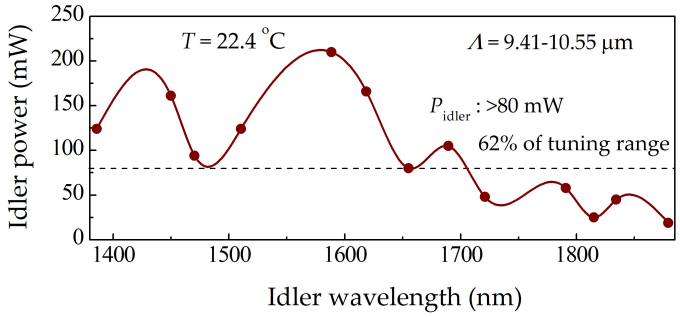

Figure 3.8: Idler power across the grating period tuning range at T=22.4 °C.

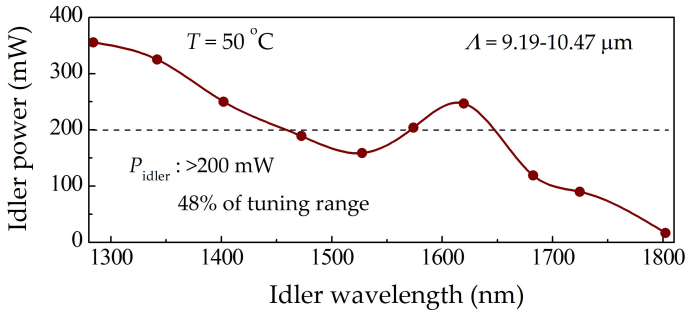

Figure 3.9: Idler power across the grating period tuning range at T=50 °C.

The output powers across the idler wavelength tuning bandwidths were also recorded during temperature tuning, at shorter and longer grating periods of Λ=9.41 µm, and Λ=10.55 µm, as shown in Figures 3.10 and 3.11, respectively. At the shorter grating period, the maximum idler power of 247 mW was recorded at 1436 nm with >100 mW over 90% of the wavelength tuning range. On the other hand, an output power of >40 mW over 23% of the idler wavelength tuning range was obtained at the longer grating period, with the maximum power of 85 mW at 1878 nm. As seen in the Figure 3.10,

the drop in output power was observed also at the shorter idler wavelengths, as the crystal temperature was increased, due to the degradation of the pump beam quality at higher crystal temperatures. However, a relatively low idler power was measured, as seen in the Figure 3.11, because the output conversion efficiency was hampered due to the combination of low gain at the longer grating period and distorted pump beam at the higher crystal temperatures.

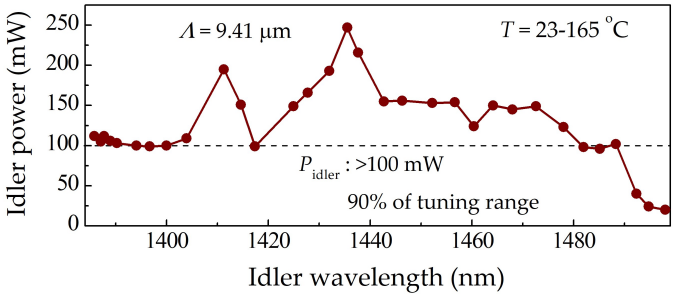

Figure 3.10: Idler power across the temperature tuning range at Λ=9.41 μm.

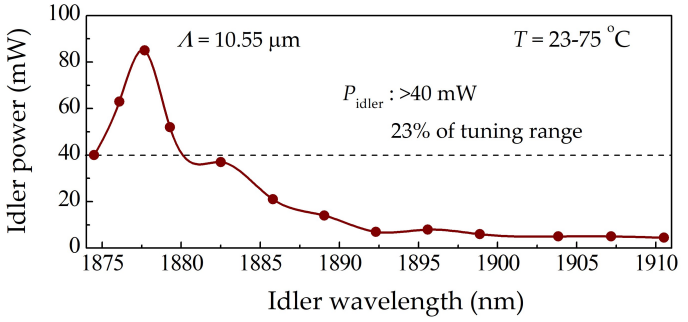

Figure 3.11: Idler power across the temperature tuning range at Λ=10.55 μm.

To investigate the power scaling capability of the system, variation in the idler power with pump power was recorded, as shown in Figure 3.12. The power scaling measurement was performed with the crystal kept at 50 ^{o}C and at a grating period Λ=9.29 μm. As seen, the idler power increases

linearly with the pump power, however, with small sharp transitions, generating the maximum idler power of 558 mW for the pump power of 3.92 W. The threshold pump power for the SRO was recorded to be 2.66 W.

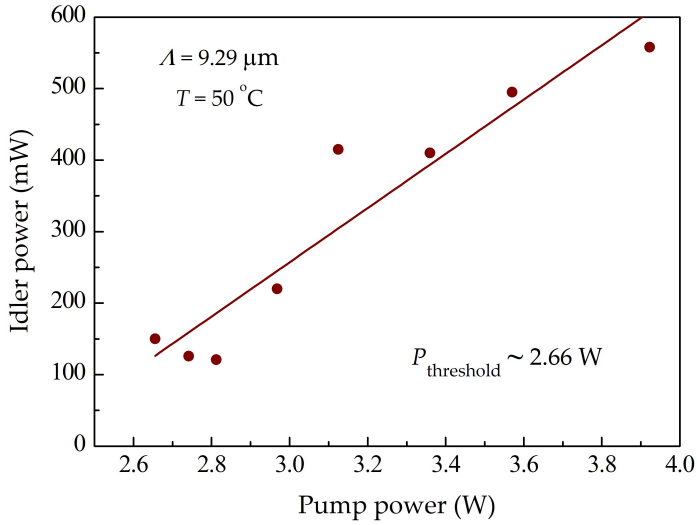

Figure 3.12: Output idler power as a function of input pump power.

In addition, the power stability of the idler output at 1461 nm was recorded, under free-running conditions. During these measurements, the crystal was kept at the room temperature and under the incident pump power of 3.1 W. As seen in Figure 3.13, the idler power exhibits a passive stability better than 2.6% rms over 1.6 minutes. The observed fluctuations in the idler power are attributed to the mechanical vibrations and, in a large part, to temperature fluctuations in the crystal. In order to find the role of air currents on the power fluctuations, the OPO was enclosed inside a box, and the idler power stability measurement was performed again. Similar results were found with the enclosed system, which suggests negligible contribution of the laboratory air currents to the output power fluctuations.

As the broadest wavelength tuning was achieved over the grating period variation across Λ=9.19-10.47 μm with the crystal temperature fixed

at 50 ^{o}C, its corresponding signal spectra with the stable output powers were plotted across the signal tuning range of 908-745 nm. The results are shown in Figure 3.14.

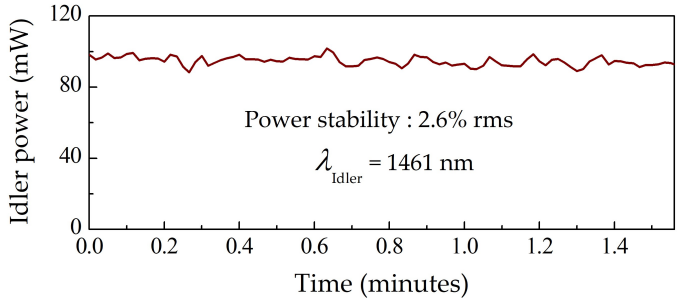

Figure 3.13: Passive power stability of the idler over 1.6 minutes.

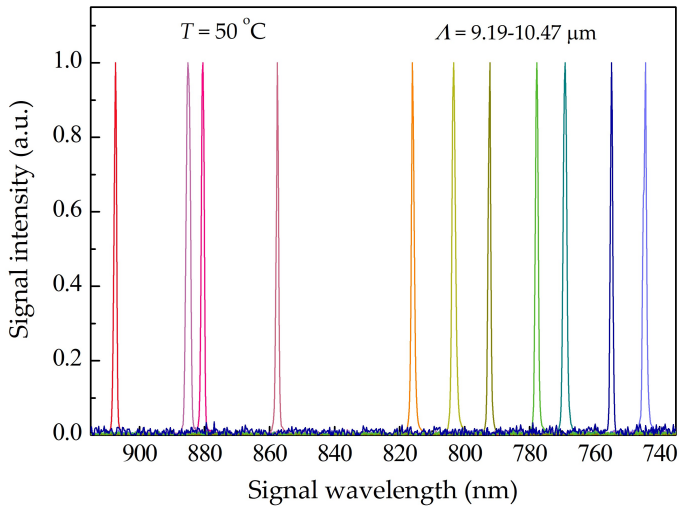

Figure 3.14: Signal spectra corresponding to the tuning range of Figure 3.7.

Moreover, far-field energy distribution along with orthogonal intensity profile of the signal beam was also recorded. The measurements were performed at the wavelength 838 nm with the maximum output signal power. As seen in Figure 3.15, a Gaussian profile exhibiting circularity >93%

was recorded, confirming high spatial beam quality. Similar beam profiles were observed across the entire signal tuning range.

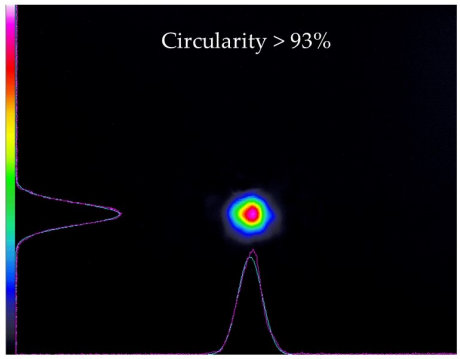

Figure 3.15: Far-field energy distribution of the output signal beam.

3.3.3 OC-SRO configuration

Due to the major limitation of low gain and high pump power threshold, the general approach to the development of cw SROs has been to deploy an optical cavity with the lowest loss at the resonant signal wave to minimize the threshold, while providing the maximum output power in the non-resonant idler in order to achieve the highest power extraction at the longer wavelengths. However, optimum output coupling of the intracavity signal can enable efficient management of thermal effects, which result from the high pump powers required for cw SRO operation. Output-coupled singly-resonant oscillator (OC-SRO) enhances the overall performance of the OPO with regard to the total output power, extraction efficiency, and useful tuning range that can be brought about at a small cost of marginally increased threshold. To study and compare the performance of the existing device under such configuration, the highly reflective mirror, M_4, was replaced by a plane output coupler, OC. The results obtained under the OC-SRO configuration are discussed in this section.

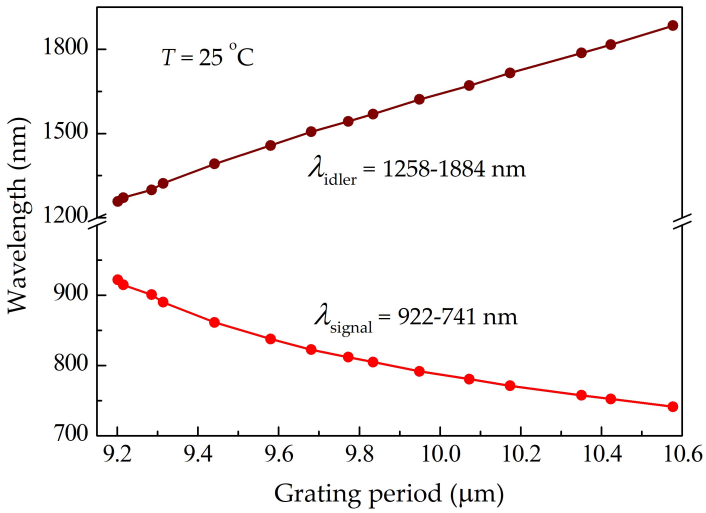

Figure 3.16: Variation in wavelength across grating period tuning at crystal temperature T=25 °C.

Different tuning schemes were employed under this configuration also, as shown earlier for the case of pure SRO. Initially, the generated signal and the corresponding idler wavelengths were recorded as a function of grating period variation, while the crystal temperature was fixed at 25 °C. Figure 3.16 shows the rapid and continuously tunable output across 922-741 nm in signal and 1258-1884 nm in idler. As seen, the grating tuning wavelength coverage, for the OC-SRO configuration under room temperature operation, shows an increase of 60 nm in signal and 133 nm in idler, as compared to that for the SRO configuration under similar conditions. The extracted signal and output idler powers were also measured across these tuning ranges. The results are shown in Figure 3.17. The signal power of >150 mW over the entire signal tuning range was generated with up to 450 mW at 901 nm, whereas an idler power of >400 mW was recorded over 66% of the idler wavelength tuning range with the maximum power up to 1.2 W at 1299 nm, corresponding to the total extraction efficiency of 30% for 5.5 W

of pump power. As evident, in this case, the idler power shows a significant increment of ∼1 W, together with the practical signal power extraction, as compared to the SRO configuration.

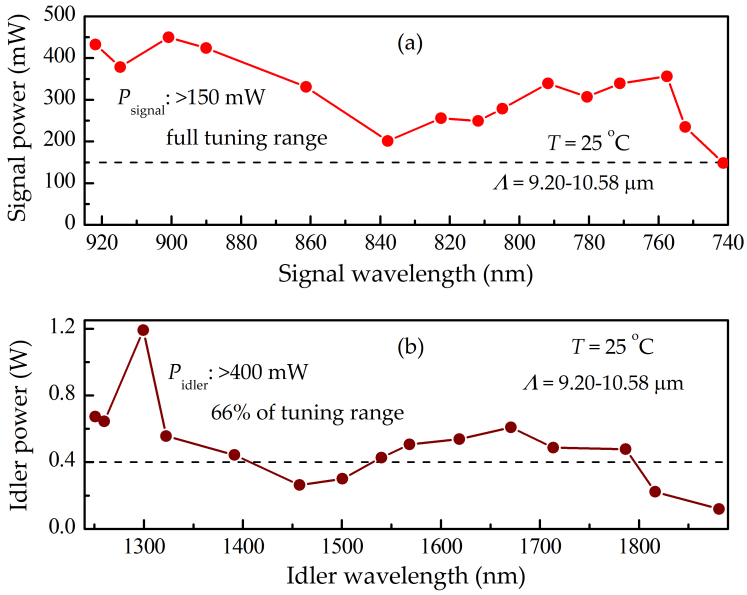

Figure 3.17: (a) Signal, and (b) idler power across grating period tuning range at T=25 °C.

Later, the wavelength tuning was obtained by varying the crystal temperature and keeping the crystal fixed at the position of shorter grating period of Λ=9.28 μm. The signal tuning across 901-865 nm and idler tuning across 1299-1381 nm was measured with the corresponding crystal temperature variation across 23-112 °C. The results are shown in Figure 3.18. The maximum generated powers were also recorded across this tuning range, as shown in Figure 3.19. The signal and idler powers of >200 mW over 72% of the respective tuning bandwidths were obtained. The signal and the corresponding idler wavelengths were further extended to 739 nm and 1901 nm, respectively, with temperature tuning at the fixed crystal position of

longer grating period of Λ=10.58 µm, as seen in Figure 3.20. The maximum extracted powers were also measured across this tuning range, as shown in Figure 3.21. The signal and idler powers of >40 mW over 88% and 86% of the respective tuning ranges were measured, at the longer grating period. As discussed in the previous section, the temperature-tuned wavelength coverage and the corresponding recorded powers were affected, due to the several factors, such as the dispersion properties of PPKTP, the reduction in parametric gain away from the degeneracy, and the degradation in the pump beam quality at higher crystal temperatures. Apart from this, in the OC-SRO case, at both extremes of crystal position, a reduced wavelength tuning performance was observed across the temperature tuning variation, since the recorded maximum operating crystal temperatures for OC-SRO were lower, as compared to that for the SRO configuration. However, the output powers across the temperature tuning bandwidths, at both extreme crystal positions in OC-SRO, show improvement over the SRO output powers under similar conditions.

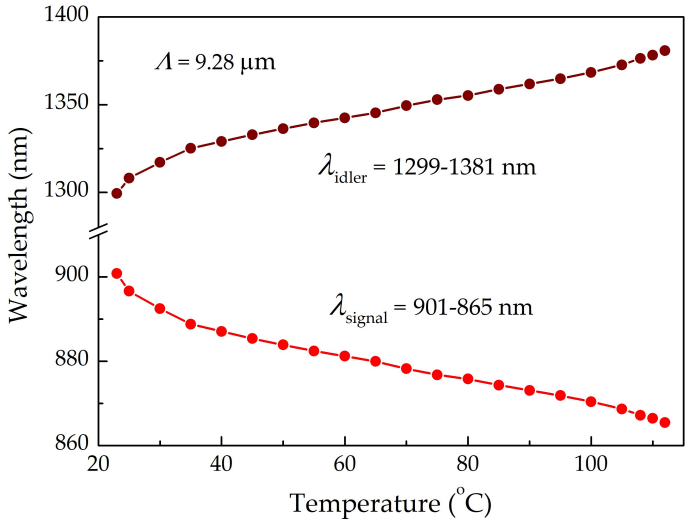

Figure 3.18: Variation in wavelength across temperature tuning at Λ=9.28 µm.

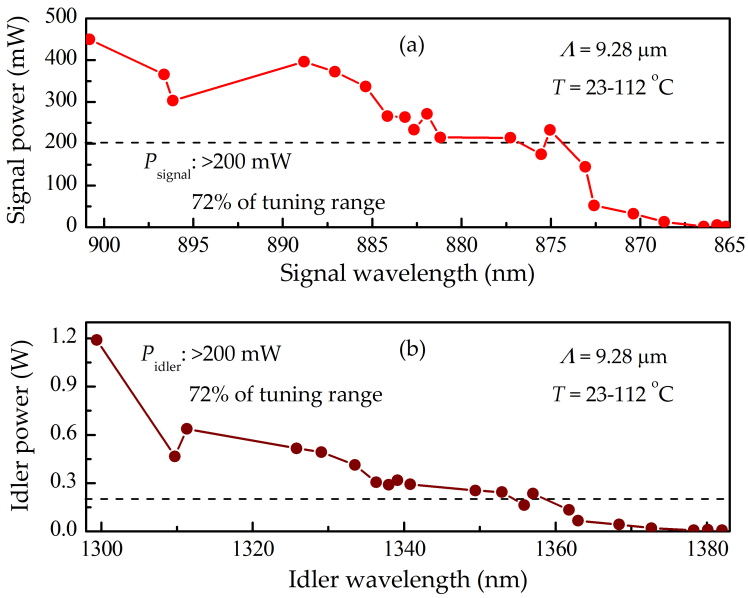

Figure 3.19: Output power across the temperature tuning range at Λ=9.28 μm.

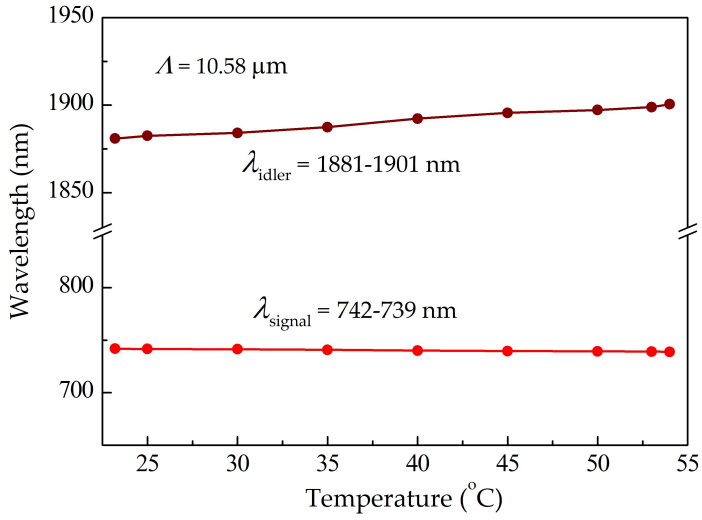

Figure 3.20: Variation in wavelength across temperature tuning at Λ=10.58 μm.

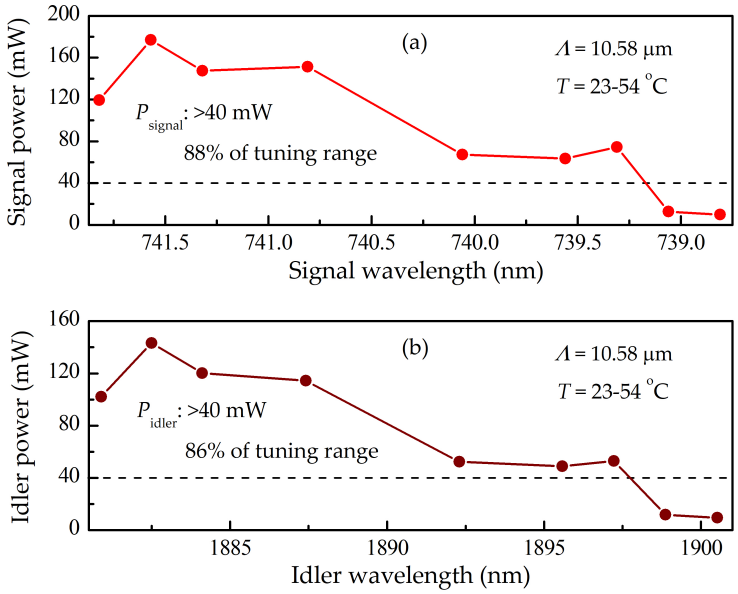

Figure 3.21: (a) Signal, and (b) idler power across the temperature tuning range at Λ=10.58 µm.

As in the case of pure SRO, the power scaling of the OPO was studied also in the OC-SRO configuration. Variation in the signal and the corresponding idler power as a function of pump power was measured, as shown in Figure 3.22 (a). The power scaling measurements were performed with the crystal at 25 °C for Λ=9.21 µm. As seen, the output powers increase with the pump power, exhibiting abrupt transitions in the signal and idler powers. The maximum signal power of 367 mW for pump power of 4.5 W and the maximum idler power of 640 mW for pump power of 4.1 W was generated during the power scaling. The threshold pump power under OC-SRO configuration was recorded to be 3.6 W, representing an increase of only 35% over the SRO threshold. The output coupling of the signal enabled the use of slightly higher pump powers under this configuration as compared to the SRO, by reducing thermal loading in the crystal. In

both configurations, the output powers recorded are the maximum powers observed at the corresponding pump power, with the cavity length kept unchanged throughout the power scaling measurements. Hence, the sharp transitions in output powers can be attributed to the temperature fluctuations in the crystal at a given pump power, resulting in mode-hopping. However, for pump powers beyond 5 W, distortion in the output beam profile was observed under long-term operation. Therefore, to avoid thermal loading in PPKTP, the maximum pump power was limited to 4.5 W. The sudden transitions in the signal wavelength with pump power were also observed, as seen in Figure 3.22 (b). With an increase in pump power from 3.6 W to 4.5 W, the signal wavelength was observed to decrease from 921 nm to 917 nm. This drop in the signal wavelength can be attributed to the increase in the crystal temperature with the increasing pump power due to residual absorption of $\sim$10% at 532 nm. Using the relevant Sellmeier and thermo-optic dispersion relations [27], the rise of 7.6 ^{o}C in the crystal temperature was theoretically calculated for the recorded drop of $\sim$4 nm in the signal wavelength.

Further, in order to study the performance of the system with respect to the operational time of the OPO, variation in signal and idler powers with the corresponding variation in the pump power was recorded, while keeping the crystal under continuous exposure to the pump, as shown in Figure 3.23(a). When the pump power was kept constant for initial 5 seconds at 5.35 W, the signal and idler powers were observed to decrease with time, from 449 mW to 388 mW, and 1.2 W to 702 mW, respectively. This decrease in the output powers at the constant high pump power may be due to the thermal lensing at pump powers beyond 5 W. As seen, the generation of maximum output power was observed after some seconds of sudden exposure to the pump power of 5.35 W. This abrupt behaviour can also be attributed to possible thermal lensing effects. After 5 seconds, with the decrease in pump power, the output powers start decreasing to 193 mW for signal and 386 mW for idler, at 4.6 W of pump power. With the

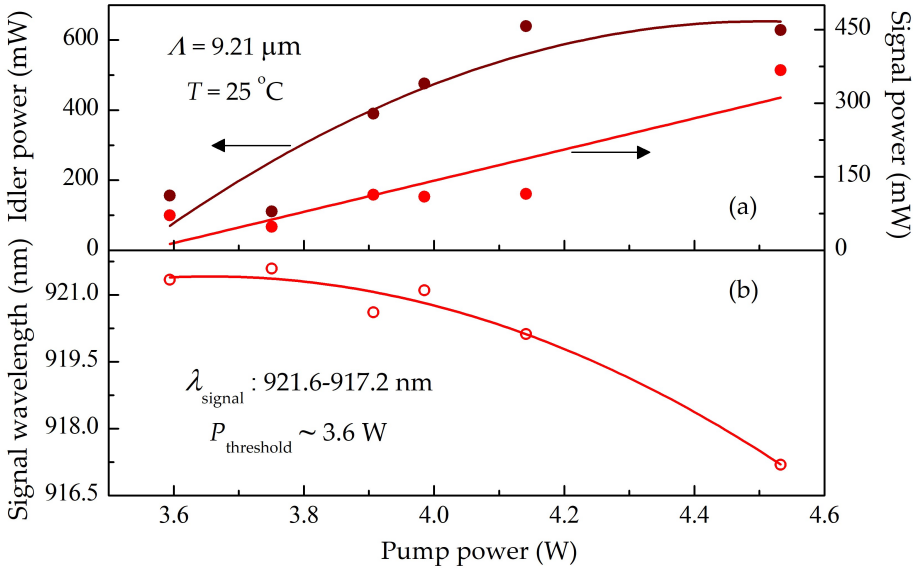

Figure 3.22: (a) Signal and idler powers as a function of pump power, and (b) corresponding variation in signal wavelength with pump power.

further decrease in the pump power, thermal loading in the crystal becomes negligible and the output powers increase to 330 mW for signal and 537 mW for idler, at 4.4 W of pump power. Then, the signal and idler powers are observed to decrease gradually to 273 mW and 471 mW, respectively, with the further decrease in the pump power from 4.4 W to 4 W, beyond which the output power curves show similar behaviour as that of the pump power, at low pump powers. Also shown in Figure 3.23(b) is the simultaneously recorded variation in signal wavelength under the continuous exposure of the crystal to the pump in time. As seen, the signal wavelength decreases over 5 nm when the pump is kept constant at the high power of 5.35 W for the initial 5 seconds. This decrease in the wavelength at the constant high power was due to the heating of the crystal, which resulted in a change in the phase-matching temperature. The decrease in the signal wavelength continued even when the pump power was gradually reduced to 4.6 W

over next 10.8 seconds. With the further decrease in the pump power below 4.6 W, the signal wavelength was observed to start increasing, which is attributed to the lowering of the crystal temperature at the reduced pump power levels. Also, similar behaviour was observed when the crystal was kept at the oven temperature of 50 ^{o}C.

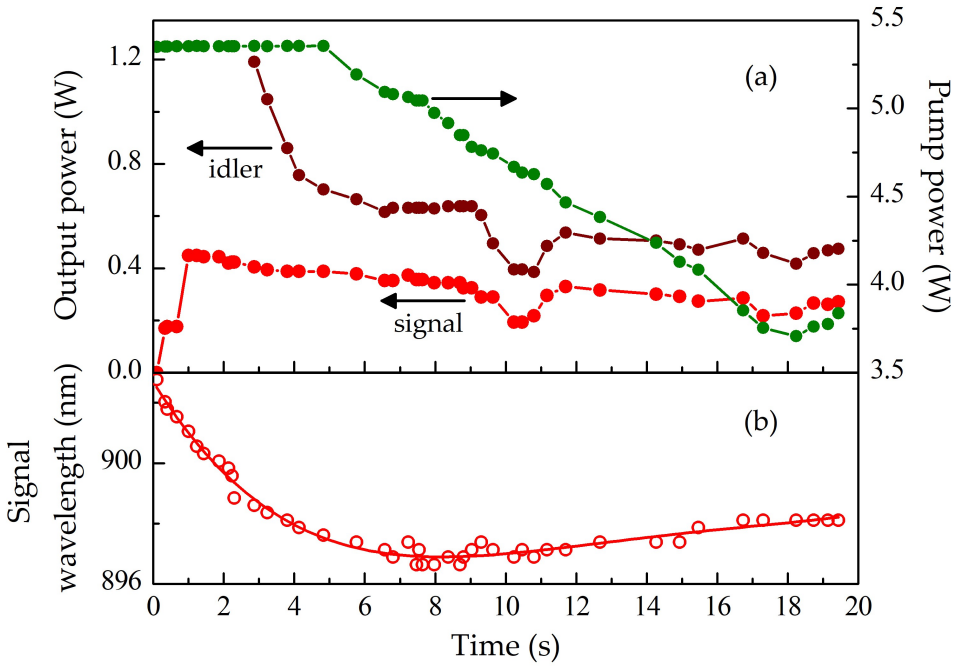

Figure 3.23: (a) Variation in output powers with time, and (b) corresponding variation in signal wavelength with time under exposure to the varying pump power over initial 20 s.

The power stability of the extracted signal at 820 nm, and the corresponding idler output at 1517 nm, was recorded simultaneously, under the free-running conditions, after letting the OPO run for a few minutes. During these measurements, the crystal was kept at room temperature and under the highest input pump power of 5.43 W. The results are shown in Figure 3.24. As seen, the signal and idler powers exhibit passive stability

better than 5.5% rms and 3.2% rms, respectively, over 2.6 minutes. The observed fluctuation in the output powers can be attributed to mechanical vibrations and temperature fluctuations in the crystal, as mentioned in the previous section.

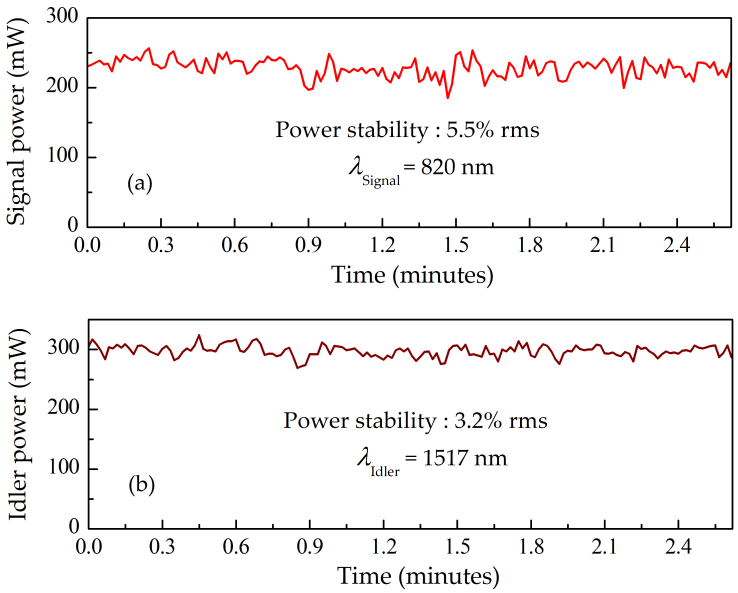

Figure 3.24: Passive power stability of (a) signal, and (b) idler over 2.6 minutes.

Moreover, spectral characterization of the generated signal was performed using a confocal Fabry-Perot interferometer (FSR=1 GHz, finesse=400). The instantaneous linewidth of the signal was measured to be 7.5 MHz, confirming single-frequency operation at room temperature. The recorded signal transmission spectrum at 831 nm is shown in Figure 3.25. Similar behaviour was observed across the entire signal tuning range.

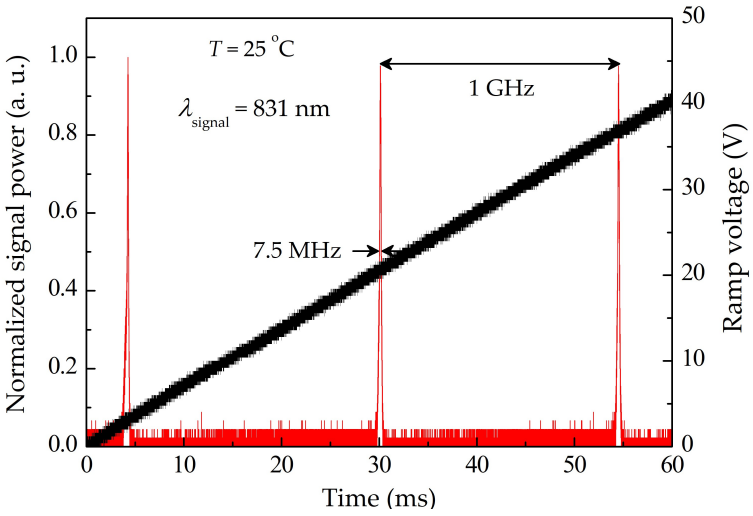

Figure 3.25: Single-frequency spectrum of the extracted signal.

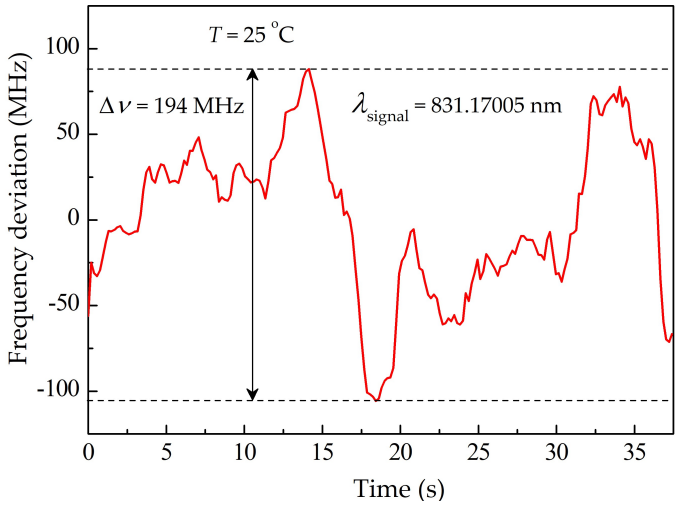

Figure 3.26: Frequency stability of the extracted signal over 38 seconds.

The frequency stability of the output signal was also recorded using a wavemeter (HighFinesse, WS-U 30). The measurements were performed un-

der the free-running conditions, and in the absence of any thermal isolation. The results are shown in Figure 3.26. As seen, the signal exhibits peak-to-peak frequency deviation of $\Delta\nu$ ~194 MHz over 37 seconds, measured at the central wavelength of 831.17005 nm.

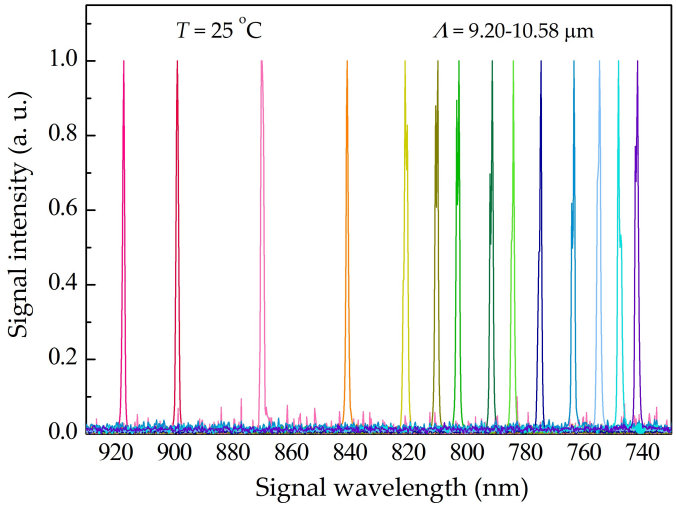

Figure 3.27: Extracted signal spectra corresponding to tuning range of Figure 3.16.

The signal spectra corresponding to the broadest wavelength tuning range was recorded also in the OC-SRO configuration. In this case, it was obtained over the grating period variation across Λ=9.20-10.58 μm, with the crystal kept at 25 °C. As shown in Figure 3.27, signal spectra with the stable output powers were obtained across the signal tuning range of 922-741 nm.

Finally, the far-field energy distribution along with the orthogonal intensity profile of the signal beam was recorded. The measurements were performed at the wavelength of 831 nm with the maximum extracted signal power. As seen in Figure 3.28, a TEM_{00} mode profile exhibiting circularity >95% was recorded, confirming the high spatial beam quality. Similar beam profiles were observed across the entire signal tuning range.

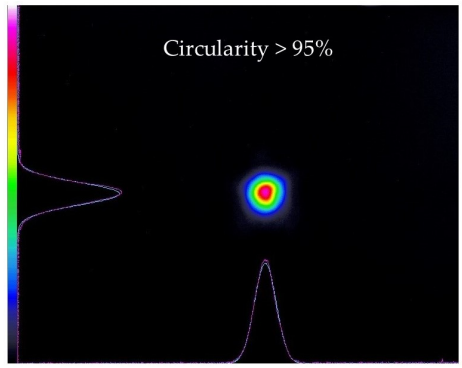

Figure 3.28: Far-field energy distribution of signal beam extracted from OC-SRO.

3.4 Conclusion

In this chapter, we have reported the first realisation of a cw OPO based on the fan-out grating PPKTP crystal. In the fan-out design, the QPM grating periods can be varied smoothly as the nonlinear crystal is translated laterally through the pump beam. This approach results in wide wavelength coverage with fast tuning rates at the fixed crystal temperature, wherein the tuning is limited only by the translational speed and the resolution of the translation mount used for the crystal. We have also employed the conventional temperature tuning method, in order to understand the device performance under different conditions.

Under the pure SRO configuration for the signal wave, the demonstrated OPO has the maximum wavelength coverage across 745-908 nm in signal and 1284-1860 nm in idler, at the constant crystal temperature of 50 ^{o}C. The maximum idler power extracted from the SRO is 356 mW at 1284 nm, with >200 mW over 48% of the idler wavelength tuning range. The pump power threshold for the SRO is 2.66 W. The idler power exhibits the passive stability better than 2.6% rms at 1461 nm, over 1.6 minutes. The output signal beam has circularity >93% at 838 nm, and shows similar results across the entire signal tuning range.

Further, the intracavity signal wave is out-coupled, in order to reduce thermal loading in the PPKTP crystal. The pump power threshold for the OC-SRO is 3.6 W, representing an increase of only 35% over the pure SRO threshold. The wavelength tuning range is greater in the OC-SRO configuration, providing the maximum coverage across 741-922 nm in signal and 1258-1884 nm in idler, at the fixed crystal temperature of 25 ^{o}C. The maximum extracted total power is 1.65 W with >150 mW of signal power over the entire signal wavelength tuning range and >400 mW of idler power over 66% of the idler wavelength tuning range. By output-coupling the signal beam OPO extraction efficiency was increased by 26%, compared to the pure SRO operation at room temperature. This set of measurement was performed at 5.2 W of pump power, corresponding to an idler extraction efficiency of 4% at 1588 nm.

The signal and idler powers exhibit passive stability better than 5.5% rms and 3.2% rms, respectively, over 2.6 minutes. The signal beam shows instantaneous linewidth of 7.5 MHz at 831 nm, confirming the single-frequency operation of the OPO. The signal exhibits peak-to-peak frequency deviation of $\Delta\nu$ ~194 MHz over 37 seconds. The extracted signal from the OC-SRO has a slightly better spatial beam quality. We have also studied the performance of the OC-SRO system with respect to the operational time of the OPO.

In conclusion, together with the wide and rapid wavelength tuning OPO operation at room temperature, we have also demonstrated that by deploying finite output coupling for the resonant signal wave in the SRO, it is possible to improve the overall output power, extraction efficiency, useful tuning range and spectral purity with a little sacrifice to the OPO threshold. The superior performance of the OPO under OC-SRO configuration compared to the pure SRO scheme suggests optimum output coupling of the intracavity power. The reduced wavelength coverage and lower output power under SRO configuration can be attributed to the higher intracavity signal power resulting in additional thermal loading of the PPKTP crystal

at lower critical pump powers beyond 3 W. With improvements in the transmission loss of the PPKTP (currently $\sim$10% at 532 nm), and proper thermal management and crystal temperature control, the performance of the OPO in providing high and stable output powers can be further enhanced.

References

[1] R. Smith, J. Geusic, H. Levinstein, J. Rubin, S. Singh, and L. Van Uitert, "Continuous optical parametric oscillation in $Ba_2NaNb_5O_{15}$," Appl. Phys. Lett. 12, 308-310 (1968).

[2] M. Dunn and M. Ebrahimzadeh, "Parametric generation of tunable light from continuous-wave to femtosecond pulses," Science 286, 1513-1517 (1999).

[3] M. Ebrahim-Zadeh, "Continuous-wave optical parametric oscillators," in *OSA Handbook of Optics*, Vol. 4, (McGraw-Hill New York, 2010), Chap. 17, pp. 1-33.

[4] I. Breunig, D. Haertle, and K. Buse, "Continuous-wave optical parametric oscillators: recent developments and prospects," Appl. Phys. B 105, 99-111 (2011).

[5] M. Klein, C. Laue, D. Lee, K. Boller, and R. Wallenstein, "Diode-pumped singly resonant continuous-wave optical parametric oscillator with wide continuous tuning of the near-infrared idler wave," Opt. Lett. 25, 490-492 (2000).

[6] E. Kovalchuk, T. Schuldt, and A. Peters, "Combination of a continuous-wave optical parametric oscillator and a femtosecond frequency comb for optical frequency metrology," Opt. Lett. 30, 3141-3143 (2005).

[7] U. Warring, M. Amoretti, C. Canali, A. Fischer, R. Heyne, J. Meier, Ch. Morhard, and A. Kellerbauer, "High-resolution laser spectroscopy on the negative osmium ion," Phys. Rev. Lett. 102, 043001 (2009).

[8] D. Arslanov, M. Spunei, J. Mandon, S. Cristescu, S. Persijn, and F. Harren, "Continuous-wave optical parametric oscillator based infrared spectroscopy for sensitive molecular gas sensing," Laser Photonics Rev. 7, 188-206 (2013).

[9] D. Hum, M. Fejer, "Quasi-phasematching," C. R. Physique 8, 180-198 (2007).

[10] R. Batchko, D. Weise, T. Plettner, G. Miller, M. Fejer, and R. Byer, "Continuous-wave 532-nm-pumped singly resonant optical parametric oscillator based on periodically poled lithium niobate," Opt. Lett. 23, 168-170 (1998).

[11] U. Ströβner, A. Peters, J. Mlynek, S. Schiller, J. Meyn, and R. Wallenstein, "Single-frequency continuous-wave radiation from 0.77 to 1.73 µm generated by a green-pumped optical parametric oscillator with periodically poled $LiTaO_3$," Opt. Lett. 24, 1602-1604 (1999).

[12] K. Kitamura, Y. Furukawa, S. Takekawa, T. Hatanaka, H. Ito, and V. Gopalan, "Non-stoichiometric control of $LiNbO_3$ and $LiTaO_3$ in ferroelectric domain engineering for optical devices," Ferroelectrics 257, 235-243 (2001).

[13] G. Samanta and M. Ebrahim-Zadeh, "Continuous-wave singly-resonant optical parametric oscillator with resonant wave coupling," Opt. Express 16, 6883-6888 (2008).

[14] S. Zaske, D. Lee, C. Becher, "Green-pumped cw singly resonant optical parametric oscillator based on MgO:PPLN with frequency stabilization to an atomic resonance," Appl Phys B 98, 729-735 (2010).

[15] A. Garashi, A. Arie, A. Skliar, and G. Rosenman, "Continuous-wave optical parametric oscillator based on periodically poled $KTiOPO_4$," Opt. Lett. 23, 1739-1741 (1998).

[16] G. Gibson, M. Ebrahimzadeh, M. Padgett, and M. Dunn, "Continuous-wave optical parametric oscillator based on periodically poled $KTiOPO_4$ and its application to spectroscopy," Opt. Lett. 24, 397-399 (1999).

[17] M. Ebrahimzadeh, G. Turnbull, T. Edwards, D. Stothard, I. Lindsay, and M. Dunn, "Intracavity continuous-wave singly resonant optical parametric oscillators," J. Opt. Soc. Am. B 16, 1499-1511 (1999).

[18] T. Edwards, G. Turnbull, M. Dunn, and M. Ebrahimzadeh, "Continuous-wave, singly-resonant, optical parametric oscillator based on periodically poled $KTiOPO_4$," Opt. Express 6, 58-63 (2000).

[19] D. Weise, U. Ströβner, A. Peters, J. Mlynek, S. Schiller, A. Arie, A. Skliar, and G. Rosenman, "Continuous-wave 532-nm-pumped singly resonant optical parametric oscillator with periodically poled $KTiOPO_4$," Opt. Commun. 184, 329-333 (2000).

[20] U. Ströβner, J. Meyn, R. Wallenstein, P. Urenski, A. Arie, G. Rosenman, J. Mlynek, S. Schiller, and A. Peters, "Single-frequency continuous-wave optical parametric oscillator system with an ultrawide tuning range of 550 to 2830 nm," J. Opt. Soc. Am. B 19, 1419-1424 (2002).

[21] C. Liu, X. Guo, Z. Bai, X. Wang, and Y. Li, "High-efficiency continuously tunable single-frequency doubly resonant optical parametric oscillator," Appl. Opt. 50, 1477-1481 (2011).

[22] K. Devi and M. Ebrahim-Zadeh, "Room-temperature, rapidly tunable, green-pumped continuous-wave optical parametric oscillator," Opt. Lett. 42, 2635-2638 (2017).

[23] G. Hansson, H. Karlsson, S. Wang, and F. Laurell, "Transmission measurements in KTP and isomorphic compounds," Appl. Opt. 39(27), 5058-5069 (2000).

[24] T. Fan, C. Huang, B. Hu, R. Eckardt, Y. Fan, R. Byer, and R. Feigelson, "Second harmonic generation and accurate index of refraction measurements in flux-grown $KTiOPO_4$," Appl. Opt. 26, 2390-2394 (1987).

[25] W. Wiechmann, S. Kubota, T. Fukui, and H. Masuda, "Refractive-index temperature derivatives of potassium titanyl phosphate," Opt. Lett. 18, 1208-1210 (1993).

[26] K. Fradkin, A. Arie, A. Skliar, and G. Rosenman, "Tunable midinfrared source by difference frequency generation in bulk periodically poled $KTiOPO_4$," Appl. Phys. Lett. 74, 914-916 (1999).

[27] K. Kato and E. Takaoka, "Sellmeier and thermo-optic dispersion formulas for KTP," Appl. Opt. 41, 5040-5044 (2002).

[28] S. Emanueli and A. Arie, "Temperature-dependent dispersion equations for $KTiOPO_4$ and $KTiOAsO_4$.," Appl. Opt. 42, 6661-6665 (2003).

Chapter 4

Continuous-wave tunable mid-infrared source based on orientation-patterned gallium phosphide

4.1 Background and motivation

Coherent monochromatic light sources in the mid-infrared (mid-IR) spectral range are of great interest in fundamental research, industry, and security domain [1]. Such sources offer a wide variety of applications from trace gas detection in environmental monitoring to sensitive chemical and biomolecular sensing in medical diagnostics [2]. In the mid-IR, the spectral range of 3-5 µm is particularly important for molecular spectroscopy, because it contains fundamental vibrational bands associated with C-H, N-H and O-H stretches of several molecules [3]. Hence, their vibrational transitions exhibit stronger line strengths in this region than their overtones typically observed in the visible and near-infrared (near-IR) regions. In order to exploit this property for high-resolution spectroscopy of corresponding molecules, narrow-linewidth continuous-wave (cw) sources providing tunable mid-IR light are of utmost importance [4]. Two major technologies for producing high-power tunable cw mid-IR radiation are quantum cascade lasers (QCLs) [5] and nonlinear frequency-conversion techniques such as difference-frequency-generation (DFG) [6] and optical parametric oscillators (OPOs) [7].

In the spectral window of 3-5 µm, QCLs represent attractive tunable sources capable of delivering multi-watt cw powers [8]. However, they

suffer from a trade-off between the high output powers and diffraction-limited beams [9]. On the other hand, OPOs serve as an effective alternative to achieve high beam quality, by transferring favourable characteristics of near-IR solid-state lasers to the mid-IR wavelength range with continuous tuning and high conversion efficiencies. Several demonstrations of cw OPOs accessing wide wavelength tuning ranges have been reported to date, by exploiting quasi-phase-matched nonlinear materials [10]. Particularly, MgO-doped periodically-poled $LiNbO_3$ (MgO:PPLN) crystals have been extensively used in different OPO cavity configurations along with the variety of grating period designs to attain multi-watt output powers across the mid-IR wavelength range up to $\sim$4 µm [11–14]. Likewise, MgO-doped stoichiometric periodically-poled $LiTaO_3$ (MgO:sPPLT) crystal has been used in singly-resonant oscillator (SRO) configuration, extracting $>$4 W across 60% of the 3-3.4 µm tuning range [15]. Also, periodically-poled $RbTiOAsO_4$ (PPRTA) was used in a pump-enhanced cavity configuration delivering multi-milliwatt cw powers across 3.2-3.5 µm [16].

The above mentioned ferroelectric nonlinear crystals, including periodically poled $KTiOPO_4$ (PPKTP), have also been employed in various cw tunable mid-IR DFG setups [6, 17]. Although MgO:PPLN has been primarily used for long-wavelength operation, its optical transmittance starts falling off above $\sim$3.6 µm [18]. Similarly, the transmission window for all oxide-based dielectric materials is limited by an intrinsic onset of multiphonon absorption. Due to the strong absorption losses at the generated wavelengths above $\sim$4 µm, these nonlinear crystals inherently suffer from thermal lensing, and hence material damage. In the case of OPOs, partial idler absorption increases oscillation thresholds, resulting in reduced conversion efficiencies.

Nevertheless, these fundamental impediments to wavelength generation beyond $\sim$4 µm can be circumvented by using non-oxide nonlinear crystals, namely semiconductors. They offer broad transparency windows deep into the mid-IR, as well as many other desirable properties, including

much higher nonlinear coefficients and better thermal conductivities as compared to the oxide-based materials [1, 19]. Semiconductors are also free of photorefractive effects that afflict ferroelectric materials. In early years, birefringent semiconductors such as $AgGaSe_2$ (AGSe), $CdGeAs_2$ (CGA), $AgGaS_2$ (AGS), $LiInS_2$ (LIS), $LiInSe_2$ (LISe), and GaSe have been used to demonstrate cw DFG sources providing broad wavelength tuning capabilities with the longest wavelength up to ∼19 µm into the deep mid-IR [20]. However, the generated mid-IR powers were restricted to nW level. Later, cubic zincblende semiconductors such as GaAs and GaP were considered as potential gain media for downconversion. However, their optical isotropy precluded birefringent phase-matching, which limited the utility of these nonlinear crystals. Moreover, the traditional periodic poling technique used to enable quasi-phase-matching (QPM) in ferroelectric crystals is not applicable to non-ferroelectric materials. Therefore, novel methods were developed in order to obtain the periodic pattern of alternately oriented domains in these semiconductors, hence the term orientation-patterned (OP) materials [21].

The advances in fabrication technology has led to the development of practical quasi-phase-matched semiconductor nonlinear crystals. OP-GaAs (gallium arsenide) was the first semiconductor material which exhibited the potential for QPM, followed by the demonstration of a cw tunable DFG with the maximum of 51 mW power at 6.8 µm [22]. On the other hand, OP-GaP (gallium phosphide) is the most recently developed quasi-phase-matched crystal, which offers wide transparency across ∼0.85-12 µm, large optical nonlinearity (d_{14}=70.6 pm/V), and high thermal conductivity (110 W/m.K) [23]. These quasi-phase-matched semiconductor materials exhibit much higher nonlinearities and wider transparency ranges than conventional MgO:PPLN, as depicted in Figure 4.1. As seen, OP-GaP exhibits lower nonlinearity compared to OP-GaAs. However, since the next-generation quasi-phase-matched semiconductor OP-GaP has a larger bandgap than OP-GaAs, it has lower two-photon absorption in the convenient pumping

range of ∼1 µm. On the other hand, OP-GaAs requires long-wavelength pumping with limited availability of ∼2 µm lasers, or the deployment of additional sources for cascaded pumping schemes. Therefore, OP-GaP is more appealing for efficient frequency downconversion into mid-IR.

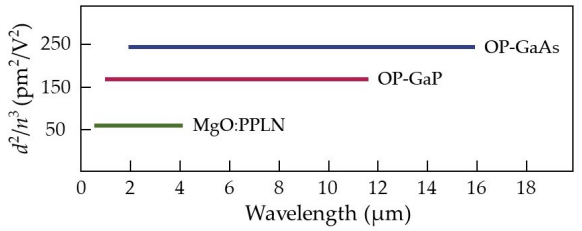

Figure 4.1: Nonlinear figure of merit versus transparency range of quasi-phase-matched nonlinear materials; currently used for cw mid-IR generation.

Despite the developments in the quasi-phase-matched semiconductor materials, cw mid-IR OPO operation based on non-oxide nonlinear crystals is yet to be demonstrated. It remains challenging due to the intrinsically high threshold powers under low cw pumping intensities, which in turn requires high-quality, low-loss nonlinear crystals, good coatings and mirrors. On the other hand, single-pass DFG approach does not require the attainment of an oscillation threshold, and thus can be considered as an attractive alternative for cw mid-IR generation. Recently, OP-GaP has been explored for cw DFG sources at fixed wavelengths of 3.4 µm [24] and 5.85 µm [25]. Both demonstrations were based on typically used 1064 nm-pumping systems. Table 4.1 summarises the results of these earlier reports.

λ_{pump}	λ_{signal}	λ_{DFG}	P_{pump}	P_{signal}	P_{DFG}	$L_{crystal}$	$\Lambda_{crystal}$	Ref.
1064 nm	1550 nm	3400 nm	47 W	24 W	150 mW	16.5 mm	20.8 µm	[24]
1064 nm	1301 nm	5850 nm	10 W	40 mW	65 µW	24.6 mm	24 µm	[25]

Table 4.1: Earlier reports on cw DFG in OP-GaP.

Given the significance of recent advances in OP-GaP as a promising new mid-IR nonlinear material, it is important to study tunable wavelength generation in this crystal. Also, considering the transmission properties of OP-GaP, long-wavelength-pumped devices are desirable. Here we report, for the first time to the best of our knowledge, the generation of tunable cw radiation across 4608-4694 nm based on 2 µm-pumped DFG in OP-GaP, with >30 mW mid-IR output power across 96% of the DFG tuning range, in the high spatial beam quality.

4.2 Experimental setup

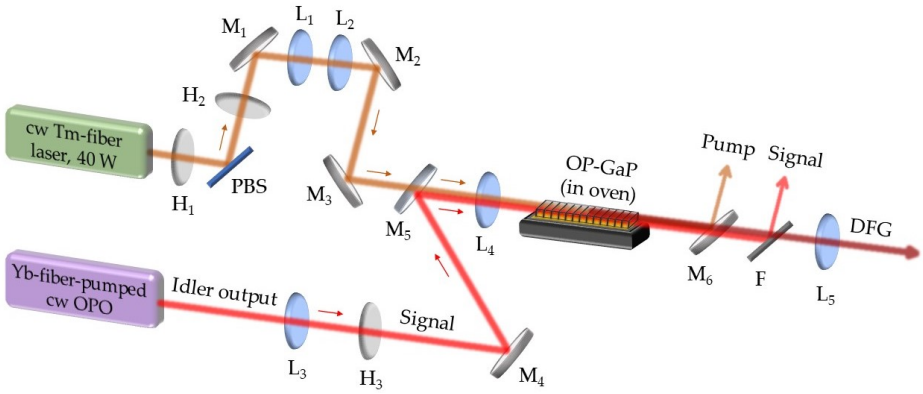

Figure 4.2: Schematic of the experimental setup. H_{1-3}, half-wave plates; PBS, polarizing beam-splitter plate; M_{1-6}, mirrors; L_{1-5}, lenses; F, filter.

A schematic of the experimental setup is shown in Figure 4.2. The pump source is a commercial cw Tm-fiber laser (IPG Photonics, TLR-50-2010-LP), delivering up to 40 W of output power at 2010 nm in a linearly polarized beam. The laser is operated at maximum power, and the input pump power for DFG is adjusted using a combination of half-wave plate H_1 and polarizing beam-splitter (PBS) plate. A second half-wave plate H_2 is placed to control the pump polarization for phase-matching inside the

OP-GaP crystal. Lenses L_1 and L_2 are used to adjust the Tm-fiber pump beam diameter. The input signal for DFG is the idler output beam derived from a home-built cw OPO, based on a 38-mm-long MgO:PPLN crystal with a grating period of Λ_{OPO}=30 µm, pumped by a commercial cw Yb-fiber laser (IPG Photonics, YLR-30-1064-LP-SF) delivering up to 30 W of output power at 1064 nm in a single-frequency, linearly polarized beam with M^2<1.01. The SRO provides up to ∼2.5 W of tunable cw output power in the non-resonant idler beam across 3370-3620 nm. The OPO idler output power is adjusted by changing the Yb-fiber pump power through a variable attenuator. Lens L_3 is used to collimate the idler beam (hereinafter DFG input signal) and a tunable, uncoated MgF_2 half-wave plate H_3 is used to control the incident signal polarization for phase-matching in the DFG process. The tilt angle of H_3 is adjusted for optimum performance at any given signal wavelength. Plane mirror M_1 is used to steer the Tm-fiber pump beam, while two pairs of plane mirrors $M_{2,3}$ and $M_{4,5}$ are used to optimize the spatial overlap of the Tm-fiber pump beam and input signal beam on lens L_4, respectively. Mirror M_5 is highly transmitting (T>99%) for the pump (at 2010 nm), while reflective (R>90%) for the input signal (over 3370-3620 nm). OP-GaP crystal used for DFG is grown using all-epitaxial approach at BAE Systems, USA. The crystal is 40-mm-long with a grating period of Λ_{DFG}=85.1 µm. The crystal has a physical aperture of 6-mm-wide and 1.7-mm-thick. End-faces of the crystal are antireflection (AR)-coated (R<1%) over 1.98-2.1 µm, 3.3-3.75 µm and 4.45-4.8 µm. The OP-GaP crystal is housed in an oven with a stability of ±0.1 °C, which can be controlled from room temperature to 200 °C. A single lens L_4 is used to focus both pump and signal beams at the center of the OP-GaP crystal. Dichroic mirror M_6 is used to separate the pump, while filter F is used to separate the signal from generated output beam. Lens L_5 is used to collimate the DFG output beam.

4.3 Results

Initially, different focal lengths for the lens L_4 were deployed in order to investigate tighter and looser focusing for both the pump and signal beams with smaller beam waist radii, w_{0p}∼47.5 µm (ξ_p∼1.8) and w_{0s}∼69 µm (ξ_s∼1.7), respectively, and larger beam waist radii, w_{0p}∼97 µm (ξ_p∼0.4) and w_{0s}∼130 µm (ξ_s∼0.5), respectively, at the center of the OP-GaP crystal. This resulted in lower DFG output powers, which is attributed to reduced spatial overlap of the pump and signal beams within the OP-GaP crystal. Hence, the optimum focusing (f=300 mm) was used to generate the maximum DFG powers, owing to the pump and signal beam waist radii of w_{0p}∼52 µm and w_{0s}∼80 µm, corresponding to the confocal focusing parameters of ξ_p∼1.5 and ξ_s∼1.3, respectively.

In the DFG experiment described here, the polarization directions of both the incident pump and signal beams could be controlled independently, in order to investigate dependence of the generated DFG power on the polarization directions of the input beams. Figure 4.3 shows the different polarization directions along the OP-GaP crystal axes. The polarization direction [11$\bar{1}$] lies on the incident (and exit) face of the crystal, perpendicular to the propagation direction [0$\bar{1}\bar{1}$]. The polarization-dependent transmission of the OP-GaP crystal was characterized by varying the polarization of the input pump and signal beams using half-wave plates H_2 and H_3, respectively. At first, the transmission measurements were performed by keeping the polarization of both input beams along the [11$\bar{1}$] direction, for which the maximum DFG power in OP-GaP was generated. The results, obtained at wavelengths 2010 and 3557 nm, are shown in Figure 4.4. The transmitted power has a linear dependence on the input powers, with the transmission of 75.1% and 62.7% at λ_{pump}=2010 nm and λ_{signal}=3557 nm, respectively. By changing the pump polarization to [01$\bar{1}$] direction and signal polarization to any arbitrary direction, the DFG efficiency was observed to decrease by ∼40%. Under this condition, however, the transmission for the pump beam

along [01$\bar{1}$] direction was measured to be 76.5%. The lower transmission measured at any polarization direction in the present OP-GaP crystal could be due to the absorption at these input wavelengths, which may be the result of possible diffusion of impurities from the GaP substrate wafer into the hydride vapour phase epitaxy (HVPE)-grown quasi-phase-matched layer or due to the silicon impurities originated during the fabrication process.

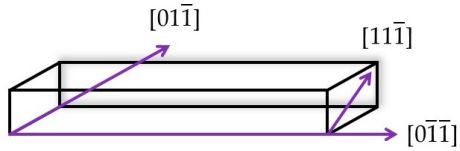

Figure 4.3: Polarization directions along OP-GaP crystal axes.

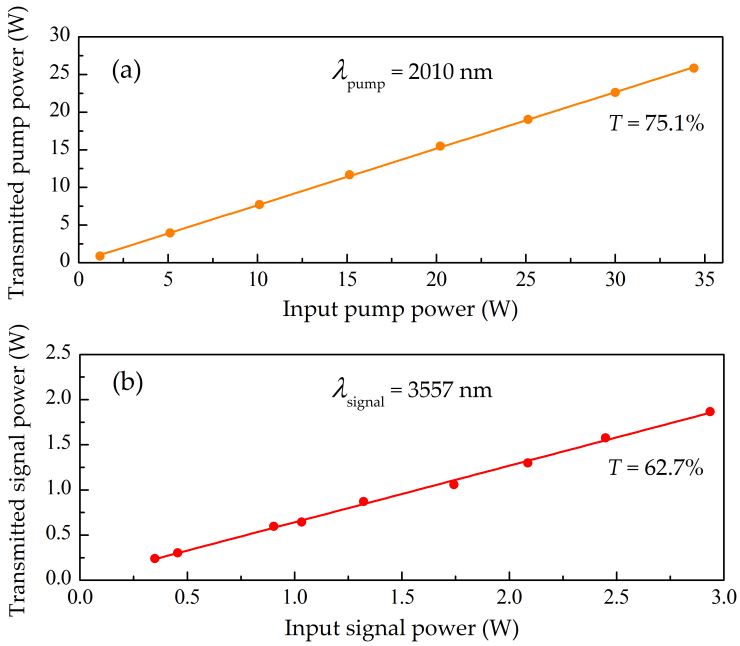

Figure 4.4: Transmission of 40-mm-long OP-GaP sample with polarization along [11$\bar{1}$] direction for (a) pump and (b) signal, respectively.

The spectral tuning characteristics of the DFG output in the mid-IR were studied by tuning the input signal, namely the OPO idler wavelength. By varying the MgO:PPLN crystal temperature, T_{OPO}, over 80-115 ^{o}C, OPO idler could be tuned across 3557-3505 nm. By simultaneously adjusting the phase-matching temperature of the OP-GaP crystal, T_{DFG}, over 25-32 ^{o}C, the DFG output was tuned across 4608-4694 nm. The phase-matching temperatures of the crystals, T_{OPO} and T_{DFG}, are the recorded temperatures of the ovens.

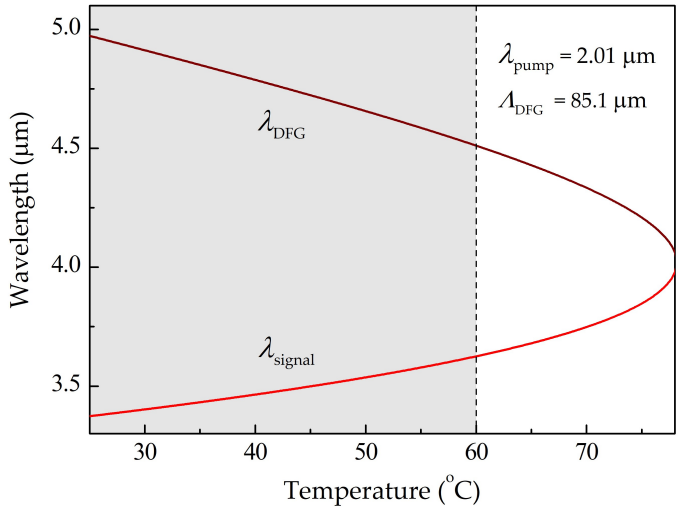

Figure 4.5: Theoretical temperature tuning curve for DFG in OP-GaP. The shaded region shows the output DFG and input signal wavelength range obtained using MgO:PPLN with Λ_{OPO}=30 μm.

It is to be noted that for the fixed pump wavelength of 2.010 μm, and with the given OP-GaP grating period Λ_{DFG}=85.1 μm, a theoretically calculated DFG tuning range across 4.97-4.05 μm could be obtained, by tuning the input signal over 3.37-3.98 μm and simultaneously varying T_{DFG} over 25-78 ^{o}C. This is shown in Figure 4.5, in which the theoretical temperature tuning curve was calculated using the relevant Sellmeier equations for

OP-GaP [26]. However, in the present work, with the single grating period Λ_{OPO}=30 µm of the MgO:PPLN crystal, the DFG input signal (OPO output idler) could be tuned across 3.37-3.62 µm, shown as the shaded region in Figure 4.5, resulting in the theoretical DFG tuning range across 4.97-4.51 µm. However, in our experiment, the generation of DFG wavelengths above 4694 nm was limited by the oven, requiring temperatures below 25 °C. Given the low output powers at longer OPO idler wavelengths with the current MgO:PPLN crystal, we performed the DFG spectral tuning down to 4608 nm.

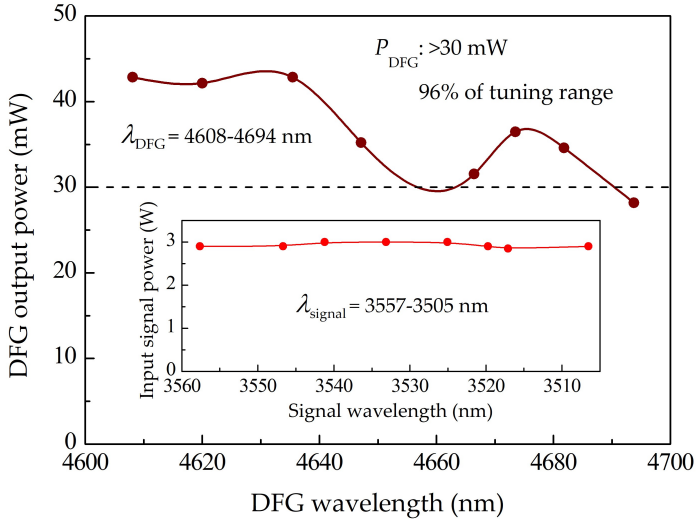

Figure 4.6: Variation of DFG power across DFG wavelength tuning range. Inset: corresponding signal power across signal wavelength tuning range.

While maintaining the optimum polarization along [11$\bar{1}$] direction for both the pump and signal beams into the OP-GaP crystal, the DFG output power was measured across the DFG wavelength tuning range for the maximum available Tm-fiber input pump power of 34 W and the maximum input signal power of ∼3 W at all signal wavelengths. The results are shown in Figure 4.6. The DFG output power reaches the maximum

of 43 mW at 4608 and 4635 nm, providing >40 mW over 37% and >30 mW over 96% of the full tuning range. The inset of Figure 4.6 shows the corresponding variation of the signal power across the signal wavelength tuning range of 3557-3505 nm as T_{OPO} was varied over 80-115 ^{o}C.

Simultaneously, the DFG spectra across the DFG wavelength tuning range were measured using a spectrum analyzer (Bristol 721) with a spectral resolution of 6 GHz in the mid-IR. The results are shown in Figure 4.7. As can be seen, the spectrum at all wavelengths has a full-width at half-maximum (FWHM) linewidth of ∼3 nm (∼42 GHz). Although, the input signal (OPO idler) beam is single-frequency, the finite Tm-fiber pump laser bandwidth of ∼0.7 nm resulted in the finite linewidth of the DFG output spectrum.

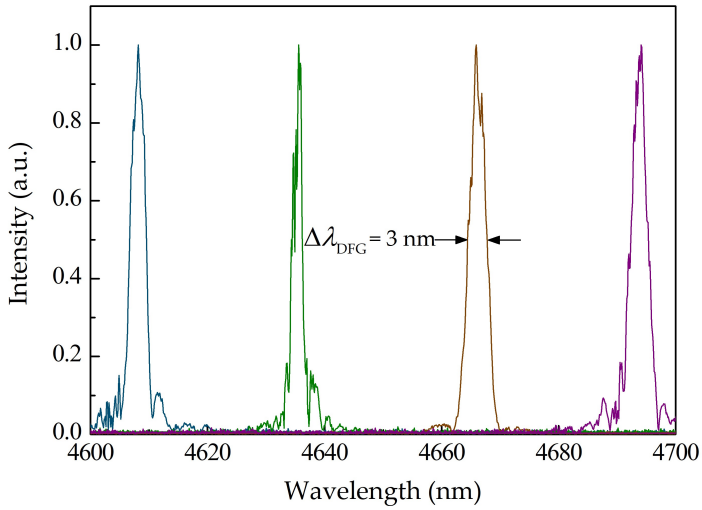

Figure 4.7: DFG spectra across wavelength tuning, at maximum input powers.

To study the power scaling capability of the source, variation of the DFG output power was recorded as a function of the incident pump and signal power, while keeping either of the input powers fixed. Figure 4.8 shows the DFG power at 4608 nm versus the pump power, with the input

signal power fixed at 2.9 W. The DFG power increases linearly with the increasing pump power, reaching 43 mW for 34 W of input pump power. To generate the maximum DFG power, the OP-GaP crystal temperature was optimized at each pump power level. Also shown in Figure 4.8 is the change in T_{DFG} with variation in the pump power, where a drop from 44 °C to 25 °C was recorded as the pump power was increased from 1.2 W to 34 W. This implies heating of the crystal at high input pump powers, which is attributed to significant absorption in the OP-GaP sample.

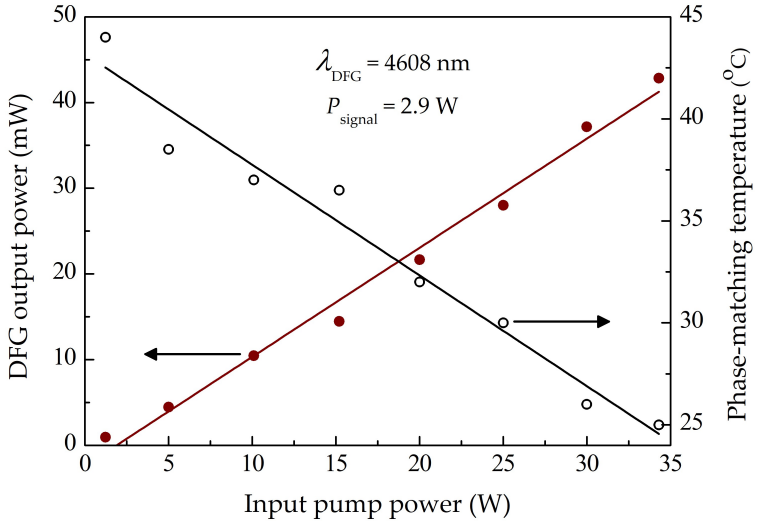

Figure 4.8: Dependence of DFG power and OP-GaP phase-matching temperature on incident pump power. The solid lines are a guide to the eye.

As seen in Figure 4.9, the DFG output power at 4608 nm was recorded as a function of the input signal power, together with the corresponding variation in the phase-matching temperature of the OP-GaP crystal, while keeping the pump power fixed. To minimize constant heating of the crystal at the high pump powers, P_{pump} was limited to 10 W and the input signal power was varied from minimum up to the maximum of 2.9 W. The DFG power increases linearly with the input signal power, but T_{DFG} was

observed to remain constant with the increasing signal power. This was to be expected, given that both the pump and maximum input signal powers were relatively low, resulting in negligible heating in the OP-GaP crystal, despite significant absorption. During these measurements, a change in wavelength of the DFG input signal (OPO idler) was also observed with the increasing Yb-fiber power while pumping the OPO. The DFG input signal wavelength was measured to decrease by ∼5 nm as the DFG input signal power was increased from 1 to 2.9 W. Hence, for attainment of the optimum phase-matching for DFG, the temperature of the OP-GaP crystal had to be increased initially by ∼0.6 °C with the increase in P_{signal}. Later, this temperature rise was balanced by cooling the crystal to compensate for the heating effect at the high signal powers.

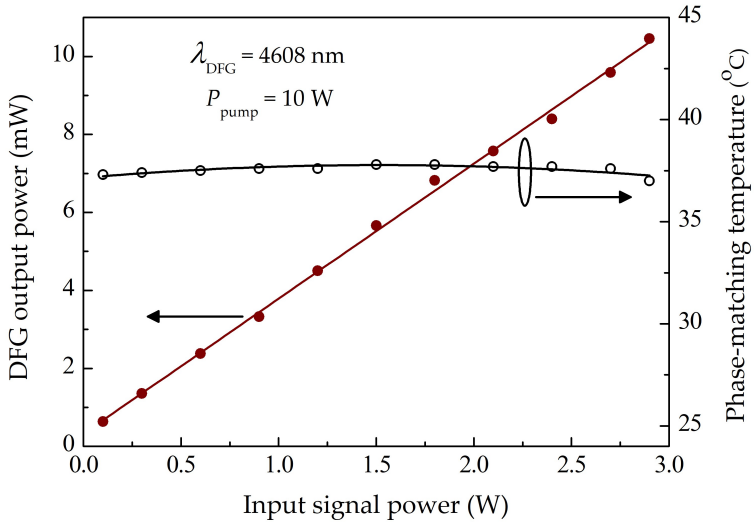

Figure 4.9: Dependence of DFG power and OP-GaP phase-matching temperature on incident signal power. The solid lines are a guide to the eye.

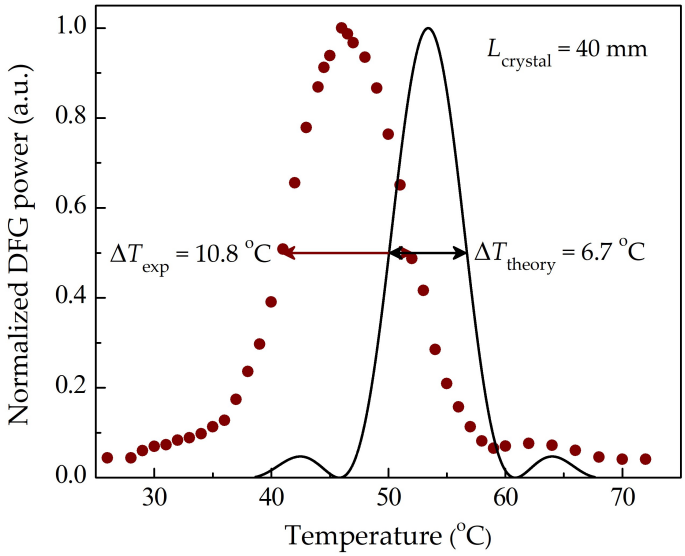

Figure 4.10: Experimentally measured (solid circle), and theoretically calculated (solid line) DFG temperature acceptance bandwidth for 40-mm-long OP-GaP.

The temperature acceptance bandwidth measurements were performed for DFG at 4608 nm. To minimize thermal contributions, the measurements were performed at the input pump power of 5 W and signal power of 1 W, using the loose focusing (w_{0p}∼97 µm, w_{0s}∼130 µm). The temperature acceptance bandwidth was determined by measuring variation of the DFG output power as a function of the OP-GaP crystal temperature. The result is shown in Figure 4.10. The experimental FWHM temperature acceptance bandwidth was recorded to be ΔT_{exp}=10.8 °C at T_{DFG}=46 °C. Also shown in Figure 4.10 is the theoretical temperature acceptance curve calculated using the relevant Sellmeier equations of OP-GaP, for the 40-mm-long crystal, assuming the single-frequency input beams in the plane-wave approximation [26]. Theoretical FWHM bandwidth was obtained to be ΔT_{theory}=6.7 °C at the phase-matching temperature of T_{theory}=53.4 °C. The discrepancy between the experimental and theoretical values of the tem-

perature acceptance bandwidth could be due to the finite bandwidth of the Tm-fiber pump laser ($\Delta\lambda_{pump}$~0.7 nm) and the plane-wave approximation considered in theoretical calculations. On the other hand, the discrepancy in the phase-matching temperature values under minimum thermal contribution could be due to the possible non-uniformity in the grating period along the 40-mm-long OP-GaP sample, as well as the non-negligible absorption in the crystal.

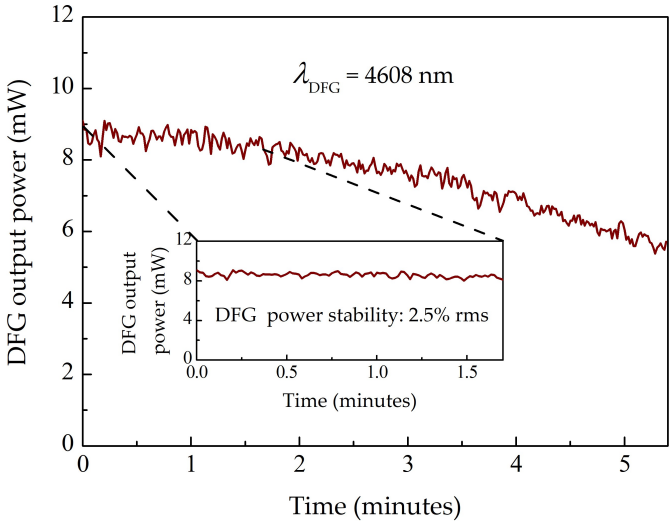

Figure 4.11: Passive power stability of DFG output over 5 minutes. Inset: zoomed version of the DFG output passive power stability over initial 1 min 40 s.

The passive power stability of the DFG output at 4608 nm was also recorded at the input Tm-fiber pump power of 10 W and signal power of 2.6 W under free-running conditions. The result is shown in Figure 4.11. As seen, the generated DFG power decreases from 9 mW to 5.4 mW over 5 minutes at the fixed input powers. The drop in the output power was observed with a rise in the crystal temperature from 38 ^{o}C to 42.5 ^{o}C. Hence, this consequent drop is attributed to the change in the phase-matching temperature. The DFG power exhibits the passive stability better than 2.5%

rms over the initial 1 minute 40 seconds, before the onset of rise in the crystal temperature, as shown in the inset of Figure 4.11. The instability in power over this time duration could be due to mechanical vibrations and air currents in the laboratory and possible mode-hopping in the OPO idler in the absence of active stabilization. No damage was observed to the crystal or AR coatings even after the long-term operation.

The far-field energy distribution of the collimated DFG output at 4608 nm, at the maximum input pump and signal powers, was recorded using a Pyrocam III camera, as shown in Figure 4.12. The result confirms excellent spatial quality with a beam circularity >92%. Similar profiles were obtained across the entire DFG tuning range. Figure 4.12 also shows the far-field energy distribution of the input signal (3557 nm) and pump (2010 nm) beams, with circularities of >93% and >97%, respectively. As evident, the beam quality was transferred from the input pump and signal to the DFG output, and no degradation in the DFG beam profile was observed at the maximum input powers. Further, no variation in the spatial mode of the input and output pump and signal beams was observed throughout our experiments, indicating the absence of thermal lensing in the crystal.

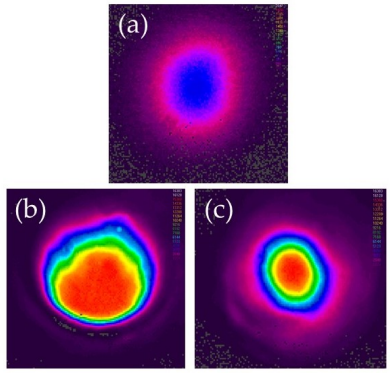

Figure 4.12: Far-field energy distribution of (a) DFG output beam, (b) input signal beam, and (c) input pump beam, at maximum input powers.

4.4 Conclusion

In this chapter, we have reported the first tunable cw DFG source based on OP-GaP crystal, using a 40-mm-long sample with a single grating period of Λ_{DFG}=85.1 µm. The demonstrated DFG source is tunable in the mid-IR across 4608-4694 nm. By exploiting single-pass DFG between the cw Tm-fiber laser and the cw OPO based on MgO:PPLN, we have generated up to 43 mW power at 4608 nm and 4635 nm, with >30 mW power across 96% of the complete tuning range. The DFG source exhibits a passive power stability better than 2.5% rms over 1.7 minutes, measured at 4608 nm. The absence of saturation in the output power at higher pump powers suggests the possibility of further scaling of the DFG power, but with the improved crystal quality. The enhanced crystal transmission would also result in the improved output power stability over the longer time duration by reducing the thermal loading of the crystal.

The recorded DFG spectra have FWHM linewidth of 3 nm, while the DFG beam circularity is >92% at 4608 nm with the excellent spatial beam quality across the entire DFG tuning range. The experimentally obtained FWHM temperature acceptance bandwidth of DFG is 10.8 ^{o}C at the phase-matching temperature of 46 ^{o}C, whereas the theoretically calculated values are slightly different. This discrepancy can be partly attributed to the duty-cycle errors in the crystal gratings. We have also studied the polarization-dependent transmission of the OP-GaP crystal, which shows non-negligible absorption of the DFG input wavelengths in the given sample.

The results demonstrate the potential of OP-GaP for the generation of practical cw mid-IR radiation across the difficult spectral region of 4-5 µm, which is of interest for many demanding applications. However, by improving the optical transmission quality and grating period uniformity, one can expect even higher output efficiencies in such cw DFG sources. Furthermore, using the same Tm-fiber laser at 2.01 µm and signal wavelengths across 3.37-3.62 µm (the complete tuning range of the OPO idler

for Λ_{OPO}=30 µm), with the OP-GaP crystal having a slightly longer grating period Λ_{DFG}=87 µm, the DFG spectral tuning can be extended up to 5 µm with higher output powers.

References

[1] M. Ebrahim-Zadeh and I. Sorokina, eds., *Mid-Infrared Coherent Sources and Applications* (Springer Netherlands, 2008).

[2] F. Tittel, R. Lewicki, M. Jahjah, B. Foxworth, Y. Ma, L. Dong, R. Griffin, K. Krzempek, P. Stefanski, and J. Tarka, "Mid-infrared laser based gas sensor technologies for environmental monitoring, medical diagnostics, industrial and security applications," in *Terahertz and Mid Infrared Radiation: Detection of Explosives and CBRN (Using Terahertz)* (Springer Netherlands, 2014), pp. 153-165.

[3] M. Vainio and L. Halonen, "Mid-infrared optical parametric oscillators and frequency combs for molecular spectroscopy," Phys. Chem. Chem. Phys. 18, 4266-4294 (2016).

[4] F. Tittel, D. Richter, and A. Fried "Mid-infrared laser applications in spectroscopy," in *Solid-State Mid-Infrared Laser Sources* (Springer Berlin Heidelberg, 2003), pp. 458-529.

[5] P. Figueiredo, M. Suttinger, R. Go, E. Tsvid, C. Patel, and A. Lyakh, "Progress in high-power continuous-wave quantum cascade lasers [Invited]," Appl. Opt. 56, H15-H23 (2017).

[6] W. Chen, J. Cousin, E. Poullet, J. Burie, D. Boucher, X. Gao, M. Sigrist, and F. Tittel, "Continuous-wave mid-infrared laser sources based on difference frequency generation," C. R. Physique 8, 1129-1150 (2007).

[7] M. Ebrahim-Zadeh and M. Dunn, "Optical parametric oscillators," in *OSA Handbook of Optics*, Vol. 4, (McGraw-Hill New York, 2000). Chap. 22, pp. 1-72.

[8] M. Razeghi, N. Bandyopadhyay, Y. Bai, Q. Lu, and S. Slivken, "Recent advances in mid infrared (3-5μm) Quantum Cascade Lasers," Opt. Mater. Express 3, 1872-1884 (2013).

[9] S. Slivken, S. Sengupta, and M. Razeghi, "High power continuous operation of a widely tunable quantum cascade laser with an integrated amplifier," Appl. Phys. Lett. 107, 251101(1-4) (2015).

[10] M. Ebrahim-Zadeh, "Continuous-wave optical parametric oscillators," in *OSA Handbook of Optics*, Vol. 4, (McGraw-Hill New York, 2010), Chap. 17, pp. 1-33.

[11] W. Bosenberg, A. Drobshoff, J. Alexander, L. Myers, and R. Byer, "93% pump depletion, 3.5-W continuous-wave, singly resonant optical parametric oscillator," Opt. Lett. 21, 1336-1338 (1996).

[12] P. Powers, T. Kulp, and S. Bisson, "Continuous tuning of a continuous-wave periodically poled lithium niobate optical parametric oscillator by use of a fan-out grating design," Opt. Lett. 23, 159-161 (1998).

[13] M. van Herpen, S. Bisson, and F. Harren, "Continuous-wave operation of a single-frequency optical parametric oscillator at 4-5 μm based on periodically poled $LiNbO_3$," Opt. Lett. 28, 2497-2499 (2003).

[14] S. Kumar, R. Das, G. Samanta, and M. Ebrahim-Zadeh, "Optimally-output-coupled, 17.5 W, fiber-laser-pumped continuous-wave optical parametric oscillator," Appl. Phys. B 102, 31-35 (2011).

[15] S. Kumar and M. Ebrahim-Zadeh, "High-power, continuous-wave, mid-infrared optical parametric oscillator based on MgO:sPPLT," Opt. Lett. 36, 2578-2580 (2011).

[16] I. Lindsay, D. Stothard, C. Rae, and M. Dunn, "Continuous-wave pump-enhanced optical parametric oscillator based on periodically poled $RbTiOAsO_4$," Opt. Express 11, 134-140 (2003).

[17] K. Fradkin, A. Arie, A. Skliar, and G. Rosenman, "Tunable midinfrared source by difference frequency generation in bulk periodically poled $KTiOPO_4$," Appl. Phys. Lett. 74, 914-916 (1999).

[18] L. Myers, W. Bosenberg, R. Eckardt, M. Fejer, and R. Byer, "Multigrating quasi-phase-matched optical parametric oscillator in periodically poled $LiNbO_3$," Opt. Lett. 21, 591-593 (1996).

[19] D. Nikogosyan, *Nonlinear Optical Crystals: A Complete Survey*, (Springer-Verlag New York, 2005).

[20] V. Petrov, "Frequency down-conversion of solid-state laser sources to the mid-infrared spectral range using non-oxide nonlinear crystals," Prog. Quantum Electron. 42, 1-106 (2015).

[21] C. Lynch, D. Bliss, T. Zens, A. Lin, J. Harris, P. Kuo, and M. Fejer, "Growth of mm-thick orientation-patterned GaAs for IR and THz generation," J. Cryst. Growth 310, 5241-5247 (2008).

[22] K. Devi, P. Schunemann, and M. Ebrahim-Zadeh, "Continuous-wave, multi-milliwatt, mid-infrared source tunable across 6.4-7.5 μm based on orientation-patterned GaAs," Opt. Lett. 39, 6751-6754 (2014).

[23] P. Schunemann, K. Zawilski, L. Pomeranz, D. Creeden, and P. Budni, "Advances in nonlinear optical crystals for mid-infrared coherent sources," J. Opt. Soc. Am. B 33, D36-D43 (2016).

[24] S. Guha, J. Barnes, and P. Schunemann, "Mid-wave infrared generation by difference frequency mixing of continuous wave lasers in orientation-patterned Gallium Phosphide," Opt. Mater. Express 5, 2911-2923 (2015).

[25] G. Insero, C. Clivati, D. Ambrosio, P. Natale, G. Santambrogio, P. Schunemann, J. Zondy, and S. Borri, "Difference frequency generation in the mid-infrared with orientation-patterned gallium phosphide crystals," Opt. Lett. 41, 5114-5117 (2016).

[26] L. Pomeranz, P. Schunemann, D. Magarrell, J. McCarthy, K. Zawilski, D. Zelmon, "1-μm-pumped OPO based on orientation-patterned GaP," Proc. SPIE 9347, 93470K(1-7) (2015).

Chapter 5

Noise in short-wavelength-pumped infrared upconversion detectors

5.1 Background and motivation

Infrared (IR) sensing and detection, especially for mid-IR spectroscopy and imaging is highly demanding in a multitude of scientific and industrial sectors [1, 2]. Newly emerging applications call for complete detection systems, consisting of tunable and stable excitation sources together with fast and sensitive detectors [3, 4]. The rapid development in narrow-linewidth infrared parametric downconversion sources over the decades has been seen so far in the previous chapters of this thesis. Similarly, high-brightness sources like supercontinuum in the mid-IR have also improved over the past years to achieve broadband trace gas sensing [5]. However, direct mid-IR detection technology has attained the saturation due to the fundamental limit on the use of traditional semiconductor detectors. Low noise detection at room temperature using conventional mid-IR detectors such as PbSe, InSb, HgCdTe pose restrictions due to the intrinsic thermal background radiation coming from these low bandgap materials itself [6]. Thermal detectors suffer from low sensitivity and slow response time [7]. On the other hand, high performance of photodetectors is hampered at room temperature operation [8], resulting in high operational cost required for cooling of such detectors.

A variety of detector materials and detection techniques based on different physical principles have been studied to date to achieve the maximum possible signal-to-noise ratio (SNR) [9]. One of the promising technologies

used for IR detection is frequency upconversion based on $\chi^{(2)}$ nonlinear materials [10]. The sum-frequency generation (SFG) i.e. upconversion process spectrally translates the long-wavelength IR signal into corresponding visible/near-IR output by virtue of three-wave-mixing, which allows high-performance detection via cost-effective Si/InGaAs detectors [11]. Measuring the upconverted light using this method usually results in a higher SNR than that of measuring the IR signal directly. Most importantly, UCDs enable fast mid-IR detection even at room temperature operation [12].

Upconversion systems based on quasi-phase-matching (QPM) materials have been exploited extensively for imaging and spectroscopic applications [13–15]. Additionally, intracavity design of pump laser in compact UCD modules provides high upconversion efficiency [16]. One of such UCD has been successfully deployed in on-field experiments for range-resolved DIAL measurement of atmospheric CH_4 [17]. Likewise, in the last decade, upconversion detection systems have emerged as an alternative technique for single-photon counting in the mid-IR [18] and are being routinely used, enjoying advantage of PPLN waveguide structures [19, 20].

In order to achieve maximum upconversion efficiency high-intensity pump field is required to be focused inside the nonlinear crystal. However, this usually leads to unintended nonlinear optical processes, i.e., additional UCD noise sources, such as upconverted spontaneous parametric down-conversion (USPDC) [21, 22], upconverted spontaneous Raman scattering [23], and upconverted thermal radiation [24]. The USPDC noise exists only in the short-wavelength-pumped UCDs ($\lambda_p < \lambda_{IR}$, where λ_p and λ_{IR} are wavelengths of the pump and input IR signal, respectively). When QPM devices are used, normally phase-mismatched SPDC process is enhanced due to the random duty cycle (RDC) error in the periodically structured QPM materials thereby increasing USPDC noise [25, 26]. For cases in which USPDC is the dominant noise source, typical dark count rate (DCR) of the UCD is larger than 10^5/s [22]. The use of long-wavelength pumped ($\lambda_p >$

λ_{IR}) UCDs was suggested to avoid USPDC noise, which can significantly reduce the DCR to a level of $\sim 10^2$/s [27], attributing noise only to the upconverted spontaneous Raman scattering.

Even though a short-wavelength-pumped UCD suffers from higher DCR, it can still be a better choice for some specific applications given the following advantages it possesses over a long-wavelength-pumped UCD: (1) short-wavelength-pumped UCD can accommodate longer IR wavelengths, the input signal is limited only by the transparency of the nonlinear material [16]; (2) unlike in a short-wavelength-pumped UCD, the upconverted wavelengths in the long-wavelength-pumped UCD may lie outside the sensitivity range of Si detector; (3) long-wavelength-pumped UCD is usually based on waveguide QPM device, which has very small étendue [27]. On the other hand, short-wavelength-pumped UCDs have been implemented not only in the waveguides but also in bulk periodically-poled nonlinear crystals. UCDs that use bulk nonlinear crystals provide a relatively large étendue, which allows better IR signal collection from a larger solid angle [17].

The study of noise sources contributing to short-wavelength-pumped, high conversion efficiency intracavity UCD module is dezirable. However, certain fundamental constraints limit the scope of our experiment. In the case of intracavity setup, fluorescence generated due to optical-pumping of typically used Nd:YVO_4 crystal can not be distinguished from the parametric noise around 800 nm in the mid-IR UCDs. Moreover, circulating inactivity pump power can not be tuned continuously. On the other hand, single-pass upconversion system is straightforward in which pump power scaling does not affect other experimental parameters. Hence, given the significance of investigation of noise sources affecting UCD operation, we deployed a short-wavelength-pumped single-pass upconversion system. Here we report, for the first time to the best of our knowledge, the discovery of new noise source SHG-SPDC (Second-harmonic-generation induced spontaneous parametric downconversion) present in such detectors.

5.2 Theory

When a high-intensity pump field is applied to a periodically-poled nonlinear crystal, several unintended optical parametric processes take place. Among them weak interactions can be ignored. However, incidental nonlinear processes that can affect the upconversion efficiency are defined as potential noise sources of the UCD system. In order to elucidate the concept of parasitic noise generation in a short-wavelength-pumped UCD, the spectral and Feynman diagrams for USPDC and SHG-SPDC processes are shown in Figure 5.1. Both respective 1st steps indicated by grey arrows, i.e. SPDC in USPDC (Figure 5.1 (a)) and SHG in SHG-SPDC (Figure 5.1 (c)) are non-phase-matched. Therefore, respective intensities of SPDC and SHG of the input pump are several orders of magnitude lower than the pump field intensity. Whereas, both respective 2nd steps indicated by purple arrows, i.e. upconversion in USPDC (Figure 5.1 (a)) and SPDC in SHG-SPDC (Figure 5.1 (c)) are quasi-phase-matched. It is important to emphasize that, the first-order QPM condition for upconversion in USPDC, $k_{\mathrm{up}} - k_{\mathrm{IR}} - k_{\mathrm{p}} = 2\pi/\Lambda$ is deliberately fulfilled by the chosen grating period at the intentionally maintained crystal temperature range, for attaining maximum upconversion efficiency. On the other hand, the QPM condition for SPDC in SHG-SPDC, $k_{\mathrm{SHG}} - k_{\mathrm{s}'} - k_{\mathrm{i}'} = 2\pi m/\Lambda$ is adventitiously fulfilled, but only for certain QPM order m, grating period Λ and operating crystal temperature values.

The SPDC in USPDC is broad-band because of the noise pedestal (shown in black in Figure 5.1 (a)) caused by nonidealities in QPM grating periods. But in the next step, the SPDC photons falling only within the acceptance bandwidth of the upconversion detector can get upconverted efficiently by satisfying the QPM condition. In contrast, the SHG is narrow-band due to the typically used narrow-linewidth pump source. The intensity of non-phase-matched SHG also depends on the errors in in QPM grating periods. In general, larger the error higher is the SHG intensity.

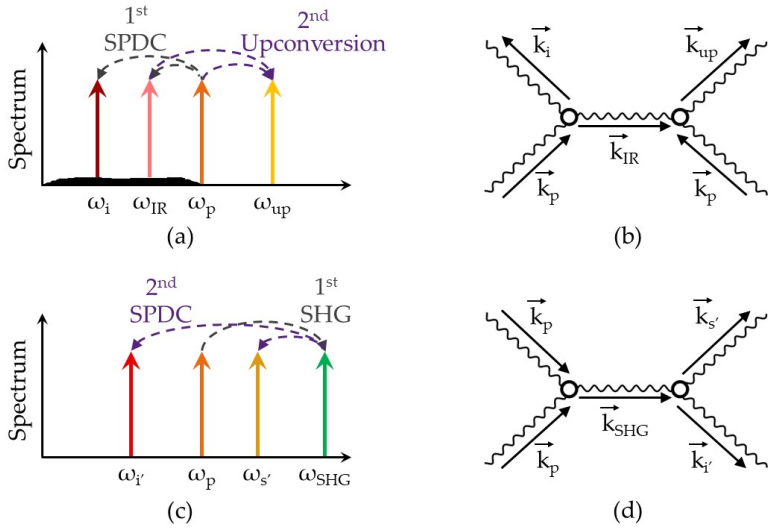

Figure 5.1: Respective spectral and Feynman diagrams for (a,b) USPDC and (c,d) SHG-SPDC noise generation processes. Where, $\omega_j = 2\pi c/\lambda_j$ and $k_j = 2\pi n_j/\lambda_j$.

The technique of periodic reversal of ferroelectric domains is prone to different types of fabrication errors, which can hamper the efficiency of the nonlinear parametric processes. The effects of many common fabrication errors on SHG process have been well studied [28]. One such error type is called random duty cycle (RDC) errors. Lithographic poling method can not prevent errors in local duty cycle even if it preserves the long-range order of the grating periods [29]. This results in domain boundaries not lying at their ideal positions and such RDC errors give rise to noise pedestal in the spatial frequency spectrum of the grating structure. This pedestal can increase the efficiency of phase-mismatched parametric processes [30].

Practical periodically-poled structures can deviate significantly from an ideal structure. A schematic of RDC errors and ideal poling structure is shown in Figure 5.2. A grating with period Λ is considered such that the domains are inverted every l=$\Lambda/2$. In a crystal having RDC errors, the position of the n^{th} domain boundary z_n is shifted from its ideal position

by $\delta z_n = z_n - z_{n,0}$. Then the deviation in length of the n^{th} period is given by $\delta l_n = l_n - l$, where $l_n = z_{n+1} - z_n$ RDC errors are considered to be independent and identically distributed. They obey Gaussian statistics and define normal distribution with variance σ_l^2. The function $g(z)$ is assumed to describe the periodic-poling structure of the crystal, such that its Fourier transform in frequency domain $\tilde{g}(\Delta k)$ represents the SHG efficiency relative to an ideal QPM grating [31].

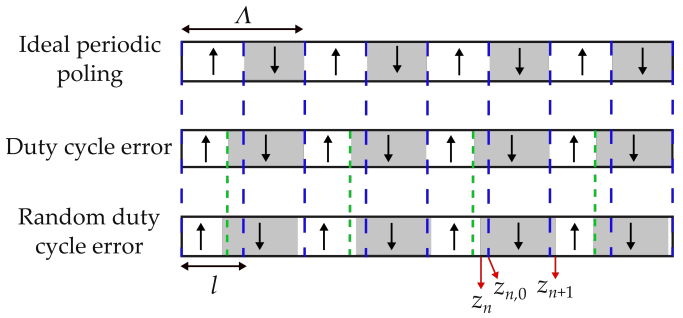

Figure 5.2: Schematic of random duty-cycle (RDC) error in a periodically-poled grating structure.

The exact periodic structure of the crystal can not be measured precisely due to technical limitations [32]. Therefore, $\tilde{g}(\Delta k)$ can not be known. But its ensemble average over randomly perturbed gratings can be calculated using equation 5.1, in order to estimate the height of the QPM pedestal when the average duty cycle and the RDC errors are known [33].

$$\langle |\tilde{g}(\Delta k)|^2 \rangle = \frac{2L}{\Delta k^2 \Lambda} \left(1 - \mathrm{e}^{-\Delta k^2 \sigma_l^2}\right) \tag{5.1}$$

Main focus of this chapter is on the discovery and further study of SHG-SPDC noise. Hence, a theoretical model for SHG-SPDC intensity is proposed using the following analytical treatment. The first step of SHG-SPDC noise generation process is non-phase-matched frequency doubling of the pump field E_p. Hence, starting with the coupled-wave-equation for

SHG process incorporating normalized grating profile of the crystal $g(z)$,

$$\frac{\mathrm{d}E_{\mathrm{SHG}}}{\mathrm{d}z} = \frac{\mathrm{i}\omega_{\mathrm{SHG}} d_{\mathrm{eff}}}{n_{\mathrm{SHG}} c} E_{\mathrm{p}}^2 g(z) \mathrm{e}^{\mathrm{i}\Delta k z} \tag{5.2}$$

where, $\Delta k = 2k_{\mathrm{p}} - k_{\mathrm{SHG}}$. Further, the intensity of the SHG field at position z is given by

$$I_{\mathrm{SHG}}(z) = 2\epsilon_0 n_{\mathrm{SHG}} c |E_{\mathrm{SHG}}|^2 \tag{5.3}$$

By integrating equation 5.2 and substituting E_{SHG} into equation 5.3, we get

$$I_{\mathrm{SHG}}(z) = 2\epsilon_0 n_{\mathrm{SHG}} c \left| \frac{\mathrm{i}\omega_{\mathrm{SHG}} d_{\mathrm{eff}}}{n_{\mathrm{SHG}} c} E_{\mathrm{p}}^2 \right|^2 \left| \int_0^z g(z") \mathrm{e}^{\mathrm{i}\Delta k z"} \mathrm{d}z" \right|^2 \tag{5.4}$$

But intensity of the pump field is given by

$$I_{\mathrm{p}} = 2\epsilon_0 n_{\mathrm{p}} c |E_{\mathrm{p}}|^2 \tag{5.5}$$

By substituting E_{p}^2 from equation 5.5 into equation 5.4 and evoking Fourier transform of the normalized grating profile of the crystal in space domain, we get

$$I_{\mathrm{SHG}}(z) = \frac{\omega_{\mathrm{SHG}}^2 d_{\mathrm{eff}}^2 I_{\mathrm{p}}^2}{2\epsilon_0 n_{\mathrm{p}}^2 n_{\mathrm{SHG}} c^3} |\tilde{g}(\Delta k)|^2 \tag{5.6}$$

Using equation 5.1, we get

$$I_{\mathrm{SHG}}(z) = \frac{\omega_{\mathrm{SHG}}^2 d_{\mathrm{eff}}^2 I_{\mathrm{p}}^2 z}{\epsilon_0 n_{\mathrm{p}}^2 n_{\mathrm{SHG}} c^3 \Delta k^2 \Lambda} \left(1 - \mathrm{e}^{-\Delta k^2 \sigma_l^2}\right) \tag{5.7}$$

As SHG exhibits a linear intensity dependence on the propagation distance [34], it's field amplitude is given as

$$E_{\mathrm{SHG}}(z) = \alpha \sqrt{z} \tag{5.8}$$

where

$$\alpha^2 = \frac{\omega_{\mathrm{SHG}}^2 d_{\mathrm{eff}}^2 I_{\mathrm{p}}^2}{2\epsilon_0^2 n_{\mathrm{p}}^2 n_{\mathrm{SHG}}^2 c^4 \Delta k^2 \Lambda} \left(1 - \mathrm{e}^{-\Delta k^2 \sigma_l^2}\right) \tag{5.9}$$

Second part of SHG-SPDC noise generation is SHG pumped quasi-phase-matched SPDC, given by $\lambda_{\text{SHG}} \rightarrow \lambda_{\text{s}'} + \lambda_{\text{i}'}$. Using coupled-wave-equations for SPDC, we get

$$\frac{\mathrm{d}E_{\text{s}'}}{\mathrm{d}z} = \frac{2\mathrm{i}\omega_{\text{s}'}d_{\text{eff}}}{n_{\text{s}'}c} E_{\text{SHG}}(z)E^{*}_{\text{i}'} \tag{5.10}$$

$$\frac{\mathrm{d}E_{\text{i}'}}{\mathrm{d}z} = \frac{2\mathrm{i}\omega_{\text{i}'}d_{\text{eff}}}{n_{\text{i}'}c} E_{\text{SHG}}(z)E^{*}_{\text{s}'} \tag{5.11}$$

where $\text{E}_{\text{s}'}$ and $\text{E}_{\text{i}'}$ represent the signal and the idler fields, respectively.

Further, by differentiating equation 5.10 w.r.t. z and using equations 1.8, 5.9 and 5.11, we get

$$\frac{\mathrm{d}^2E_{\text{s}'}}{\mathrm{d}z^2} = \frac{1}{2z}\frac{\mathrm{d}E_{\text{s}'}}{\mathrm{d}z} + \gamma z E_{\text{s}'} \tag{5.12}$$

where

$$\gamma = \frac{4\omega_{\text{s}'}\omega_{\text{i}'}d^2_{\text{eff}}}{n_{\text{s}'}n_{\text{i}'}c^2}|\alpha|^2 \tag{5.13}$$

Second-order linear homogeneous differential equation 5.12 has a following general solution

$$E_{\text{s}'}(z) = C_1 \sinh\left(\frac{2}{3}\sqrt{\gamma}z^{\frac{3}{2}}\right) + C_2 \cosh\left(\frac{2}{3}\sqrt{\gamma}z^{\frac{3}{2}}\right) \tag{5.14}$$

Considering the following initial conditions for SPDC,

$$I_{\text{s}'}(0) = 0 \tag{5.15}$$

$$I_{\text{i}'}(0) = I_{\text{i}0} \tag{5.16}$$

where,

$$I_{\text{i}0} = \frac{c\hbar\omega_{\text{i}}}{4\pi^2 n_{\text{i}}}\int_{\psi}^{\psi+\mathrm{d}\psi}\sin\psi\mathrm{d}\psi\int_{k_{\text{i}}}^{k_{\text{i}}+\mathrm{d}k_{\text{i}}}k_{\text{i}}^2\mathrm{d}k_{\text{i}} \tag{5.17}$$

is the intensity of a of an input idler is given by [35], when a SPDC process is described semi-classically by accounting for quantum effects of vacuum

fluctuations [36], having k-vectors between k_{i} and $k_{\mathrm{i}} + \mathrm{d}k_{\mathrm{i}}$ with angles ranging between ψ and $\psi + \mathrm{d}\psi$ are considered. Then, the equation for SHG-SPDC noise intensity is given by,

$$I_{\mathrm{s}'}(z) = \frac{\omega_{\mathrm{s}'}\omega_{\mathrm{i}'}^2 n_{\mathrm{i}'}^2 \hbar\psi}{4\pi^2 c^2} \sinh^2\left(\frac{2}{3}\sqrt{\gamma} z^{\frac{3}{2}}\right) \mathrm{d}\omega_{\mathrm{i}'}\mathrm{d}\psi \tag{5.18}$$

5.3 Experimental setup

A schematic of the experimental setup is shown in Figure 5.3. It consists of a single-pass upconversion system. The pump source is a commercial cw Yb-fiber laser (IPG Photonics, YLR-30-1064-LP-SF) delivering up to 30 W of output power at 1064 nm in a single-frequency, linearly polarized beam with M^2<1.01. The laser is operated at maximum power, and the input pump power is adjusted using a combination of half-wave plate H_1 and polarizing beam-splitter (PBS) cube. A second half-wave plate H_2 is placed to control the pump polarization. Using lens L_1 (focal length, f_1=200 mm), the pump beam is focused at the centre of the crystal to the beam waist radius of $w_{0\mathrm{p}}$∼48 µm. The crystal is housed in an oven (PV40, Covesion) with a stability of ±0.01 °C, which can be controlled from room temperature to 200 °C. Two different multiple-grating period, 5% MgO-doped PPLN crystals are used in this experiment. A 40-mm-long crystal with grating periods, Λ=12 and 12.96 µm (suitable for telecom signal detection), and a 20-mm-long MgO:PPLN with Λ=22 and 23 µm (suitable for mid-IR wavelength detection) are used. The transmitted pump beam from the crystal is reflected by a plane dichroic mirror M_1 in order to separate the generated noise from the pump and the pump power is monitored through a power meter. The noise photons are transmitted through M_1. After passing through a periscope arrangement (M_{2-3}), polarization of the noise photons is changed to *p*-polarization state with respect to the working surface of an equilateral dispersive prism (N-SF11). The prism is used to spectrally separate out the noise from the residual pump, SHG of the pump at 532 nm

and the upconverted photons. An iris is placed in the image plane of lens L_2 (f_2=50 mm) as a spatial filter in order to pass only the noise photons while blocking the stray beams. Lens L_3 (f_3=50 mm) is used to focus the beam of noise photons into the imaging system. For the elimination of ambient light a bandpass filter BPF (different filters for telecom and mid-IR signal wavelengths) is placed in front of a sensitive electron multiplying CCD (EM-CCD) camera (Luca S 658M, Andor) capable of single-photon counting, which is used to image the noise photons in order to further measure the noise counts. The IR source for upconversion detection is not included in the setup, because the sole focus of this experiment is to investigate the noise characteristics of short-wavelength-pumped UCDs. However, the source can be readily installed in order to use this system as an IR detector.

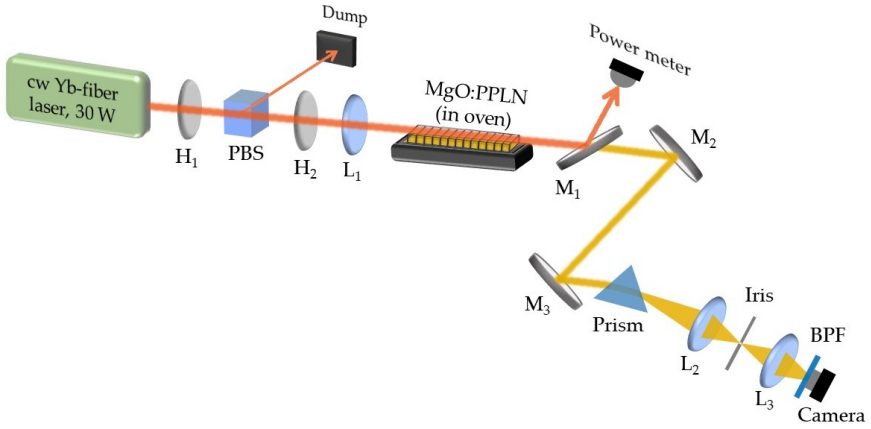

Figure 5.3: Schematic of the experimental setup. H_{1-2}, half-wave plates; PBS, polarizing beam splitter; L_{1-3}, lenses; M_{1-3}, mirrors; BPF, bandpass filter.

5.4 Results

5.4.1 UCD for telecom signal detection

Initially, noise from a 40-mm-long MgO:PPLN crystal with two grating periods of Λ=12 and 12.69 µm associated with telecom band (1.3 µm$<\lambda_{IR}<$1.7 µm) detection was measured. The wavelengths corresponding to USPDC and SHG-SPDC noise (λ_{up} and $\lambda_{s'}$, respectively) were first calculated using relevant Sellmeier equations for MgO:PPLN [37]. The theoretical phase-matching curves shown in Figure 5.4 are based on the first-order QPM condition for upconversion of telecom wavelengths (y-axis on right) represented by solid lines ($\lambda_{IR} + \lambda_p \rightarrow \lambda_{up}$) and SPDC of 532 nm denoted by dashed lines ($\lambda_{SHG} \rightarrow \lambda_{s'} + \lambda_{i'}$). As seen from the graph, wavelengths corresponding to USPDC and SHG-SPDC for Λ=12 µm are well separated from each other throughout the complete temperature tuning range. On the other hand, SHG-SPDC for Λ=12.69 µm is not contributing in the noise source, since QPM condition for SPDC of SHG is not satisfied in this case.

In order to experimentally investigate the properties of generated noise, a series of images was recorded using the EM-CCD camera at different crystal temperatures from 50 to 160 ^{o}C. In this experiment, a bandpass filter with central wavelength of λ_c=625 nm and bandwidth of $\Delta\lambda_{FWHM}$=50 nm was used to confine the spectral region of interest from 600 to 650 nm by removing ambient light from the measured data. Figure 5.5 shows the images taken while temperature of the crystal was kept constant at 50 ^{o}C. The images suffer from astigmatism due to dispersion by the prism. However, it does not affect the noise photon rate measurements. Two diamond-shaped patterns were observed in the image obtained using Λ=12 µm, as seen in Figure 5.5 (a). The USPDC and SHG-SPDC noise parts are marked by red and yellow boxes, respectively. Two distinct patterns for two different noise sources were expected from the theoretical results, because at 50 ^{o}C the wavelengths corresponding to USPDC and SHG-SPDC noise

were calculated to be λ_{up}=634.9 nm and $\lambda_{s'}$=605 nm, respectively. Therefore, as discussed before, both noise sources were spectrally separated from each other by the prism, resulting in spatially distinguishable patterns. In the case of Λ=12.69 µm as shown in Figure 5.5 (b), only one diamond-shaped pattern was observed, associated with USPDC process corresponding to upconverted wavelength of λ_{up}=646.7 nm at 50 °C.

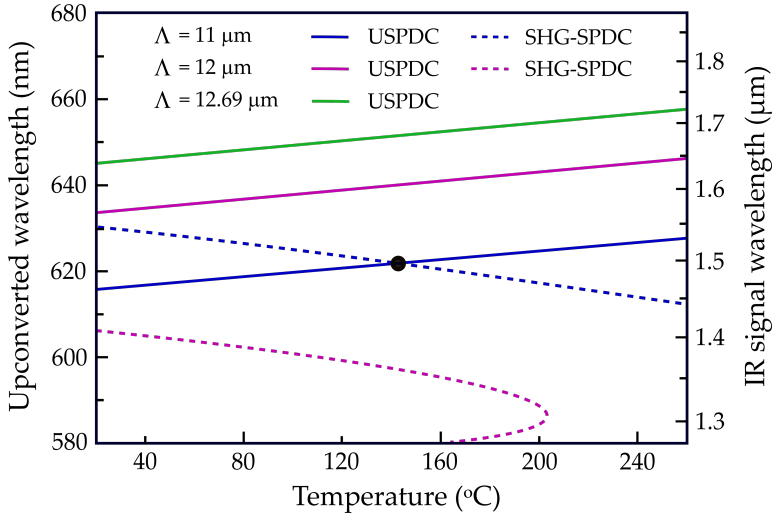

Figure 5.4: Phase-matching wavelength corresponding to USPDC and SHG-SPDC noise versus crystal temperature, plotted for upconversion of telecom wavelength (y-axis on right) using different grating periods.

From perspective of the sensitivity of the detector, these two grating periods (12 and 12.69 µm) can have similar background noise levels, since noise photons due to SHG-SPDC for Λ=12 µm can be removed using a narrow bandpass spectral filter. However, the noise due to SHG-SPDC can not be even separated from USPDC in some particular cases, if the wavelengths corresponding to USPDC and SHG-SPDC noise have the same value at certain phase-matching conditions. An example is shown in Figure 5.4, where a black dot represents λ_{up}=$\lambda_{s'}$. It implies that, the UCD will suffer from a higher total background noise if a crystal with grating period

of Λ=11 µm is operated at the phase-matching temperature of 147 °C.

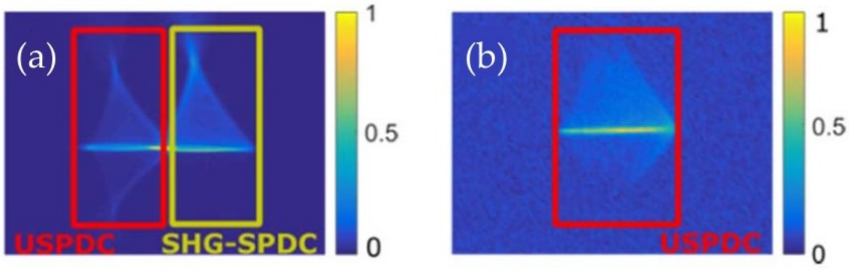

Figure 5.5: Images used for noise count measurements at crystal temperature of 50 °C, for grating periods (a) Λ=12 µm and (b) Λ=12.69 µm.

Further, the noise photon rate i.e. DCR of the detector was calculated from the images shown in Figure 5.5. The formula $(R\text{-}R_0)/\tau$ was used to deduce DCR, where respective noise R (when pump power P_p>0) and corresponding background R_0 (P_p=0) are sums of the camera pixel readout in the region of interest; and τ is the integration time of the camera. Similarly, experimental data acquired from all EM-CCD images taken at different crystal temperatures was expressed in the form of DCRs associated with both respective noise sources. In order to use the full dynamic range of the camera τ was selected from 3 seconds to 1 minute depending on the intensity of the noise. The results for grating period Λ=12 µm are shown in Figure 5.6, while the pump power was kept constant at the maximum of 22 W. The inset graph implies that, the change in temperature from 50 to 57 °C has a larger impact on SHG-SPDC noise than that on USPDC noise count. As the non-phase-matched SHG is a narrow-band source, its intensity I_SHG depends on the instantaneous value of $|\tilde{g}(\Delta k)|^2$ and not on the average value like in the case of USPDC with broadband SPDC pedestal. Hence, this trend can be attributed to the significant fluctuations in the SHG intensity with varying crystal temperature. As seen in the main graph of Figure 5.6, both noise sources have similar DCR levels in general but at certain phase-matching conditions SHG-SPDC can dramatically increase the noise floor

of the UCD. In the particular case, at crystal temperature of 52 °C, the DCR due to SHG-SPDC is 5 times greater than that due to USPDC noise. The measured DCR due to SHG-SPDC process was strongly reduced for T>100 °C, because when the crystal temperature was increased above 100 °C, SHG-SPDC wavelength started falling below 600 nm and thus the bandpass filter started blocking it. This suggests that spectral filtering effectively decreases the noise contribution coming from SHG-SPDC process.

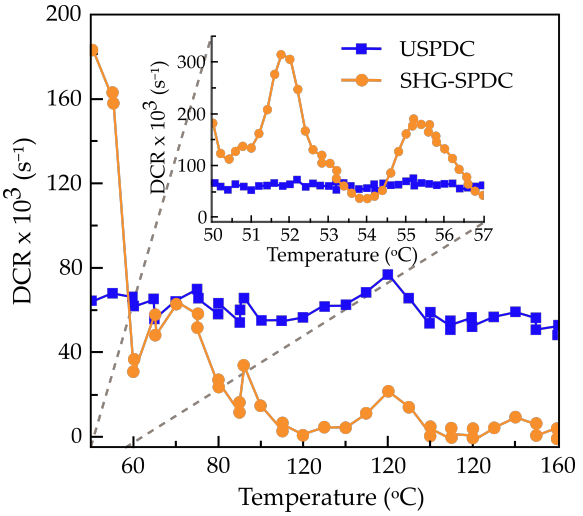

Figure 5.6: Measured total dark count rate of UCD as a function of crystal temperature, at the maximum pump power of P_p=22 W, for Λ=12 µm.

To study the dependence of parasitic noise on the pump power, the respective DCRs due to the USPDC and SHG-SPDC were measured as a function of varying input pump power while the operating temperature of the MgO:PPLN crystal was kept fixed at 50 °C. The results are shown in Figure 5.7. The uncertainty in each measured DCR is less than 4x10^3 s^{-1}. At the maximum pump power of P_p=22 W, the upconversion efficiency η_{up} was theoretically estimated to be close to unity. The SPDC intensity is known to be proportional to P_p [26], while η_{up} is linearly proportion

to P_p for η_{up} well below 0.5, but saturates as it approaches the unity [27]. Therefore, the USPDC noise rate is initially proportional to P_p^2 but becomes linear as P_p approaches its maximum value, as seen from the experimental data fitted with a 2nd-degree polynomial in Figure 5.7. The SHG-SPDC data is fitted with 2nd- and 3rd-degree polynomials (black dashed and green solid curve, respectively), indicating a better fit, i.e. a lower chi-squared value for the 3rd-degree polynomial. In a solitary SHG process, the SHG rate is known to scale with P_p^2. However, the fit of SHG-SPDC data to a 3rd-degree polynomial in P_p suggests that the SHG and SPDC processes are coupled in more complex manner as SHG rate increases along the crystal length.

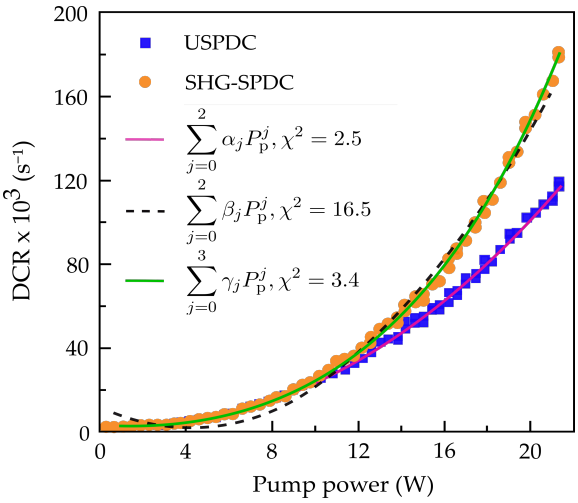

Figure 5.7: Measured total dark count rate of UCD as a function of input pump power, at crystal temperature of T=50 °C, for Λ=12 µm. α_j, β_j and γ_j are the fitting parameters.

The DCR caused due to SHG-SPDC noise is plotted together with the theoretically calculated SHG-SPDC intensity $I_{s'}$ using equation 5.18, as shown in Figure 5.8. The value of RDC errors used in the simulation is σ_l/l=10%. The result obtained from the proposed theoretical model starts deviating from the measured DCR when P_p>12 W. The large discrepancy

between the simulation and experimental data can be attributed to the narrow-band nature of the non-phase-matched SHG, because the model is based on the average value of $|\tilde{g}(\Delta k)|^2$ as its instantaneous value can not be known. Therefore, more rigorous model is required to explain the dependence of SHG-SPDC on P_{p}.

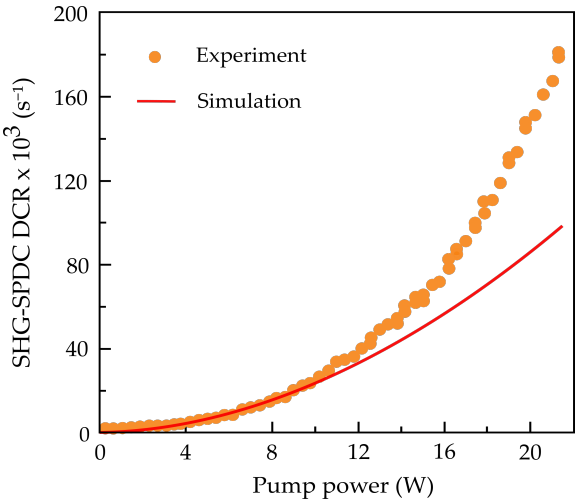

Figure 5.8: Comparison between the measured dark count rate caused due to SHG-SPDC noise and simulation based on the proposed theoretical model.

5.4.2 UCD for mid-IR signal detection

In order to study the presence of parasitic noise in UCDs designed for mid-IR range (2.5 µm$<\lambda_{\mathrm{IR}}<$4 µm) detection, a 20-mm-long MgO:PPLN crystal with two grating periods of Λ=22 and 23 µm was deployed in the single-pass UCD setup. Corresponding theoretical phase-matching curves for USPDC and SHG-SPDC wavelengths were plotted, as shown in Figure 5.9. The first-order QPM condition was used for upconversion of mid-IR wavelengths (y-axis on right). However, third-order QPM condition was used for SPDC of 532 nm i.e. $k_{\mathrm{SHG}} - k_{\mathrm{s}'} - k_{\mathrm{i}'} = 3.2\pi/\Lambda$. The intersection point

between calculated USPDC and SHG-SPDC wavelengths is represented by a black dot. For Λ=22 µm at crystal temperature of 160 °C, both noise sources have the same wavelength (λ_{up}=$\lambda_{s'}$). Hence, the UCD will suffer from higher background noise in this particular case. As seen from Figure 5.9, wavelengths of the upconverted signal are in the range of 750 to 850 nm. Therefore, a bandpass filter with λ_c=800 nm and $\Delta\lambda_{FWHM}$=100 nm was used in this experiment to filter out the ambient light.

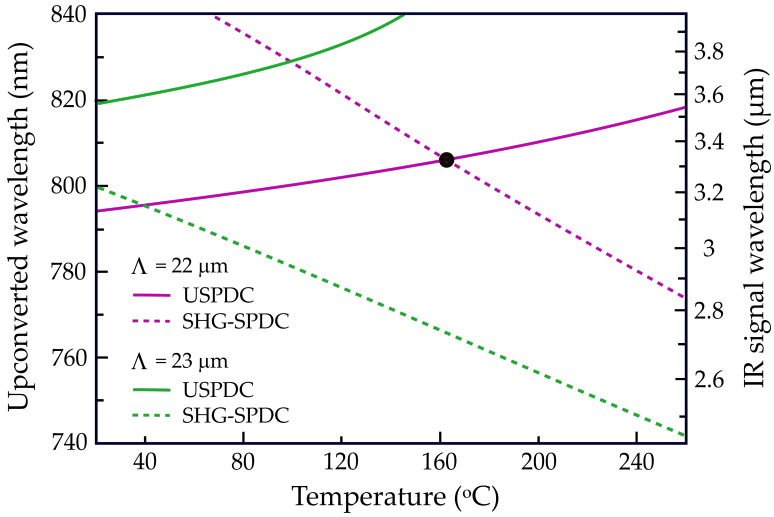

Figure 5.9: Phase-matching wavelength corresponding to USPDC and SHG-SPDC noise versus crystal temperature, plotted for upconversion of mid-IR wavelength (y-axis on right) using different grating periods.

A series of images was taken at different crystal temperatures, from room temperature to 160 °C, while keeping the pump power constant at 22 W, to experimentally observe the degeneracy in noise at 160 °C. Figure 5.10 shows the images taken by camera when crystal temperature was kept fixed at 50 °C. Similar to Figure 5.5 (a), Figures 5.10 (a) and (b) show two separate patterns, which indicate that both grating periods satisfy the QPM condition for SHG-SPDC noise, as predicted by the theoretical curves.

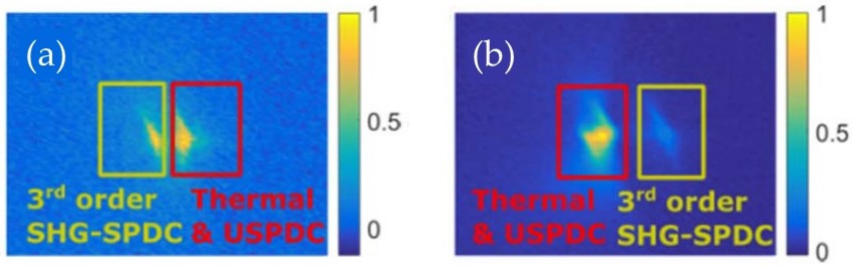

Figure 5.10: Images used for noise count measurements at crystal temperature of 50 °C, for grating periods (a) Λ=22 µm and (b) Λ=23 µm.

Unlike UCDs operating in the telecom region, the mid-IR UCDs additionally suffer from upconverted thermal radiation. This noise originates mainly from the nonlinear material and becomes a dominant source of DCR even at room temperature while operating the UCD at absorption edge of the MgO:PPLN crystal i.e. from and above 3.5 µm. [24]. However, the photons generated due to the upconverted thermal radiation cannot be physically separated from the USPDC noise. Hence, the red boxes in Figure 5.10 are labelled as "Thermal & USPDC". The thermal noise becomes prominent for the case of Λ=23 µm as seen from the 5.10 (b), because the input λ_{IR} is greater than 3.5 µm.

As mentioned before, the SPDC followed by the SHG process satisfies third-order QPM condition. Therefore, observed SHG-SPDC intensity is reduced by factor of 9 over the first-order quasi-phase-matched SPDC process working under same parameters. This results into overall much lower SHG-SPDC intensity as compared to that of the accompanying USPDC noise. It is observed that SHG-SPDC noise for Λ=23 µm is negligible throughout the whole temperature range, and the total dark count rate of the UCD is primarily based on USPDC and upconverted thermal noise. Variation in total DCR as a function of crystal temperature is shown in Figure 5.11. The DCR due to USPDC and upconverted thermal noise in the mid-IR UCD is more than 5 times that of in the telecom UCD, as seen from

Figure 5.6. Hence, the noise contribution from the upconverted thermal radiation is critical. It implies that, in mid-IR UCDs major challenge is to overcome the internal noise contribution from MgO:PPLN crystal because it acts as a source of thermal background radiation.

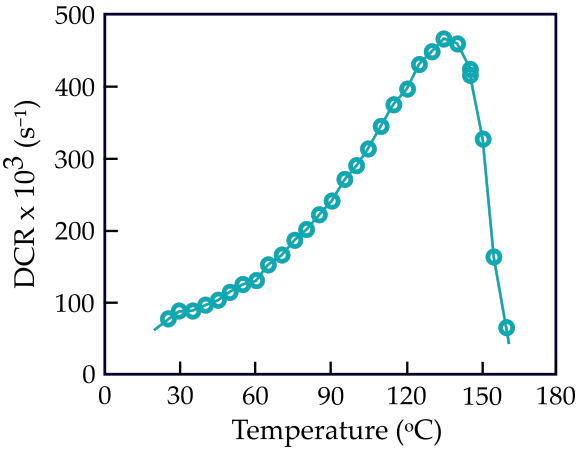

Figure 5.11: Measured total dark count rate of UCD as a function of crystal temperature, at the maximum pump power of P_p=22 W, for Λ=23 µm.

5.5 Conclusion

In this chapter, we have reported a newly discovered noise source in short-wavelength-pumped upconversion detectors. In order to demonstrate its presence together with other well-known noise sources such as USPDC and upconverted thermal radiation, single-pass UCDs based on MgO:PPLN crystals pumped by 1-µm Yb-fiber laser are deployed. Two multiple-grating MgO:PPLN crystals are used to investigate the noise properties in different spectral regions, 40-mm-long crystal with grating periods of Λ=12 and 12.96 µm (suitable for upconversion of telecom wavelengths) and 20-mm-long crystal with Λ=22 and 23 µm (suitable for upconversion of mid-IR wavelengths). A sensitive EM-CCD camera is used to measure the generated

noise photons, which are denoted by dark count rate of the upconversion detector.

We have explained the origin of SHG-SPDC noise, supported by phase-matching curves of unintended parametric interactions taking place inside the strongly pumped periodically-poled nonlinear materials. Similar to USPDC process, generation of SHG-SPDC noise is also based on a two-step mechanism, in which non-phase-matched SHG of the pump splits into SPDC though QPM. The SPDC in USPDC gives rise to broadband pedestal. On the other hand SHG in SPDC is narrow-band. This difference changes the dynamics of both noise sources. We have also proposed the theoretical model to support quantitative analysis of SHG-SPDC noise. The discrepancy between experimentally measured and theoretically calculated SHG-SPDC noise counts could be due to the difference in the average and instantaneous value of the crystal structure function.

To compare the characteristics of different noise contributions, we have experimentally studied the response of USPDC, upconverted background thermal radiation (only in the case of mid-IR UCDs) and SHG-SPDC noise by varying the pump power and the crystal temperature. The intensity of SHG-SPDC noise is found to be approximately proportional to the cube of pump power, at fixed crystal temperature. For certain phase-matching conditions SHG-SPDC can potentially increase the noise floor of the detector, at a given pump power. SHG-SPDC noise usually has a different wavelength than the upconverted signal intended to measure, thus the noise can be removed by using proper spectral filters. However, SHG-SPDC may have the same wavelength as the upconverted signal for some phase-matching instances, which makes spectral filtering impossible.

The results presented in this work can be extended to other UCDs pumped at different wavelengths, employing different nonlinear quasi-phase-matched materials including orientation-patterned crystals in bulk as well as in waveguide configuration. Taking into account the influence of SHG-SPDC noise on overall performance of the UCDs, it is important

to carefully design and operate such detectors especially when detecting weak input IR signals at single-photon level. Further work on simulation is required to precisely calculate the intensity of SHG-SPDC noise.

References

[1] B. Stuart, "Infrared spectroscopy: fundamentals and applications," Wiley, UK (2004).

[2] M. Walsh, R. Reddy and R. Bhargava, "Label-free biomedical imaging with mid-IR spectroscopy," IEEE J. of Selected Topics in Quantum Elect. 18, 1502-1513, (2012).

[3] P. Werle, F. Slemr, K. Maurer, R. Kormann, R. Mucke, B. Janker, "Near- and mid-infrared laser-optical sensors for gas analysis," Opt. Lasers Eng. 37, 101-1114 (2002).

[4] S. Wolf, T. Trendle, J. Kiessling, J. Herbst, K. Buse, and F. KÃ¼hnemann, "Self-gated mid-infrared short pulse upconversion detection for gas sensing," Opt. Express 25, 24459-24468 (2017).

[5] K. Jahromi, Q. Pan, L. Høgstedt, S. Friis, A. Khodabakhsh, P. Moselund, and F. Harren, "Mid-infrared supercontinuum-based upconversion detection for trace gas sensing," Opt. Express 27, 24469-24480 (2019).

[6] A. Rogalski, "Infrared detectors," third edition, CRC Press, (2018).

[7] A. Karim and J. Andersson, "Infrared detectors: advances, challenges and new technologies," IOP Conf. Ser.: Mater. Sci. Eng. 51, 012001 (2013).

[8] I. Amiri, F. Houssien, A. Rashed, A. Mohammed, "Temperature effects on characteristics and performance of near-infrared wide bandwidth for different avalanche photodiodes structures," Results in Phys. 14, 102399 (2019).

[9] C. Tan and H. Mohseni, "Emerging technologies for high performance infrared detectors," Nanophotonics 7, 169-197 (2017).

[10] R. Pedersen, L. Høgstedt, A. Barh, L. Meng and P. Tidemand-Lichtenberg, "Characterization of the NEP of mid-infrared upconversion detectors," IEEE Phot. Tech. Lett. 31, 681-684 (2019).

[11] J. Dam, C. Pedersen, and P. Tidemand-Lichtenberg, "High-resolution two-dimensional image upconversion of incoherent light," Opt. Lett. 35, 3796-3798 (2010).

[12] J. Dam, P. Tidemand-Lichtenberg, and C. Pedersen, "Room-temperature mid-infrared single-photon spectral imaging" Nat. Photonics 6, 788 (2012).

[13] L. Huot, P. Moselund, P. Tidemand-Lichtenberg, L. Leick, and C. Pedersen, "Upconversion imaging using an all-fiber supercontinuum source," Opt. Lett. 41, 2466 (2016).

[14] L. Kehlet, N. Sanders, P. Tidemand-Lichtenberg, J. Dam, and C. Pedersen, "Infrared hyperspectral upconversion imaging using spatial object translation," Opt. Express 23, 34023 (2015).

[15] H. Maestre, A. Torregrosa, and J. Capmany, "IR Image upconversion using band-limited ASE illumination fiber sources,"Opt. Express 24, 8581 (2016).

[16] A. Barh, C. Pedersen, and P. Tidemand-Lichtenberg, "Ultra-broadband mid-wave-IR upconversion detection," Opt. Lett. 42, 1504-1507 (2017).

[17] L. Meng, A. Fix, M. Wirth, L. Høgstedt, P. Tidemand-Lichtenberg, C. Pedersen, and P. J. Rodrigo, "Upconversion detector for range-resolved DIAL measurement of atmospheric CH_4," Opt. Express 26, 3850 (2018).

[18] M. Albota and F. Wong, "Efficient single-photon counting at 1.55 μm by means of frequency upconversion," Opt. Lett. 13, 1449-1451 (2004).

[19] F. Ma, L. Liang, J. Chen, Y. Gao, M. Zheng, X. Xie, H. Liu, Q. Zhang, and J. Pan, "Upconversion single-photon detectors based on integrated periodically poled lithium niobate waveguides [Invited]," J. Opt. Soc. Am. B 35, 2096 (2018).

[20] L. Lehmann, L. Grossard, L. Delage, F. Reynaud, M. Chauvet, and F. Bassignot, "Single photon MIR upconversion detector at room temperature with a PPLN ridge waveguide," Opt. Express 27, 19233-19241 (2019).

[21] C. Tang, "Spontaneous Emission in the Frequency Up-Conversion Process in Nonlinear Optics," Phys. Rev. 182, 367 (1969).

[22] H. Pan, H. Dong, and H. Zeng, "Efficient single-photon counting at 1.55 µm by intracavity frequency upconversion in a unidirectional ring laser," Appl. Phys. Lett. 89, 191108 (2006).

[23] P. Kuo, J. Pelc, C. Langrock, and M. Fejer, "Using temperature to reduce noise in quantum frequency conversion," Opt. Lett. 43, 2034 (2018).

[24] A. Barh, P. Tidemand-Lichtenberg, and C. Pedersen, "Thermal noise in mid-infrared broadband upconversion detectors," Opt. Express 26, 3249 (2018).

[25] J. Pelc, C. Phillips, D. Chang, C. Langrock, and M. Fejer, "Efficiency pedestal in quasi-phase-matching devices with random duty-cycle errors," Opt. Lett. 36, 864 (2011).

[26] J. Pelc, C. Langrock, Q. Zhang, and M. Fejer, "Influence of domain disorder on parametric noise in quasi-phase-matched quantum frequency converters" Opt. Lett. 35, 2804 (2010).

[27] J. Pelc, L. Ma, C. Phillips, Q. Zhang, C. Langrock, O. Slattery, X. Tang, and M. Fejer, "Long-wavelength-pumped upconversion single-photon detector at 1550 nm: performance and noise analysis," Opt. Express 19, 21445 (2011).

[28] M. Fejer, G. Magel, D. Jundt, and R. Byer, "Quasi-phase-matched second harmonic generation: tuning and tolerances," IEEE J. Quantum Electron. 28, 2631-2654 (1992).

[29] C. Phillips, J. Pelc, M. Fejer, "Random duty cycle errors in QPM gratings: implications for sensitive nonlinear-optical devices," Advanced Solid State Lasers, JTh2A.60, OSA (2013).

[30] C. Phillips, J. Pelc, and M. Fejer, "Parametric processes in quasi-phasematching gratings with random duty cycle errors," JOSA B 30, 982-993 (2013).

[31] J. Pelc, "Frequency conversion of single photons: physics, devices, and applications," Ph.D. dissertation (Stanford University, 2012).

[32] HC Photonics corp.

[33] C. Phillips, "Broadband optical sources based on highly nonlinear quasi-phasematched interactions," Ph.D. dissertation (Stanford University, 2012).

[34] W. Wang, Y. Sheng, S. Liu, X. Niu, and W. Krolikowski, "Manipulation of quadratic cascading processes in a locally quasi-periodic $\chi^{(2)}$ medium," Opt. Express 22, 6976-6983 (2014).

[35] P. Powers and J. Haus, "Fundamentals of nonlinear optics," CRC Press, USA (2011).

[36] T. Giallorenzi and C. Tang, "Quantum theory of spontaneous parametric scattering of intense light," Phys. Rev. 166, 225-233 (1968).

[37] O. Gayer, Z. Sacks, E. Galun, and A. Arie, "Temperature and wavelength dependent refractive index equations for MgO-doped congruent and stoichiometric $LiNbO_3$," Appl. Phys. B 91, 343-348 (2008).

Chapter 6

Summary and outlook

This chapter summarizes work presented in the thesis and discusses avenues for future developments based on obtained results. Our main objective was to demonstrate cw tunable sources in different spectral regions of interest. To accomplish this goal we characterized two novel nonlinear crystals in different device architectures. Additionally, we analyzed the noise properties influencing cw short-wavelength-pumped upconversion detectors.

The specific achievements of this work include:

- First implementation of cw OPO using fan-out grating design PPKTP crystal. Under pure SRO configuration, OPO is widely tunable across 745-908 nm in signal and 1284-1860 nm in idler, at the crystal temperature of 50 ^{o}C. Further, output coupling of intracavity signal enables increased output wavelength tuning coverage at room temperature operation, providing total power of 1.65 W with $>$150 mW of signal power over the entire signal wavelength tuning range and $>$400 mW of idler power over 66% of the idler wavelength tuning range. The signal and idler show passive power stability better than 5.5% rms and 3.2% rms, respectively, over 2.6 minutes. The signal exhibits frequency stability better than 194 MHz over 37 seconds and it has an instantaneous linewidth of 7.5 MHz at 831 nm, with beam circularity $>$95%.

- First successful demonstration of tunable cw source based on newly developed quasi-phase-matched nonlinear crystal, OP-GaP. By exploit-

ing single-pass DFG between Tm-fiber laser and MgO:PPLN OPO, mid-IR radiation across 4608-4694 nm is generated. The source provides 43 mW of DFG power at 4608 and 4635 nm, with >30 mW power over 96% of the entire wavelength tuning range. The DFG source exhibits passive power stability better than 2.5% rms over 1.7 minutes. The DFG spectra have FWHM linewidth of 3 nm, with the beam circularity >92%. The experimentally obtained DFG temperature acceptance bandwidth is 10.8 ^{o}C at the phase-matching temperature of 46 ^{o}C. The polarization-dependent transmission of the OP-GaP crystal at DFG input wavelengths is also recorded.

- Discovery of SHG (532 nm)-induced spontaneous parametric downconversion (SHG-SPDC) noise in short-wavelength-pumped upconversion detectors (UCDs) designed for signal detection in different spectral regions. Noise contribution of cw single-pass UCDs are investigated using two multi-grating PPLN crystals with grating periods of 12 & 12.69 μm for telecom and 22 & 23 μm for mid-IR signals. The properties of SHG-SPDC noise are characterized and compared with upconverted spontaneous parametric downconversion (USPDC) noise and upconverted background thermal radiation. SHG-SPDC noise generation is a two-step process, phase-mismatched SHG of 1064 nm pump splits into SPDC via quasi-phase-matching. Experimentally, SHG-SPDC intensity is found to be approximately proportional to the cube of the pump power. Simulations are performed for the same using proposed theoretical model. For certain phase-matching conditions SHG-SPDC has higher dark count rates than other noise contributions and moreover it may have the same wavelength as the upconverted signal which makes its spectral filtering impossible.

Future possible extensions of this work are given below.

- In the case of PPKTP OPO, low-threshold operation and increased output powers can be achieved with higher crystal transmission for the green and improvements in the fan-out grating period structure. Further, the output power stability and frequency stability can be enhanced by isolating the system from mechanical vibrations and by deploying active stabilization control for the OPO cavity length, respectively. Also, it would be of interest to study the OPO characteristics under variable output coupling of the signal. Moreover, since these idler wavelengths are ideal to pump semiconductor nonlinear crystals such as CSP and OP-GaP, this OPO having single-frequency nature and excellent beam quality can be used in the future to demonstrate cascaded cw OPO operation in the mid-IR.

- In the case of OP-GaP based DFG source, further scaling of the DFG power is possible with improved crystal transmission. It is also important to determine the source of polarization dependent transmission nature of OP-GaP. The overall performance of the system can be enhanced by using OP-GaP crystals with uniform grating periods and negligible absorption of the interacting waves. Most importantly, the long-standing issue of cw OPOs based on traditional oxide-based nonlinear materials offering limited mid-IR transparency can be addressed with the matured orientation-patterned crystal growth technology. Hence, further efforts need to be put into developing good quality OP-GaP crystals which would result in low-threshold, narrow-linewidth cw mid-IR OPOs.

- Considering the significant impact of SHG-SPDC noise on the overall performance of UCDs a careful attention should be given when designing such detectors in future particularly intended for weak IR signal detection at single-photon level operation in quantum fre-

quency converters. However, more research is required to establish an explicit theoretical model for the better understanding of the cubic dependence of SHG-SPDC intensity on the pump power. Further studies with more focus on SHG-SPDC noise is therefore suggested. The obtained results can also be extended to the other forms of UCDs which may use waveguide configuration, different nonlinear materials, or different pump wavelengths. Since most of the UCDs are based on pump-enhanced intracavity design to increase the upconversion efficiency, it is of great interest to study SHG-SPDC and USPDC noise sources in high-efficiency intracavity UCDs.